APPLICATION OF THE MÖBIUS TRANSFORMATION TO NONLINEAR FDTD SIMULATIONS OF THE IONOSPHERE

By

ANTHONY JOSEPH ERDMAN

A DISSERTATION PRESENTED TO THE GRADUATE SCHOOL
OF THE UNIVERSITY OF FLORIDA IN PARTIAL FULFILLMENT
OF THE REQUIREMENTS FOR THE DEGREE OF
DOCTOR OF PHILOSOPHY

UNIVERSITY OF FLORIDA

2019

I dedicate this to my wife, Dooyoung Kim.

ACKNOWLEDGMENTS

These past four and a half years have been a true honor and pleasure to work as a graduate student in the Ionospheric Radio Lab (IRL) here at University of Florida.

I would like to thank my advisor, Dr. Robert Moore, for his endless enthusiasm and constant source of ideas. Also, I have greatly enjoyed the varied graduate school experience full of field work and lab work that he provided for me. I would also like to thank Dr. Vladimir Rakov, Dr. Martin Uman, Dr. Zoleikha Biron, and Dr. Subrata Roy for serving as members on my committee. It was a privilege to take Dr. Rakov's 'Lightning' course and Dr. Uman's 'Plasma Physics' course.

To my labmates: Michael Mitchell who provided invaluable guidance on how everything in the lab works. Daniel Kotovsky who was able to provide a reference for any topic. Hunter Burch and Quincy Flint who were always available to have a conversation on anything, work related or not. Robbie Wilkes and Clinton Snider who were always able to lighten the mood through a good joke.

To my family: My parents, Robert and Toni, who were always supportive of me and my studies. My brothers, Robert and Paul, who always keep me in check.

Most importantly, to my wife, Dooyoung Kim. Thank you. We went through this process together and you were always there for me, understanding. I was able to complete this journey because of you. You have been a wonderful partner though all of this.

TABLE OF CONTENTS

page

ACKNOWLEDGMENTS . . . 4

LIST OF TABLES . . . 7

LIST OF FIGURES . . . 8

ABSTRACT . . . 10

CHAPTER

1 INTRODUCTION . . . 12

1.1 The Ionosphere and Ionospheric Modification . . . 12
1.1.1 Ionospheric Heating by Man-Made HF Transmitters . . . 14
1.1.2 Ionospheric Heating by Man-Made VLF Transmitters . . . 16
1.2 Ionospheric Effects of Lightning . . . 17
1.3 Finite-Difference Time-Domain . . . 19
1.3.1 Möbius Transformation . . . 22
1.3.2 Nonlinear FDTD . . . 25
1.4 Scientific Contributions . . . 26

2 LINEAR COLD PLASMA FDTD . . . 28

2.1 Linear Methods . . . 28
2.1.1 Method 1 . . . 33
2.1.2 Method 2 . . . 34
2.1.3 Method 2: Non-Möbius Transformation . . . 36
2.1.4 Method 3 . . . 37
2.1.5 Method 4 . . . 39
2.1.6 Method 5 . . . 42
2.2 Demonstration of Methods . . . 44
2.2.1 Möbius: Unit Step and Impulse Response . . . 44
2.2.2 Möbius: Faraday Rotation . . . 45
2.2.3 Möbius: Reflection and Transmission Characteristics . . . 47
2.2.4 Non-Möbius: Reflection and Transmission Characteristics . . . 55
2.3 Linear Method Comparison . . . 57
2.3.1 Numerical Comparisons . . . 57
2.3.2 Stability . . . 60
2.3.3 Memory and Speed . . . 60
2.3.4 Nonlinear Applicability . . . 62

3 HF HEATING OF THE D-REGION . . . 64

3.1 Nonlinear FDTD Model . . . 64
3.2 HF Cross Modulation . . . 69

3.2.1 Heating and Cooling . . . 71
3.2.2 Model Input Observations . . . 73
3.2.3 Experiment vs Simulation . . . 78
3.2.4 Effective Doppler Shifts . . . 82
3.3 High Frequency Oscillations . . . 82
3.3.1 Electron Temperature Oscillations . . . 83
3.3.2 Electron Density Oscillations . . . 85
3.4 Thermal Cubic Nonlinearity . . . 87
3.4.1 Dominant Mechanism . . . 87
3.4.2 Generated Frequency Dependence . . . 91

4 PLASMA FDTD INCLUDING CONVECTION AND CONDUCTION . . . 94

4.1 Moments of the Boltzmann Equation . . . 94
4.2 VLF Heating . . . 99
4.2.1 First-Order Moment . . . 101
4.2.2 Second-Order Moment . . . 109
4.2.3 Second-Order Moment's Dependence on First-Order Moment . . . 113
4.2.4 Discussion . . . 115
4.3 HF Heating . . . 117

5 ANALYSIS OF LIGHTNING SKYWAVES . . . 121

5.1 Non-Möbius Lightning FDTD Model . . . 121
5.2 Möbius Lightning FDTD Model . . . 124
5.3 Skywave Reflection Height . . . 127
5.3.1 Linear vs Nonlinear Model . . . 127
5.3.2 Dependence on Return Stroke Peak Current . . . 129
5.3.3 Dependence on Ambient Profile . . . 132
5.3.4 Dependence on Calculation Method . . . 133
5.4 Frequency Dependent Reflection Height . . . 136

6 SUMMARY AND SUGGESTIONS FOR FUTURE WORK . . . 140

6.1 Summary of Contributions . . . 140
6.2 Suggestions for Future Research . . . 141
6.2.1 Improved HF Heating Model . . . 141
6.2.2 Improved Lightning Model . . . 142
6.2.3 Moments of the Boltzmann Equation: VLF and HF . . . 143

APPENDIX: LINEAR METHOD UPDATE COEFFICIENTS . . . 144

REFERENCES . . . 148

BIOGRAPHICAL SKETCH . . . 159

LIST OF TABLES

Table page

2-1 Faraday rotation error 47

2-2 Reflection and transmission error 48

2-3 FDTD memory requirement 61

2-4 FDTD FLOPs requirement 62

5-1 Method based reflection height 134

LIST OF FIGURES

Figure page

1-1 Ionospheric electron density versus altitude 13

1-2 Lightning skywave propagation schematic 18

1-3 1-D FDTD grid 21

2-1 Unit step and impulse response with Möbius transformation 45

2-2 Faraday rotation with Möbius transformation 46

2-3 Numerical coefficient properties for an electron only plasma 49

2-4 Numerical coefficient properties for a collisional plasma 50

2-5 Numerical coefficient properties for an anisotropic plasma 51

2-6 Numerical absorption and propagation constants for an anisotropic plasma 52

2-7 Numerical coefficients for a collisional anisotropic plasma 53

2-8 Numerical absorption and propagation constants for a collisional anisotropic plasma 54

2-9 Numerical coefficients for a collisional anisotropic plasma: Möbius vs non-Möbius . . 56

2-10 FDTD comparison: iteration basis 58

2-11 FDTD comparison: simulation basis 59

3-1 Cross-modulation schematic 70

3-2 Electron temperature and collision frequency: heating cycle 72

3-3 Electron temperature and collision frequency: cooling cycle 73

3-4 Ambient density and temperature profiles 74

3-5 Cross-modulation magnitude and phase versus neutral profile 75

3-6 Cross-modulation magnitude and phase versus electron density profile 76

3-7 Cross-modulation magnitude and phase versus radiated HF power 77

3-8 Cross-modulation: experiment and simulation comparison 79

3-9 Cross-modulation: experiment and simulation overlay 81

3-10 Effective doppler shift: experiment versus simulation 83

3-11 Electron temperature oscillations at combination frequencies 84

3-12 Thermal cubic nonlinearity: electron density changes . . . 85
3-13 Thermal cubic nonlinearity: electron density oscillations . . . 86
3-14 Thermal cubic nonlinearity: electric field, collision frequency, and current density . . 89
3-15 Thermal cubic nonlinearity: frequency dependence . . . 92
4-1 Terms of the first order moment: $\hat{\mathrm{x}}$-components . . . 103
4-2 Plasma current density: logarithmic scale . . . 104
4-3 Terms of the first order moment: $\hat{\mathrm{z}}$-components . . . 106
4-4 Terms of the first order moment: magnitude . . . 108
4-5 VLF heating: electron temperature . . . 111
4-6 VLF heating: collision frequency . . . 112
4-7 VLF heating: comparison of Joule heating terms . . . 113
4-8 Electron temperature dependence on first-order moment . . . 114
4-9 HF heating: Joule heating term comparison . . . 118
4-10 HF heating: Joule heating term spectral content . . . 119
5-1 Non-Möbius: dependence on FDTD model . . . 123
5-2 Ionospheric conductivity at 80 km versus electric field strength . . . 126
5-3 Lightning EMP propagation . . . 128
5-4 Linear versus nonlinear simulations . . . 129
5-5 Dependence on return stroke peak current . . . 130
5-6 Reflection height vs return stroke peak current . . . 131
5-7 Dependence on ambient electron density profile . . . 132
5-8 Separation of lightning groundwave and skywave . . . 135
5-9 Linear and nonlinear simulations of skywaves . . . 136
5-10 Spectral content . . . 137
5-11 Reflection height versus frequency . . . 138

Abstract of Dissertation Presented to the Graduate School
of the University of Florida in Partial Fulfillment of the
Requirements for the Degree of Doctor of Philosophy

APPLICATION OF THE MÖBIUS TRANSFORMATION TO NONLINEAR FDTD SIMULATIONS OF THE IONOSPHERE

By

Anthony Joseph Erdman

December 2019

Chair: Robert C. Moore
Major: Electrical and Computer Engineering

Nonlinear processes in the D-region ionosphere (50 to 100 km altitude) produced by high-power Very Low Frequency (VLF, 3 - 30 kHz) and High Frequency (HF, 3 - 30 MHz) radio wave propagation are investigated through numerical simulations, and the results are compared against experimental observations and analytical solutions.

There are many ways to discretize Maxwell's Equations. Five different Finite-Difference Time-Domain (FDTD) methods implementing a linear cold plasma and discretized using the Möbius transformation are analyzed for their performance including memory, speed, accuracy, and stability. The methods are compared to analytical solutions for a cold plasma and excellent accuracy is demonstrated. It is found that by applying the Möbius transformation, all methods maintain the same stability criteria as a standard FDTD implementation of free space. Additionally, by applying the Möbius transformation, all methods accurately simulate a cold plasma and produce nearly identical numerical results.

Having analyzed a number of different linear methods, an optimal nonlinear method is selected to model HF heating of the D-region ionosphere, using the 1^{st}- and 2^{nd}-order moments of the Boltzmann Equation discretized using the Möbius transformation. This model is unique in its ability to directly calculate high frequency oscillations of electron temperature, electron density, and electron-neutral collision frequency. HF cross-modulation experiments are simulated and compared to experimental observations with excellent agreement. Thermal cubic nonlinearity experiments are also simulated and show that the dominant mechanism is a mixing

of the electron-neutral collision frequency at $|\omega_2 - \omega_1|$ with the plasma current density at ω_1 in polar regions.

The 1^{st}- and 2^{nd}-order moments of the Boltzmann Equation derived including the convective derivative are presented. All terms are investigated for their impact on the plasma current density and electron temperature for heating at VLF frequencies. It is shown that the Joule heating term is the most significant for electron temperature heating and that the additional terms in the 1^{st}-order moment may play a detectable role for the plasma current density.

A 2-D, cylindrically symmetric nonlinear lightning heating model of the D-region ionosphere is created with update equations discretized using the Möbius transformation. This model is used to analyze the effects of self-action produced by electric field heating of the ionosphere on the effective reflection height of the skywave. Skywaves are simulated to penetrate deeper into the ionosphere in the nonlinear version of the model compared to the linear version of the model at all return stroke peak currents simulated (1 kA to 200 kA).

CHAPTER 1
INTRODUCTION

This Ph.D. dissertation is focused on electromagnetic wave propagation through the collisional, magnetized plasma of the D-region ionosphere (50 km to 100 km altitude). Linear and nonlinear phenomena are investigated using Finite-Difference Time-Domain (FDTD) modeling, and simulation results are compared against analytical solutions and experimental observations. This dissertation begins with a brief background of the ionosphere, lightning, and FDTD, and lists the scientific contributions of this work. Chapter 2 includes an analysis of five linear plasma FDTD methods which are discretized using the Möbius Transformation. Chapter 3 presents the results of a nonlinear HF heating FDTD model for the D-region ionosphere and a comparison of simulation results with experimental observations. Chapter 4 analyzes the 1^{st}- and 2^{nd}-order moments of the Boltzmann equation derived including the convective derivative and shows that the version of the Joule heating term impacts electron temperature heating the strongest. Chapter 5 discusses the results of a nonlinear lightning FDTD model simulating the increased electromagnetic pulse (EMP) penetration into the ionosphere due to self-action and makes concrete predictions for ground-based observations. Chapter 6 summarizes the scientific contributions presented in this work and suggests future research directions.

1.1 The Ionosphere and Ionospheric Modification

The ionosphere is a plasma layer surrounding the earth between ~50 km and 1000 km altitude. The important charged species for radio wave propagation through the ionosphere are free electrons, and example electron density profiles for nighttime and daytime are shown in Figure 1-1. These ionospheric profiles were created using the International Reference Ionosphere (IRI) 2016 for 03-May-2012 at the geographic location (62.39° N, 145° W) at local 12 AM, midnight, and 12 PM, noon.

The ionosphere is nominally divided into three layers called the D-region (50 km to 100 km), E-region (100 km to 150 km), and F-region (150 km and above). During the day, ionization of the ionosphere is predominantly caused by extreme ultraviolet and x-ray radiation

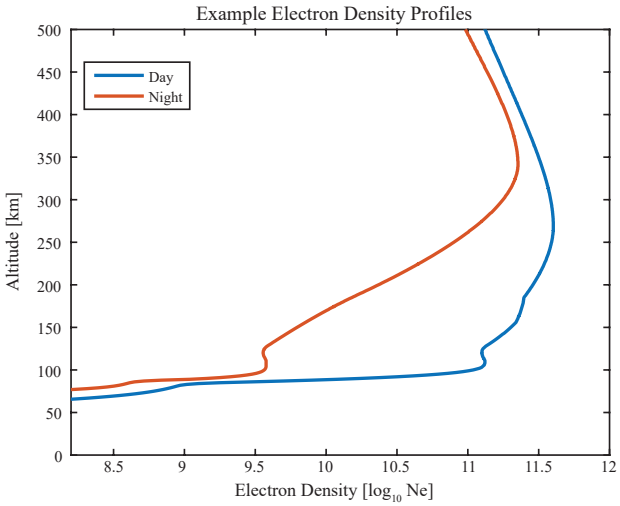

Figure 1-1. Example electron density profile of the ionosphere above HAARP (62.39° N, 145° W) at local 12 AM, 'Night', and 12 PM, 'Day'.

from the sun, and at nighttime the D- and E-regions are maintained through cosmic radiation from extrasolar sources [*Chapman*, 1931a,b, 1939; *Rishbeth and Garriott*, 1969; *Hargreaves*, 1979]. Figure 1-1 shows the dramatic difference in the electron density versus altitude profiles of the nighttime and daytime ionosphere.

High-power electromagnetic (EM) waves propagating through the D-region ionosphere meaningfully interact with the background cold plasma, producing significant changes in electron temperature and chemical composition [*Bailey and Martyn*, 1934; *Ratcliffe*, 1959; *Stubbe and Kopka*, 1977; *Gurevich*, 1978; *Budden*, 1985]. These heating and chemical changes to the background cold plasma in turn modify the electron-neutral collision frequency and the electron density, which control the rate of absorption and the phase propagation constant of the radio wave. In other words, the conductivity of the ionosphere is altered by these waves, in turn affecting the propagation of the same radio waves: i.e., self-action [*Gurevich*, 1978]. The ionospheric modification therefore changes the way that the waves propagate through the ionosphere and leads to nonlinear effects such as self-absorption, cross-modulation, and the generation of "combination" frequencies [*Getmantsev et al.*, 1974].

Three sources of these modifying waves are considered: 1) high-power, ground-based High Frequency (HF, 3 - 30 MHz) ionospheric heaters, 2) Very Low Frequency (VLF, 3 kHz - 30

kHz) transmitters, and 3) lightning. Man-made high-power radio wave transmitters that are capable of significantly modifying the overlying ionosphere exist around the world. There are a few ionospheric heaters (HF transmitters directed vertically) around the world, such as the High-frequency Active Auroral Research Program (HAARP) Observatory in Gakona, Alaska, the Arecibo Observatory in Arecibo, Puerto Rico, the European Incoherent Scatter Scientific Association (EISCAT) heater located near Tromsø, Norway, and the Sura Heater located near Vasilsursk, Russia. Among the ionospheric heaters, HAARP is by far the most flexible and versatile transmitter. The experimental observations used in this work were performed near HAARP, which is a 12x15 phased array capable of transmitting between 2.8 and 10 MHz with a total radiated power of 3.6 MW and an ERP of 1 GW. There are also numerous transmitters in the VLF range operated by Navies for submarine communications such as NAA (24 kHz) in Cutler, ME, USA with an estimated total radiated power of 1 MW, and NLK (24.8 kHz) in Jim Creek, WA, USA with an estimated total radiated power of 250 kW [*Rodriguez*, 1994]. In this work, we will use VLF sources to explore the relative importance of convective derivative terms in various moments of the Boltzmann Equation. Lightning, on the other hand, is a natural, nearly world-wide phenomenon with a global average flash rate of ~100 flashes per second. Lightning can also significantly modify the overlaying ionosphere, resulting in electron density and temperature changes and even produce dielectric breakdown.

1.1.1 Ionospheric Heating by Man-Made HF Transmitters

At ionospheric heaters like HAARP, the conductivity of the ionosphere can be modified by purposefully selecting the power, frequency, polarization, modulation scheme (e.g., sine, square wave, CW), modulation frequency, HF beam direction, and HF beam pattern transmitted. A wide range of ionospheric heating experiments investigate the nonlinear interactions in the ionosphere.

Tellegen [1933] presented the first example of nonlinear radio wave interaction in the ionosphere when the Luxembourg broadcasting station was picked up on another radio station that propagated through the same ionospheric region. This led to the initial theory

behind nonlinear interactions in the ionosphere presented by *Bailey and Martyn* [1934]. This phenomenon became known as the Luxembourg Effect and is scientifically referred to as cross-modulation. The theory behind cross-modulation was addressed quantitatively by *Huxley and Ratcliffe* [1949]. More recent HF heating experiments of cross modulation have been performed by *Senior et al.* [2010] at EISCAT and *Langston and Moore* [2013] at HAARP.

A primary focus of modulated ionospheric heating experiments is Extremely Low Frequency (ELF, 3 Hz - 3 kHz) and VLF wave generation [e.g., *Stubbe et al.*, 1982; *James et al.*, 1984; *Ferraro et al.*, 1984; *Barr et al.*, 1985; *Rietveld et al.*, 1989; *Barr and Stubbe*, 1991; *Milikh et al.*, 1999; *Moore et al.*, 2006; *Moore*, 2007; *Moore et al.*, 2007; *Moore and Agrawal*, 2011; *Moore et al.*, 2012; *Cohen et al.*, 2008, 2010, 2012b; *Agrawal and Moore*, 2012; *Cohen and Golkowski*, 2013; *Fujimaru*, 2014; *Getmantsev et al.*, 1974]. The theory for these experiments was first presented by *Stubbe and Kopka* [1977] and relies upon a naturally forming DC current in the ionosphere known as the auroral electrojet. Modulating the conductivity of the ionosphere at ELF/VLF frequencies in the presence of the electrojet also modulates the current of the electrojet. This creates a giant radiating antenna at the modulation frequency and its harmonics in the D-region ionosphere. Electrojet dependent ELF/VLF wave generation techniques include amplitude modulation, beat-wave modulation, Synthesized Two Frequency (STF) modulation, interharmonic modulation, frequency-time multiplexing, beam-painting, and geometric modulation, among others. Due to the low propagation loss of ELF/VLF waves bound by the earth-ionosphere waveguide, these generated signals can propagate thousands of kilometers [*Moore et al.*, 2007] and be injected into the magnetosphere as whistler mode waves [*Inan et al.*, 2004; *Golkowski et al.*, 2008, 2009, 2010].

The above methods for ELF/VLF wave generation are all dependent on the presence of an electrojet current, the strength of which varies with time. To more reliably create ELF/VLF waves using modulated HF heating, other techniques are needed. *Papadopoulos et al.* [2011a,b] presented modeling results and experimental observations of Ultra Low Frequency (ULF, below 3 Hz) and ELF generation through modulated F-region heating in the absence of

electrojet currents. The thermal cubic nonlinearity is another electrojet independent method for ELF/VLF wave generation. This technique was demonstrated (albeit with $<$1 dB SNR) in Russia using HF transmitters by *Kotik and Ermakova* [1998]. The effect was demonstrated much more clearly in Norway, using VLF transmitters by *Barr* [1996], and in Alaska using HAARP by *Moore et al.* [2013]. The thermal cubic nonlinearity involves the interaction of two high-power radio waves in the D-region ionosphere with frequencies ω_1 and ω_2 where $|\omega_2 - 2\omega_1|$ is in the ELF/VLF range. *Gurevich* [1978] and *Kotik and Ermakova* [1998] suggested that the mechanism leading to the ELF/VLF wave generation is a mixing of the collision frequency at $2\omega_1$ with a plasma current density at ω_2 to produce a source current density at $|\omega_2 - 2\omega_1|$. *Moore et al.* [2013] presented numerical modeling showing that the ELF/VLF source in polar regions is instead produced by a mixing of the collision frequency at $|\omega_2 - \omega_1|$ with the plasma current density at ω_1.

1.1.2 Ionospheric Heating by Man-Made VLF Transmitters

VLF heating of the lower ionosphere was theoretically discussed in detail by *Galejs* [1972] in which the D-region was modeled at nighttime as a homogenous, magnetized plasma with a sharp boundary at 85 km. *Galejs* [1972] predicted electron temperature increases of 10% for a 1000 kW transmitter. *Rodriguez* [1994] performed a controlled VLF heating experiment by cycling the the NAA VLF transmitter OFF and ON and measuring the effect on the NSS (21.4 kHz, 265 kW, Annapolis, MD) VLF transmitter signal. It was found that the NSS signal recorded in Gander, Newfoundland increased in amplitude up to 0.84 dB and retarded in phase by as much as 5.3°. *Marshall* [2014] utilized a nonlinear FDTD model to investigate the effects of VLF transmitter power and frequency, and magnetic dip angle on a nighttime ionosphere. Daytime effects were not investigated due to the increased electron density, which in the model of *Marshall* [2014] requires an extremely small time-step to maintain stability. Absorption of trans-ionospheric propagating VLF waves from ground based transmitters have been simulated and compared with experimental observations by *Cohen et al.* [2012a] and *Graf et al.* [2013]. Simulations by *Cohen et al.* [2012a] and *Graf et al.* [2013] utilized the

model detailed in *Lehtinen and Inan* [2008, 2009] which does not include electron temperature heating or electron density changes.

1.2 Ionospheric Effects of Lightning

Lightning produces strong quasi-static fields and radiates EM waves across the frequency spectrum and typically at a significantly higher power than most man-made transmitters. These fields and waves are capable of heating and ionizing the overlying ionosphere creating disturbances known as "transient luminous events" (TLEs), which include elves, sprites, sprite halos, blue starters, blue jets, and gigantic jets [*Inan et al.*, 2010]. Elves were first discovered visually by *Boeck et al.* [1992] and are a result of the radiated EMP. They are observed optically for less than 1 ms [*Newsome and Inan*, 2010] as red bursts of light [*Taranenko et al.*, 1993a] between 85 km to 100 km altitude and up to 700 km radially [*Barrington-Leigh and Inan*, 1999; *Wescott et al.*, 2001]. Sprites and sprite halos are caused by the lightning quasi-electrostatic field and were first discovered by *Franz et al.* [1990] after being predicted by *Wilson* [1924]. Sprites are seen between 50 km and 95 km [*Sentman et al.*, 1995] whereas sprite halos are seen around 70 km to 85 km with a radial extent of 40 km to 85 km [*Barrington-Leigh et al.*, 2001]. Blue jets are electrical sparking above the thundercloud top reaching an altitude of 40 km to 50 km [*Boeck et al.*, 1995; *Wescott et al.*, 1995]. Blue starters are very similar to blue jets, but only reach an altitude of 25 km [*Wescott et al.*, 1996]. Gigantic jets were first observed by *Pasko et al.* [2002] and are upward lightning discharges reaching 90 km altitude [*Su et al.*, 2003].

The EMP from a lightning strike is capable of propagating thousands of kilometers in the Earth-Ionosphere (EI) waveguide. The one-hop skywaves examined here reflect from the lower ionosphere once before being received at the recording station on the ground as depicted in Figure 1-2. Due to the increased path length of the skywave, the groundwave and skywave can be separated from each other in the time-domain. By using the time-delay between respective parts of the groundwave and skywave, the effective skywave reflection height can be determined [*McDonald et al.*, 1979; *Carvalho et al.*, 2017]. Used predominantly

in Chapter 5 of this work is the peak-to-peak method which uses the time delay between the peak vertical electric field on the ground of the skywave and the groundwave to calculate the effective skywave reflection height. The slow-breakpoint and fast-breakpoint were identified by *McDonald et al.* [1979] and the slow/fast-breakpoint methods use the time delay between the start of the groundwave to the slow/fast-breakpoint to calculate an effective skywave reflection height. This time domain method produces an *effective* reflection height because the ionosphere is a dispersive and vertically stratified media and all frequencies will typically reflect at slightly different altitudes [*Westcott*, 1962a,b].

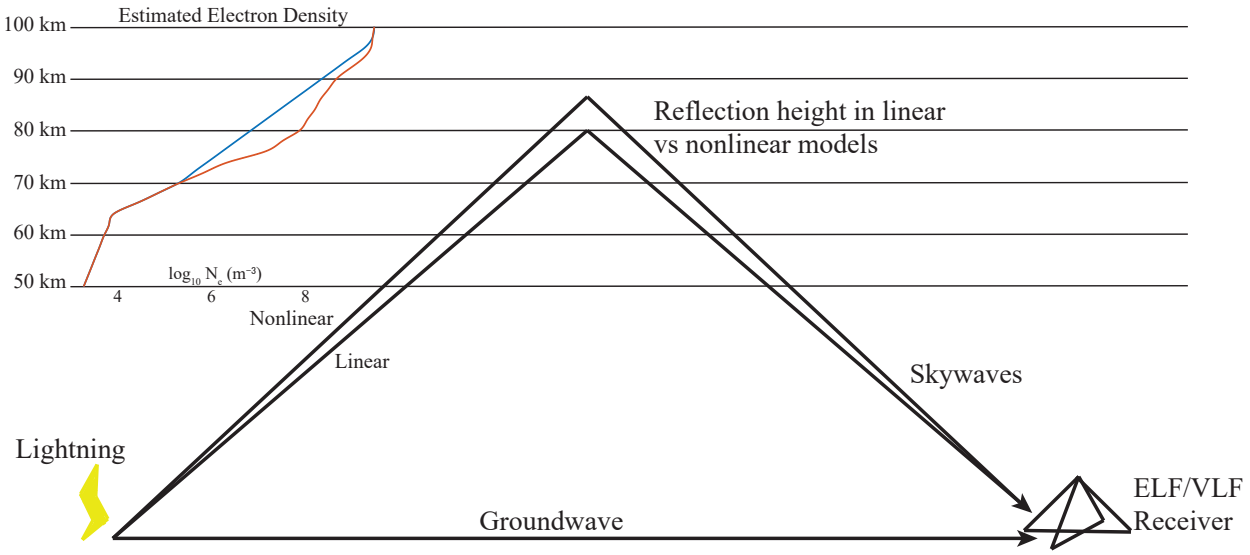

Figure 1-2. Depiction of a lightning skywave and groundwave propagation to a VLF receiver. In the upper left, example estimated electron density profiles are shown.

Lightning can be used as a source to probe and characterize the ionosphere [e.g., *Cheng and Cummer*, 2005; *Han and Cummer*, 2010a,b; *Han et al.*, 2011; *Obenberger et al.*, 2018; *McCormick et al.*, 2018; *Malins et al.*, 2019]. Previous works have shown that lightning can modify the electron density and electron temperature of the overlying ionosphere [e.g., *Taranenko et al.*, 1993b; *Pasko et al.*, 1997; *Barrington-Leigh*, 2000; *Cheng and Cummer*, 2005; *Marshall et al.*, 2010; *Marshall*, 2012, 2014; *Shao et al.*, 2013; *Lay et al.*, 2014; *Kotovsky and Moore*, 2016a,b; *Koh et al.*, 2019]. Previous studies that have analyzed skywave reflection heights from a lightning discharge have used linear models that do not include the effects of

ionization changes or electron temperature modifications [e.g., *Cheng and Cummer*, 2005; *Jacobson et al.*, 2009a,b; *Han and Cummer*, 2010a,b; *Han et al.*, 2011; *Haddad et al.*, 2012; *Somu et al.*, 2015; *Carvalho et al.*, 2017; *Tran et al.*, 2017; *McCormick et al.*, 2018; *Qin et al.*, 2019; *Mostajabi et al.*, 2019]. Recent studies have used nonlinear models to analyze ionospheric changes due to lightning [e.g., *Taranenko et al.*, 1993b; *Pasko et al.*, 1997; *Kuo et al.*, 2007, 2012; *Marshall et al.*, 2010; *Marshall*, 2012, 2014; *Liu*, 2012; *Luque et al.*, 2014; *Kotovsky and Moore*, 2016a,b, 2017; *Gordillo-Vazquez et al.*, 2016], but have not directly investigated skywave propagation. *Salem et al.* [2015] created a 1-D model to solve for the steady-state, modified from ambient, electron density profile at nighttime caused by the electrostatic fields present above a thunderstorm. This model was expanded to include the effects of collision frequency changes by *Salem et al.* [2016] and the effect on ELF/VLF reflection heights were determined. A model that includes the time-varying nonlinearities of electron density and collision frequency changes in conjunction with the quasi-electrostatic and radiated EMP is needed to investigate the effect on skywave propagation from a lightning return stroke.

1.3 Finite-Difference Time-Domain

The Finite-Difference Time-Domain (FDTD) method is used in this work to model linear and nonlinear wave interactions with the ionosphere from VLF and HF ionospheric heaters and lightning. The FDTD method was initially proposed by *Yee* [1966] to handle isotropic and non-dispersive media. Fundamentally, FDTD works by discretizing the two Maxwell curl equations (Ampere's Law (Eq. 1-1) and Faraday's Law (Eq. 1-2)) in time and space. Implementation of these equations naturally satisfy $\nabla \cdot \vec{D}_{\text{eff}} = 0$ and $\nabla \cdot \vec{B} = 0$, but also allow $\nabla \cdot (\epsilon_0 \vec{E}) = \rho$ to be calculated after the fact.

$$\nabla \times \vec{H} = \vec{J} + \epsilon_0 \frac{\partial \vec{E}}{\partial t} = \frac{\partial \vec{D}_{\text{eff}}}{\partial t} \tag{1-1}$$

$$\nabla \times \vec{E} = -\mu_0 \frac{\partial \vec{H}}{\partial t} \tag{1-2}$$

In Eq. 1-1, $\vec{D}_{\text{eff}}$ is an effective electric flux density, written throughout the rest of this work as $\vec{D}$. By offsetting the electric and magnetic field in time and space, visualized in Figure 1-3, it is possible to leapfrog each forward in time, solving for wave propagation. Since the original method was proposed, several FDTD techniques have advanced to model a linear, dispersive anisotropic cold plasma, of which two main method groups have been used and developed widely: recursive convolution (RC) [e.g., *Luebbers et al.*, 1990, 1991; *Hunsberger et al.*, 1992; *Kelley et al.*, 1996] and direct integration (DI) [e.g., *Nickisch and Franke*, 1992; *Young*, 1994; *Cummer*, 1997; *Young and Nelson*, 2001; *Hu and Cummer*, 2006; *Yu and Simpson*, 2010]. The RC group includes the original first-order accurate method [*Luebbers et al.*, 1991] and the later piecewise-linear RC (PLRC) [*Kelley et al.*, 1996] method which provides second-order accuracy. For modeling the ionosphere, *Cummer* [1997] found that the PLRC method is more accurate than the DI method for a fixed computational effort, but that the stability criteria of the PLRC method depends on the plasma parameters. In nonlinear simulations of ionospheric heating experiments and lightning, the plasma parameters such as the electron density and collision frequency can change every iteration. This effect makes the stability criteria and maximum time-step unknown at the start of the simulation and for this reason, the RC group of methods will not be investigated further in this dissertation.

This work focuses on the DI group of methods because of their comparable accuracy to PLRC methods, their ability to maintain a stability criteria the same as a free-space FDTD implementation, and their direct applicability to nonlinear media. When modeling a cold plasma, the DI method discretizes Maxwell's equations coupled with an auxiliary ordinary differential equation (ADE). For a linear cold plasma, the ADE is typically the expression for the plasma current density (Eq. 1-3) derived using magneto-ionic theory [*Budden*, 1985].

$$\frac{\partial}{\partial t}\vec{J} = \frac{q_e^2 N_e}{m_e}\vec{E} + \frac{q_e}{m_e}\vec{J} \times \vec{B}_0 - \nu\vec{J} \tag{1-3}$$

Eq. 1-3 is the 1^{st}-order moment of the Boltzmann Equation, also known as the momentum transport equation, derived neglecting the convective derivative. Discussed in

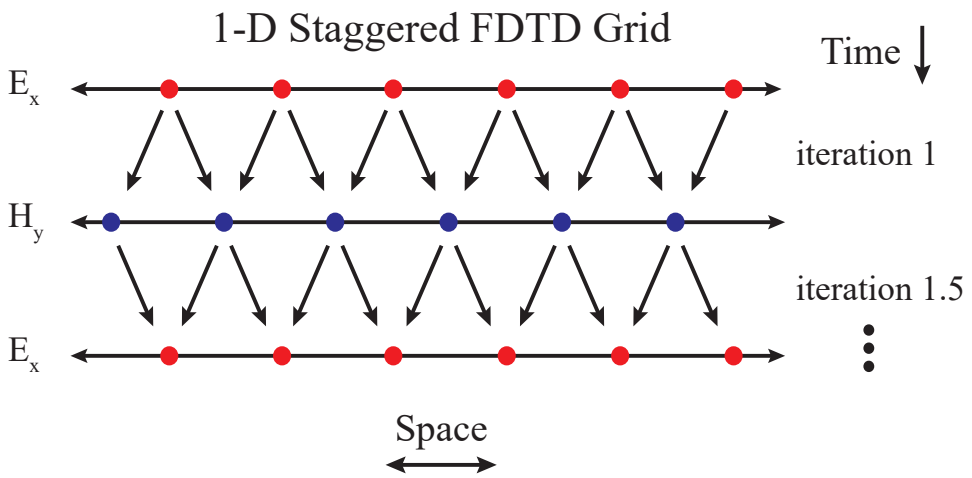

Figure 1-3. Depiction of a 1-D FDTD grid with the electric field and magnetic flux density offset in time and space. Surrounding field points at a previous time-step are used to update the new field value.

Chapter 4 is the 1^{st}-order moment of the Boltzmann Equation derived including the convective derivative. A plasma current density of the form shown in Eq. 1-3 is appropriate for modeling ELF/VLF propagation in the Earth-Ionosphere waveguide where significant heating of the ionosphere does not occur. Various cold plasma FDTD methods utilizing an ADE have been developed and presented over the years including those by *Nickisch and Franke* [1992], *Young* [1994], and *Cummer* [1997]. *Cummer* [1997] found that *Nickisch and Franke* [1992] is unstable if $\nu \neq 0$ and the stability of *Young* [1994] depends on the plasma parameters. These methods were originally presented to handle an isotropic, non-magnetized cold plasma. *Hu and Cummer* [2006] expanded the method from *Cummer* [1997] to include a vertical magnetic field in a 2-D cylindrical model. This method was presented in more detail for 3-D Cartesian coordinates with an arbitrarily directed background magnetic field by *Yu and Simpson* [2010] and both implementations are found to maintain the same stability criteria as a free-space FDTD implementation by the authors.

The cross product of the plasma current density and background magnetic field in Eq. 1-3 requires that all components of the plasma current density are solved simultaneously. To overcome this requirement, some DI methods manipulate the plasma current density in order

to create a relationship between $\vec{E}$ and $\vec{D}$ through an effective permittivity. This relationship serves as the ADE for these methods and will be shown in Chapter 2 for an anisotropic cold plasma. Although it was for Debye and Lorentz media, this style of ADE was first presented by *Joseph et al.* [1991], followed by *Gandhi et al.* [1993] for a two-relaxation Debye medium. *Young and Nelson* [2001] expanded and presented this method for an isotropic cold plasma. *Gamliel* [2017] built upon this work and derived an anisotropic cold plasma method. This dissertation investigates possible reasons why some of these implementations behave better than others.

1.3.1 Möbius Transformation

An FDTD method for an anisotropic cold plasma in which the stability factor does not rely upon the plasma parameters is extremely beneficial in reducing computational run-time and is important for future nonlinear implementations. When the stability factor is dependent on the plasma parameters, the time-step can be limited to a value much smaller than a non-dependent implementation. This causes significantly longer simulation run times, which *Hu and Cummer* [2006] showed could be an order of magnitude longer. This effect is especially apparent for a nonlinear implementation in which the plasma parameters change dynamically. The maximum and minimum of the plasma parameters are not necessarily known beforehand, and it is unknown what the maximum allowed time step is.

The discretization of Mth-order dispersive media by means of the Möbius transformation (MT) addresses this problem and was first applied to FDTD by *Pereda et al.* [2002]. The MT stably maps the poles of a continuous system to a discrete system. A benefit of the MT is that a stable system in the continuous domain maintains its stability in the discrete domain. Discretization using the MT of a continuous-time system in the frequency domain was shown by *Pereda et al.* [2002] to be the following mapping of ω:

$$j\omega \rightarrow \frac{2j}{\Delta_t}\frac{sin(\omega\Delta_t/2)}{cos(\omega\Delta_t/2)} = j\frac{W}{V} \tag{1-4}$$

where we define:

$$jW = \frac{2j}{\Delta_t} sin(\omega \Delta_t / 2) = \frac{e^{\frac{j\omega\Delta t}{2}} - \frac{-j\omega\Delta t}{2}}{\Delta t} \tag{1-5}$$

and

$$V = cos(\omega \Delta_t / 2) = \frac{e^{\frac{j\omega\Delta t}{2}} + \frac{-j\omega\Delta t}{2}}{2}. \tag{1-6}$$

Discretization of a continuous-time system $(F(t))$ to a discrete-time system (F^n) in the time domain utilizes the following time-derivative mapping:

$$\frac{d^m}{dt^m} F(t) \rightarrow (j\omega)^m F(\omega) \rightarrow \left(j\frac{W}{V} \right)^m F\left(\frac{W}{V} \right) \tag{1-7}$$

where m is the order of the differential, and j is $\sqrt{-1}$. The first mapping in Eq. 1-7 is the Fourier transform from the time domain to the frequency domain and the second mapping is the Möbius transformation in the frequency domain.

In the frequency domain, one may then multiply all terms by appropriate powers of W and V so that no W's or V's remain in the denominator of any one term. The inverse Fourier transform of V can be seen to be an average of the terms spaced $\frac{\Delta t}{2}$ and $\frac{-\Delta t}{2}$ from any point in time. Similarly, the inverse Fourier transform of W represents the differential between two terms spaced in time and separated by Δt.

Previous works such as those by *Hu and Cummer* [2006], *Yu and Simpson* [2010], and *Gamliel* [2017] have created anisotropic plasma FDTD models with update equations discretized the same way as if using the MT, although none explicitly mention use of the MT. Serendipitously, their implementation of centered differencing along with centered averaging led to implementations the same as if the MT had been utilized. *Gamliel* [2017] did not recognize the MT and used the substitution $j\omega^m \rightarrow jW^m V^{M-m}$, where it was required to know the highest order derivative in advance of MT application. From this description, it is seen that the "stencil generator" of *Gamliel* [2017] is similar, but not the same as implementing Eq. 1-7. In this work, the MT is used to discretize the update equations for each linear method presented in Chapter 2. A linear method discretized using the MT from Chapter 2 is then used as the basis for the nonlinear models presented in Chapter 3, Chapter 4, and Chapter 5.

The methods of *Hu and Cummer* [2006], *Yu and Simpson* [2010], *Gamliel* [2017], and those presented in this work have found that the stability factor is not a function of the plasma parameters. The ability to create a cold plasma FDTD with a stability condition the same as a free space FDTD implementation, regardless of the plasma parameters, is a strong motivating factor to use the Möbius transformation to discretize the FDTD update equations. This motivating factor is even more important for nonlinear implementations which can have the plasma parameters change every iteration.

Although a number of cold plasma FDTD models exist, a comparative analysis, especially one including the effects of the MT has not yet been completed (until this dissertation). The five method's analyzed in Chapter 2 are derived starting with fundamentally the same three equations which are Ampere's Law (Eq. 1-1), Faraday's Law (Eq. 1-2), and momentum-transfer (Eq. 1-3), but the implementations range from first-order to twelfth-order. The range in order may produce significant differences between the five methods and trade-offs may exist between memory, speed, and accuracy. For example, the second-, first- and zeroth-order differentials for a second-order differential system as given by the MT are:

$$\frac{\partial^2 f^n}{\partial t^2} = \frac{1}{(\Delta t)^2}\left(f^{n+1} - 2f^n + f^{n-1}\right) \Leftrightarrow (jW)^2 \tag{1-8}$$

$$\frac{\partial^1 f^n}{\partial t^1} = \frac{1}{2(\Delta t)^1}\left(f^{n+1} + 0f^n - f^{n-1}\right) \Leftrightarrow jWV \tag{1-9}$$

$$\frac{\partial^0 f^n}{\partial t^0} = \frac{1}{4(\Delta t)^0}\left(f^{n+1} + 2f^n + f^{n-1}\right) \Leftrightarrow V^2. \tag{1-10}$$

Note that the last term uses the average value of the field, not just the field at time step n.

For a fourth-order differential system, however, the fourth through zeroth-order differentials as given by the MT are:

$$\frac{\partial^4 f^n}{\partial t^4} = \frac{1}{(\Delta t)^4}\left(f^{n+2} - 4f^{n+1} + 6f^n - 4f^{n-1} + f^{n-2}\right) \Leftrightarrow (jW)^4 \tag{1-11}$$

$$\frac{\partial^3 f^n}{\partial t^3} = \frac{1}{2(\Delta t)^3}\left(f^{n+2} - 2f^{n+1} + 0f^n + 2f^{n-1} - f^{n-2}\right) \Leftrightarrow (jW)^3 V \tag{1-12}$$

$$\frac{\partial^2 f^n}{\partial t^2} = \frac{1}{4(\Delta t)^2}\left(f^{n+2} + 0f^{n+1} - 2f^n + 0f^{n-1} + f^{n-2}\right) \Leftrightarrow (jW)^2 V^2 \tag{1-13}$$

$$\frac{\partial^1 f^n}{\partial t^1} = \frac{1}{8(\Delta t)^1}\left(f^{n+2} + 2f^{n+1} + 0f^n - 2f^{n-1} - f^{n-2}\right) \Leftrightarrow (jW)^1 V^3 \tag{1-14}$$

$$\frac{\partial^0 f^n}{\partial t^0} = \frac{1}{16(\Delta t)^0}\left(f^{n+2} + 4f^{n+1} + 6f^n + 4f^{n-1} + f^{n-2}\right) \Leftrightarrow V^4. \tag{1-15}$$

It is important to note that discretization using the MT has the effect that all differentials utilize the same number of time steps, which *Gamliel* [2017] described as 'spreading'. For an M^{th}-order differential system, $M + 1$ time steps are required in the differentials. According to the MT, implementing the time-derivatives in this manner is necessary to maintain a plasma-parameter independent stability criteria.

1.3.2 Nonlinear FDTD

The simulation of HF heating experiments and the accurate modeling of lightning skywave propagation requires the use of nonlinear models. For ionospheric modification simulations, nonlinear FDTD models include a temporally and spatially varying electron temperature, electron-neutral collision frequency, and electron density. Nonlinear FDTD methods that model radio wave propagation through the D-region ionosphere have been created and detailed in the literature [*Kuo et al.*, 2007, 2012; *Marshall et al.*, 2010; *Marshall*, 2012, 2014; *Luque et al.*, 2014; *Gordillo-Vazquez et al.*, 2016; *Kotovsky*, 2016; *Kotovsky and Moore*, 2017]. The majority of the methods presented are for lightning interaction with the ionosphere and focus on frequencies in the VLF range. *Marshall* [2014] created a FDTD model that simulated heating from VLF transmitters, but did not include electron density changes. Previous methods to model HF heating of the D-region ionosphere have been implemented such as ray-tracing [*Moore*, 2007], but these methods do not allow for the same direct calculation of HF oscillations of electron density, collision frequency, and electron temperature that the FDTD method allows. Instead, estimates of these HF oscillations must be made in post-calculation [e.g., *Moore et al.*, 2013].

Due to the higher power densities radiated by lightning, attempts to model ionospheric modification from lightning are different than those for man-made transmitters. The nonlinear model that will be used for HF heating simulations is implemented using moments of the Boltzmann Equation; it assumes that a Maxwellian electron energy distribution is valid throughout the heating process, and that average electron energies remain well below ~1 eV. These assumptions are in general valid for ionospheric modification produced by man-made transmitters. Lightning emits enough power to heat electron temperatures in the ionosphere rapidly enough and significantly enough that the assumption of a Maxwellian distribution is not valid. In this case, average electron energies between 1 eV and 10 eV are regularly obtained. Models of nonlinear processes produced by lightning are thus different from those produced by man-made transmitters. In particular, the method to update the ionospheric conductivity is different. The method in the lightning model presented in this work makes the quasi-static heating approximation and uses an empirical model to update the electron mobility [*Pasko et al.*, 1997; *Pasko*, 1998; *Kotovsky*, 2016; *Kotovsky and Moore*, 2017] based on laboratory experiments [*Davies*, 1983; *Hegerberg and Reid*, 1980].

1.4 Scientific Contributions

The contributions to knowledge that are presented in the dissertation are as follows:

- I implemented five different Finite-Difference Time-Domain methods of a magnetized collisional plasma to demonstrate that the application of the Möbius Transformation to FDTD solutions of Maxwell's Equations produces results of similar order accuracy no matter the specific implementation. As a result, if the Möbius Transformation is employed, accuracy is no longer an important trade-off consideration among accuracy, memory usage, and speed.
- I created a nonlinear HF heating FDTD model of the D-region ionosphere based upon the application of the Möbius Transformation to the 1^{st}- and 2^{nd}- order moments of the Boltzmann Equation neglecting convection and conduction. Minor exceptions to the rigorous application of the Möbius Transformation are made for implementation considerations, and these exceptions are fully described. The model includes the ability to directly calculate high-frequency oscillations of electron density, electron temperature, and collision frequency. Data from cross-modulation experiments and thermal cubic nonlinearity experiments at HAARP are compared to simulation results for validation.

- I evaluated the relative importance of nonlinear terms in the 1^{st}- and 2^{nd}- order moments of the Boltzmann Equation, derived accounting for the convective derivative. Results determined the $\frac{1}{\sigma_{||}}\vec{J}\cdot\vec{J}$ term that replaces the $\vec{J}\cdot\vec{E}$ term (derived neglecting convection) has the largest relative impact on electron temperature heating at lower frequencies (i.e., $<$100 kHz). Additional terms of the 1^{st}-order moment are identified as potentially contributing detectably to the plasma current density.

- I applied the Möbius Transformation to numerically simulate the self-action of lightning-generated electromagnetic pulses in the D-region ionosphere, and demonstrated that this self-action produces significantly deeper penetration of skywaves into the ionospheric plasma at all return stroke peak currents. Model simulations support the claim that electron temperature enhancements (rather than changes in electron density) primarily account for this increased penetration.

CHAPTER 2
LINEAR COLD PLASMA FDTD

In this chapter, five different direct integration (DI) FDTD methods are discretized to simulate radio wave propagation in a collisional, anisotropic, electron-only cold plasma. The resulting simulations are compared and contrasted. One method is directly compared to the analytical solutions for a cold plasma for validation. All five FDTD methods are then compared to each other including an analysis of their numerical output, stability, memory, speed, and nonlinear applicability. The first method considered is that presented by *Yu and Simpson* [2010] which couples Maxwell's Equations with the plasma current density. Three additional methods considered use the higher-order ADE based on the relationship between $\vec{D}_{\text{eff}}$ and $\vec{E}$. The fifth method considered is a discretization of the cold plasma wave equation for the electric field. The unique feature of all of these methods in comparison to most other cold plasma FDTD methods is that the update equations are discretized by application of the Möbius transformation as discussed in Chapter 1. One additional implementation discretized without using the Möbius transformation is provided to highlight the importance of the Möbius transformation.

2.1 Linear Methods

The D-region ionosphere (50 - 100 km altitude) is a highly collisional, weakly ionized, and magnetized plasma and electromagnetic wave propagation is governed by Maxwell's Equations:

$$\begin{aligned} \nabla \times \vec{E} &= -\frac{\partial \vec{B}}{\partial t} \qquad \nabla \cdot \vec{D} = \rho \\ \nabla \times \vec{H} &= \vec{J} + \frac{\partial \vec{D}}{\partial t} \quad \nabla \cdot \vec{B} = 0 \end{aligned} \tag{2-1}$$

where $\vec{E}$ is the wave electric field, $\vec{D} = \epsilon \vec{E}$ is the electric flux density, $\vec{H}$ is the wave's magnetic field, $\vec{B} = \mu \vec{H}$ is the magnetic flux density, $\vec{J}$ is the total plasma current density, and ρ is the total charge density. In the D-region, the permittivity (ϵ) and permeability (μ) of the plasma are taken to be their free-space values, which do not vary spatially or temporally. This is because one can regard the plasma as consisting of charged and neutral particles moving

around in free-space. Therefore, $\epsilon = \epsilon_0$ and $\mu = \mu_0$, which allows them to be factored out of the temporal and spatial derivatives in Eq. 2-1. Wave propagation through the plasma is governed then by the modified Maxwell's Equations:

$$\begin{aligned} \nabla \times \vec{E} &= -\mu_0 \frac{\partial \vec{H}}{\partial t} & \nabla \cdot \vec{D}_{\text{eff}} &= 0 \\ \nabla \times \vec{H} &= \vec{J} + \epsilon_0 \frac{\partial \vec{E}}{\partial t} = \frac{\partial \vec{D}_{\text{eff}}}{\partial t} & \nabla \cdot \vec{H} &= 0 \end{aligned} \tag{2-2}$$

where $\vec{D}_{\text{eff}}$ is an effective electric flux density that includes the effects of the permittivity and conductivity, written throughout the rest of the work as $\vec{D}$. For a linear, electron-only plasma, the time variation of the plasma current density is given by the first-order moment of the Boltzmann Equation, neglecting convection, conduction, gravity and the interaction of the wave magnetic field with the medium:

$$\frac{\partial}{\partial t}\vec{J} = \frac{q_e^2 N_e}{m_e}\vec{E} + \frac{q_e}{m_e}\vec{J} \times \vec{B}_0 - \nu \vec{J}. \tag{2-3}$$

N_e is the electron density, q_e is the electron charge, m_e is the electron mass, $\vec{B}_0$ is the background magnetic field, and ν is the effective electron-neutral collision frequency. The first method this paper considers (see Section 2.1.1) couples Eq. 2-3 as the ADE with the modified Maxwell's equations (Eq. 2-2) in order to model the cold plasma. A benefit of using Eq. 2-3 in Method 1 is that it is easy to add multiple charged plasma constituents as is sometimes desirable.

The second, third, and fourth methods analyzed here are derived using the following relationship between the plasma current density $\vec{J}$, the electric field $\vec{E}$, and the effective electric flux density $\vec{D}$:

$$\vec{J} = \frac{\partial \vec{D}}{\partial t} - \epsilon_0 \frac{\partial \vec{E}}{\partial t}. \tag{2-4}$$

This expression is substituted into the momentum transfer equation (Eq. 2-3) in order to obtain the following expression relating $\vec{E}$ to $\vec{D}$:

$$\epsilon_0 \frac{\partial^2 \vec{E}}{\partial t^2} - \epsilon_0 \frac{q_e}{m_e}\left(\frac{\partial \vec{E}}{\partial t} \times \vec{B}_0\right) + \epsilon_0 \nu \frac{\partial \vec{E}}{\partial t} + \frac{q_e^2 N_e}{m_e}\vec{E} = \frac{\partial^2 \vec{D}}{\partial t^2} - \frac{q_e}{m_e}\left(\frac{\partial \vec{D}}{\partial t} \times \vec{B}_0\right) + \nu \frac{\partial \vec{D}}{\partial t}. \quad (2\text{-}5)$$

This equation is similar to that derived by *Young and Nelson* [2001], which was in turn based on the method presented by *Joseph et al.* [1991] for Debye and Lorentz media. In this dissertation it is anisotropic, accounting for a static $\vec{B}_0$, which *Young and Nelson* [2001] neglected. The anisotropy causes the three components of $\vec{E}$ to be coupled to each other and to the three components of $\vec{D}$, in general. The second method this dissertation considers (see Section 2.1.2) couples Eq. 2-5 as the ADE with the modified Maxwell's equations (Eq. 2-2) in order to model the cold plasma.

In a linear plasma, N_e, ν, and B_0 are constant with time. Eqs. 2-2 and 2-3 form a linear system and therefore, frequency domain analysis can be easily implemented. In the frequency domain, Eq. 2-5 may be expressed as follows:

$$-\omega^2 \epsilon_0 \vec{E} - \epsilon_0 \frac{q_e}{m_e}\left(j\omega \vec{E} \times \vec{B}_0\right) + j\omega\epsilon_0 \nu \vec{E} + \frac{q_e^2 N_e}{m_e}\vec{E} = -\omega^2 \vec{D} - \frac{q_e}{m_e}\left(j\omega \vec{D} \times \vec{B}_0\right) + j\omega\nu \vec{D} \quad (2\text{-}6)$$

Without making any assumptions about the direction of $\vec{B}_0$, the effective permittivity tensor that satisfies:

$$\vec{D} = \bar{\bar{\epsilon}}_{\text{eff}} \vec{E} \quad (2\text{-}7)$$

can be expressed [*Ratcliffe*, 1959]:

$$\bar{\bar{\epsilon}}_{\text{eff}} = \epsilon_0 \bar{\bar{I}} + \frac{\epsilon_0 \omega_p^2}{\omega(\omega - j\nu)\left[(\omega - j\nu)^2 - \omega_c^2\right]} \begin{bmatrix} \omega_{cx}^2 - (\omega - j\nu)^2 & \omega_{cx}\omega_{cy} - (\nu + j\omega)\omega_{cz} & \omega_{cx}\omega_{cz} + (\nu + j\omega)\omega_{cy} \\ \omega_{cx}\omega_{cy} + (\nu + j\omega)\omega_{cz} & \omega_{cy}^2 - (\omega - j\nu)^2 & \omega_{cy}\omega_{cz} - (\nu + j\omega)\omega_{cx} \\ \omega_{cx}\omega_{cz} - (\nu + j\omega)\omega_{cy} & \omega_{cy}\omega_{cz} + (\nu + j\omega)\omega_{cx} & \omega_{cz}^2 - (\omega - j\nu)^2 \end{bmatrix} \quad (2\text{-}8)$$

where $\bar{\bar{I}}$ is the identity matrix, ω is the frequency of the wave, $\omega_p = \sqrt{q_e^2 N_e / m_e \epsilon_0}$ is the angular plasma frequency, and $\omega_c = -q_e \vec{B}_0 / m_e = \omega_{cx}\hat{x} + \omega_{cy}\hat{y} + \omega_{cz}\hat{z}$ is the cyclotron frequency. Method 3 (see Section 2.1.4) discretizes Eq. 2-7 coupled with the modified Maxwell's equations (Eq. 2-2) to model the cold plasma. Method 4 (see Section 2.1.5) inverts the effective permittivity as shown in Eq. 2-9 and discretizes this equation coupled with the modified Maxwell's equations (Eqs. 2-2) to model the cold plasma.

$$\vec{E} = \bar{\bar{\epsilon}}_{\text{eff}}^{-1} \vec{D}. \tag{2-9}$$

The derivation of the cold plasma wave equation, which is discretized by Method 5 (see Section 2.1.6), starts with a few manipulations of the modified Maxwell's Equations. The first manipulation is taking an additional curl of Faraday's Law (Eq. 1-2):

$$\frac{\partial}{\partial t} \nabla \times \vec{H} = -\frac{1}{\mu_0} \nabla \times \nabla \times \vec{E}. \tag{2-10}$$

The second manipulation is of Ampere's Law (Eq. 1-1), and it relates the plasma current density to the magnetic and electric field:

$$\vec{J} = \nabla \times \vec{H} - \epsilon_0 \frac{\partial \vec{E}}{\partial t}. \tag{2-11}$$

It will be useful to have an expression of Eq. 2-11 with an additional one and two time derivatives performed:

$$\begin{aligned} \frac{\partial \vec{J}}{\partial t} &= \frac{\partial}{\partial t} \nabla \times \vec{H} - \epsilon_0 \frac{\partial^2 \vec{E}}{\partial t^2} \\ \frac{\partial^2 \vec{J}}{\partial t^2} &= \frac{\partial^2}{\partial t^2} \nabla \times \vec{H} - \epsilon_0 \frac{\partial^3 \vec{E}}{\partial t^3}. \end{aligned} \tag{2-12}$$

The second time derivative of the curl of the magnetic field in Eq. 2-12 can be related to the electric field by performing a time derivative of Eq. 2-10:

$$\frac{\partial^2}{\partial t^2} \nabla \times \vec{H} = -\frac{1}{\mu_0} \frac{\partial}{\partial t} \nabla \times \nabla \times \vec{E}. \tag{2-13}$$

It is noted that the time derivatives in Eq. 2-13 can be moved inside or outside of the curl operators because the temporal and spatial derivatives are independent of each other. By substitution of Eq. 2-10 and Eq. 2-13 into Eq. 2-12, the explicit relationships between the plasma current density and the electric field are then:

$$\begin{aligned}\frac{\partial \vec{J}}{\partial t} &= -\frac{1}{\mu_0}\nabla \times \nabla \times \vec{E} - \epsilon_0 \frac{\partial^2 \vec{E}}{\partial t^2} \\ \frac{\partial^2 \vec{J}}{\partial t^2} &= -\frac{1}{\mu_0}\frac{\partial}{\partial t}\nabla \times \nabla \times \vec{E} - \epsilon_0 \frac{\partial^3 \vec{E}}{\partial t^3}.\end{aligned} \tag{2-14}$$

The next step in the derivation of the cold plasma wave equation for the electric field is to take another time derivative of the first-order moment of the Boltzmann Equation (Eq. 2-3):

$$\frac{\partial^2 \vec{J}}{\partial t^2} = \frac{q_e^2 N_e}{m_e}\frac{\partial \vec{E}}{\partial t} + \frac{q_e}{m_e}\left(\frac{\partial \vec{J}}{\partial t} \times \vec{B}_0\right) - \nu \frac{\partial \vec{J}}{\partial t}. \tag{2-15}$$

where it is assumed that the electron density (N_e), collision frequency (ν), and background magnetic field ($\vec{B}_0$) are all constant in time. Substituting for the time derivatives of the plasma current density in Eq. 2-15 using Eq. 2-14 yields:

$$\begin{aligned}-\frac{1}{\mu_0}\frac{\partial}{\partial t}\nabla \times \nabla \times \vec{E} - \epsilon_0 \frac{\partial^3 \vec{E}}{\partial t^3} = \\ \frac{q_e^2 N_e}{m_e}\frac{\partial \vec{E}}{\partial t} + \frac{q_e}{m_e}\left(-\frac{1}{\mu_0}\nabla \times \nabla \times \vec{E} - \epsilon_0 \frac{\partial^2 \vec{E}}{\partial t^2}\right) \times \vec{B}_0 - \nu\left(-\frac{1}{\mu_0}\nabla \times \nabla \times \vec{E} - \epsilon_0 \frac{\partial^2 \vec{E}}{\partial t^2}\right)\end{aligned} \tag{2-16}$$

Equation 2-16 is the cold plasma wave equation for the electric field, but it can be put into a more traditional wave equation form by placing the spatial derivatives on one side and the temporal derivatives on the other for the final version:

$$\begin{aligned}\frac{\partial(\nabla \times \nabla \times \vec{E})}{\partial t} - \frac{q_e}{m_e}(\nabla \times \nabla \times \vec{E}) \times \vec{B}_0 + \nu(\nabla \times \nabla \times \vec{E}) = \\ -\frac{\mu_0 q_e^2 N_e}{m_e}\frac{\partial \vec{E}}{\partial t} + \frac{q_e \mu_0 \epsilon_0}{m_e}\left(\frac{\partial^2 \vec{E}}{\partial t^2} \times \vec{B}_0\right) - \mu_0 \epsilon_0 \nu \frac{\partial^2 \vec{E}}{\partial t^2} - \mu_0 \epsilon_0 \frac{\partial^3 \vec{E}}{\partial t^3}.\end{aligned} \tag{2-17}$$

The double curls on the left hand side of Eq. 2-17 are often substituted using the vector identity $\nabla \times \nabla \times \vec{A} = \nabla(\nabla \cdot \vec{A}) - \nabla^2 \vec{A}$, but it is not necessary to do so, and we do not do so here.

Having derived the equations for the methods, we now proceed to discuss each method in detail.

2.1.1 Method 1

The first method analyzed in this work was originally presented by *Hu and Cummer* [2006] in 2-D cylindrical coordinates and then expanded to 3-D Cartesian coordinates by *Yu and Simpson* [2010]. This method is unique among the methods presented in that it is straight forward to include multiple charged species. To model an electron-only cold plasma, this method couples the modified Maxwell's Equations with the momentum transport equation, shown together in Eq. 2-18. Method 1 uses a matrix inversion to simultaneously solve for the components of the electric field and plasma current density coupled through the cross product with the background magnetic field. The reader is referred to *Yu and Simpson* [2010] for a full description and derivation of this method. To compare to the other methods presented, this method is reduced to an electron-only plasma.

$$\boxed{\begin{aligned} \nabla \times \vec{E} &= -\mu_0 \frac{\partial \vec{H}}{\partial t} \qquad \nabla \cdot \vec{D} = 0 \\ \nabla \times \vec{H} &= \vec{J} + \epsilon_0 \frac{\partial \vec{E}}{\partial t} \qquad \nabla \cdot \vec{H} = 0 \\ \frac{\partial}{\partial t}\vec{J} &= \frac{q_e^2 N_e}{m_e}\vec{E} + \frac{q_e}{m_e}\vec{J} \times \vec{B}_0 - \nu \vec{J} \end{aligned}} \tag{2-18}$$

It is noted that this method collocates in space and time the $\vec{E}$ and $\vec{J}$ field components and requires time differentials of first-order, the same as Eq. 2-3. *Hu and Cummer* [2006] and *Yu and Simpson* [2010] do not explicitly mention the use of the Möbius transformation. It should be clear that implementing these equations using the MT would result in the same set of update equations for the electric field and plasma current density employed by *Hu and Cummer* [2006] and *Yu and Simpson* [2010].

This method is included for comparison because the time rate of change of the plasma current density is a first-order equation and this is the only method presented that uses only first-order differentials. For a nonlinear implementation of an electron only plasma, this method would require a $6x6$ matrix inversion every iteration. The inverted matrix would then be multiplied to two other $6x6$ matrices in order to create the update coefficients. This process is required at every grid cell in which the plasma parameters vary in time. Of course, one could solve the $6x6$ matrix inversion analytically, but this would require a similar number of multiplies every iteration as well, although some speedup is expected.

2.1.2 Method 2

The second method couples the modified Maxwell's Equations with Eq. 2-5 as the ADE. These equations are shown together in Eq. 2-19.

$$\begin{aligned} \nabla \times \vec{E} &= -\mu_0 \frac{\partial \vec{H}}{\partial t} \qquad \nabla \cdot \vec{D} = 0 \\ \nabla \times \vec{H} &= \frac{\partial \vec{D}}{\partial t} \qquad \nabla \cdot \vec{H} = 0 \\ \epsilon_0 \frac{\partial^2 \vec{E}}{\partial t^2} - \epsilon_0 \frac{q_e}{m_e} \left(\frac{\partial \vec{E}}{\partial t} \times \vec{B}_0 \right) + \epsilon_0 \nu \frac{\partial \vec{E}}{\partial t} + \frac{q_e^2 N_e}{m_e} \vec{E} &= \frac{\partial^2 \vec{D}}{\partial t^2} - \frac{q_e}{m_e} \left(\frac{\partial \vec{D}}{\partial t} \times \vec{B}_0 \right) + \nu \frac{\partial \vec{D}}{\partial t} \end{aligned} \tag{2-19}$$

It is noted that, similar to Method 1, each component of the electric field is coupled to each other and to the effective electric flux density due to the cross product with the background magnetic field. In order to discretize Eq. 2-5, a direct substitution for the time differentials using Eqs. 1-8 to 1-10 is performed. This discretization process is derived below and yields the following relationship (Eq. 2-20):

$$\frac{1}{\Delta t^2}\left(\vec{D}^{n+1}-2\vec{D}^{n}+\vec{D}^{n-1}\right)+\frac{\nu}{2\Delta t}\left(\vec{D}^{n+1}-\vec{D}^{n-1}\right)-\left[\frac{q_e}{m_e}\frac{1}{2\Delta t}\left(\vec{D}^{n+1}-\vec{D}^{n-1}\right)\times\vec{B}_0\right]$$
$$=\frac{\epsilon_0}{\Delta t^2}\left(\vec{E}^{n+1}-2\vec{E}^{n}+\vec{E}^{n-1}\right)+\frac{\epsilon_0\nu}{2\Delta t}\left(\vec{E}^{n+1}-\vec{E}^{n-1}\right)-\left[\frac{\epsilon_0 q_e}{m_e}\frac{1}{2\Delta t}\left(\vec{E}^{n+1}-\vec{E}^{n-1}\right)\times\vec{B}_0\right]$$
$$+\frac{q_e^2 N_e}{m_e}\frac{1}{4\Delta t^0}\left(\vec{E}^{n+1}+2\vec{E}^{n}+\vec{E}^{n-1}\right). \tag{2-20}$$

The latest time step of $\vec{E}$ can be solved for in terms of previous time steps of $\vec{E}$ and the current and previous time steps of $\vec{D}$. This can be written in matrix form as the following:

$$A\begin{bmatrix}\vec{E}_x^{n+1}\\ \vec{E}_y^{n+1}\\ \vec{E}_z^{n+1}\end{bmatrix}=B\begin{bmatrix}\vec{E}_x^{n}\\ \vec{E}_y^{n}\\ \vec{E}_z^{n}\end{bmatrix}+C\begin{bmatrix}\vec{E}_x^{n-1}\\ \vec{E}_y^{n-1}\\ \vec{E}_z^{n-1}\end{bmatrix}+F\begin{bmatrix}\vec{D}_x^{n+1}\\ \vec{D}_y^{n+1}\\ \vec{D}_z^{n+1}\end{bmatrix}+G\begin{bmatrix}\vec{D}_x^{n}\\ \vec{D}_y^{n}\\ \vec{D}_z^{n}\end{bmatrix}+H\begin{bmatrix}\vec{D}_x^{n-1}\\ \vec{D}_y^{n-1}\\ \vec{D}_z^{n-1}\end{bmatrix} \tag{2-21}$$

where A, B, C, F, G, and H are 3x3 coefficient matrices and are provided in the Appendix. In order to solve for the latest time step of $\vec{E}$, Eq. 2-21 is multiplied through by A^{-1}, yielding Eq. 2-22. The inverse of matrix 'A' can be calculated either numerically or analytically.

$$\begin{bmatrix}\vec{E}_x^{n+1}\\ \vec{E}_y^{n+1}\\ \vec{E}_z^{n+1}\end{bmatrix}=A^{-1}B\begin{bmatrix}\vec{E}_x^{n}\\ \vec{E}_y^{n}\\ \vec{E}_z^{n}\end{bmatrix}+A^{-1}C\begin{bmatrix}\vec{E}_x^{n-1}\\ \vec{E}_y^{n-1}\\ \vec{E}_z^{n-1}\end{bmatrix}+A^{-1}F\begin{bmatrix}\vec{D}_x^{n+1}\\ \vec{D}_y^{n+1}\\ \vec{D}_z^{n+1}\end{bmatrix}+A^{-1}G\begin{bmatrix}\vec{D}_x^{n}\\ \vec{D}_y^{n}\\ \vec{D}_z^{n}\end{bmatrix}+A^{-1}H\begin{bmatrix}\vec{D}_x^{n-1}\\ \vec{D}_y^{n-1}\\ \vec{D}_z^{n-1}\end{bmatrix} \tag{2-22}$$

In a linear implementation, the update coefficients do not change with each iteration and the inversion of matrix A only needs to be computed once during the code initialization, as is the case for, $A^{-1}B$, $A^{-1}C$, $A^{-1}F$, $A^{-1}G$, and $A^{-1}H$. Computing the coefficient matrices initially and not in each update iteration significantly reduces the computational burden of this method. For a nonlinear implementation, the update coefficients have to be recalculated every iteration at every grid cell. To do this, A^{-1} is calculated, which is a $3x3$ matrix inversion, and is multiplied through to the five other $3x3$ coefficient matrices. It has been found that

implementing the analytical solution of A^{-1} instead of having MATLAB numerically calculate the $3x3$ matrix inversion every iteration in a nonlinear implementation performs ~6x faster.

2.1.3 Method 2: Non-Möbius Transformation

The implementation of Method 2 without utilizing the Möbius transformation is very similar to the implementation utilizing the Möbius transformation shown above in Section 2.1.2. The same equations shown in Eq. 2-19 are the foundation for this method as well. The Möbius transformation was utilized above through the substitution of the time differentials of Eqs. 1-8 to 1-10 as shown in Eq. 2-20. For the non-Möbius transformation version of Method 2, the second-order (Eq. 1-8) and first-order (Eq. 1-9) time differentials are the same as for the Möbius implementation. The zeroth-order time differential is not the same though, and Eq. 1-10 is not used. Instead the time-centered value is used as shown in Eq. 2-23.

$$\frac{\partial^0 f^n}{\partial t^0} = f^n \tag{2-23}$$

The discretization of Eq. 2-5 in the non-Möbius transformation version of Method 2 uses Eqs. 1-8, 1-9, and 2-23 and is shown in Eq. 2-24.

$$\begin{aligned}
&\frac{1}{\Delta t^2}\left(\vec{D}^{n+1} - 2\vec{D}^{n} + \vec{D}^{n-1}\right) + \frac{\nu}{2\Delta t}\left(\vec{D}^{n+1} - \vec{D}^{n-1}\right) - \left[\frac{q_e}{m_e}\frac{1}{2\Delta t}\left(\vec{D}^{n+1} - \vec{D}^{n-1}\right) \times \vec{B}_0\right] \\
&= \frac{\epsilon_0}{\Delta t^2}\left(\vec{E}^{n+1} - 2\vec{E}^{n} + \vec{E}^{n-1}\right) + \frac{\epsilon_0 \nu}{2\Delta t}\left(\vec{E}^{n+1} - \vec{E}^{n-1}\right) - \left[\frac{\epsilon_0 q_e}{m_e}\frac{1}{2\Delta t}\left(\vec{E}^{n+1} - \vec{E}^{n-1}\right) \times \vec{B}_0\right] \\
&\qquad + \frac{q_e^2 N_e}{m_e}\vec{E}^{n}
\end{aligned} \tag{2-24}$$

Only the zeroth-order time differential term (last term on the right hand side) in Eq. 2-24 is different from Eq. 2-20. The process to isolate and solve for the latest time step of the electric field is the same in the non-Möbius transformation version of Method 2 as above. The final difference is that the update coefficients A, B, and C will be different along the diagonal.

2.1.4 Method 3

The third method analyzed in this work was presented in detail by *Gamliel* [2017]. The form of the update equation for the electric field is similar to that for Method 2 with the major difference being that Method 2 requires differentials of second-order and Method 3 requires differentials of fourth-order. This means that Method 3 requires more time steps and update coefficients in the update equation. This method couples the modified Maxwell's Equations with Eq. 2-7 as the ADE, shown together in Eq. 2-25. In this form, Eq. 2-7 solves for $\vec{D}$ which is already known through the update equation using Ampere's Law. The manipulation of Eq. 2-7 to solve for the latest time step of $\vec{E}$ is described next.

$$\nabla \times \vec{E} = -\mu_0 \frac{\partial \vec{H}}{\partial t} \qquad \nabla \cdot \vec{D} = 0$$

$$\nabla \times \vec{H} = \frac{\partial \vec{D}}{\partial t} \qquad \nabla \cdot \vec{H} = 0$$

$$\vec{D} = \bar{\bar{\epsilon}}_{\text{eff}} \vec{E}$$

$$\bar{\bar{\epsilon}}_{\text{eff}} = \epsilon_0 \bar{\bar{I}} + \frac{\epsilon_0 \omega_p^2}{\omega(\omega - j\nu)\left[(\omega - j\nu)^2 - \omega_c^2\right]} \begin{bmatrix} \omega_{cx}^2 - (\omega - j\nu)^2 & \omega_{cx}\omega_{cy} - (\nu + j\omega)\omega_{cz} & \omega_{cx}\omega_{cz} + (\nu + j\omega)\omega_{cy} \\ \omega_{cx}\omega_{cy} + (\nu + j\omega)\omega_{cz} & \omega_{cy}^2 - (\omega - j\nu)^2 & \omega_{cy}\omega_{cz} - (\nu + j\omega)\omega_{cx} \\ \omega_{cx}\omega_{cz} - (\nu + j\omega)\omega_{cy} & \omega_{cy}\omega_{cz} + (\nu + j\omega)\omega_{cx} & \omega_{cz}^2 - (\omega - j\nu)^2 \end{bmatrix} \tag{2-25}$$

This expression for $\bar{\bar{\epsilon}}_{\text{eff}}$ has powers of $j\omega$ in the denominator. Any $j\omega$ in the denominator corresponds to an integration so the first step is to multiply Eq. 2-7 by the denominator of Eq. 2-8. This is equal to multiplying by $\omega(\omega - j\nu)\left[(\omega - j\nu)^2 - \omega_c^2\right]$. The next step is to expand this relationship in term of $j\omega$. This is shown in Eq. 2-26 for D_x.

$$\begin{aligned} \left[(j\omega)^4 + (j\omega)^3 3\nu + (j\omega)^2(\omega_c^2 + 3\nu^2) + (j\omega)^1(\nu^3 + \nu\omega_c^2)\right] D_x = \\ \epsilon_0 \left[(j\omega)^4 + (j\omega)^3 3\nu + (j\omega)^2(\omega_c^2 + \omega_p^2 + 3\nu^2) + \right. \\ \left. (j\omega)^1(\nu^3 + \nu\omega_c^2 + 2\nu\omega_p^2) + (j\omega)^0(\nu^2\omega_p^2 + \omega_{cx}^2\omega_p^2)\right] E_x + \\ \epsilon_0 \left[-(j\omega)^1\omega_p^2\omega_{cx} + (j\omega)^0(\omega_{cx}\omega_{cy} - \nu\omega_{cz}\right] E_y + \\ \epsilon_0 \left[(j\omega)^1\omega_p^2\omega_{cy} + (j\omega)^0(\omega_{cx}\omega_{cz} + \nu\omega_{cy}\right] E_z \end{aligned} \tag{2-26}$$

An inverse Fourier transform is then performed to arrive back in the time domain shown in Eq. 2-27. This equation is now a fourth-order ordinary differential equation relating D_x to E_x, E_y and E_z. Similar equations can be constructed that relate D_y and D_z to E_x, E_y and E_z. Because the update equations requires fourth-order differentials, Eqs. 1-11 to 1-15 are used to discretize the system.

$$\begin{aligned}\left[\frac{\partial^4}{\partial t^4}+3\nu\frac{\partial^3}{\partial t^3}+(\omega_c^2+3\nu^2)\frac{\partial^2}{\partial t^2}+(\nu^3+\nu\omega_c^2)\frac{\partial^1}{\partial t^1}\right]D_x=\\ \epsilon_0\left[\frac{\partial^4}{\partial t^4}+3\nu\frac{\partial^3}{\partial t^3}+(\omega_c^2+\omega_p^2+3\nu^2)\frac{\partial^2}{\partial t^2}+\right.\\ \left.(\nu^3+\nu\omega_c^2+2\nu\omega_p^2)\frac{\partial^1}{\partial t^1}+(\nu^2\omega_p^2+\omega_{cx}^2\omega_p^2)\frac{\partial^0}{\partial t^0}\right]E_x+\\ \epsilon_0\left[-\omega_p^2\omega_{cx}\frac{\partial^1}{\partial t^1}+(\omega_{cx}\omega_{cy}-\nu\omega_{cz})\frac{\partial^0}{\partial t^0}\right]E_y+\\ \epsilon_0\left[\omega_p^2\omega_{cy}\frac{\partial^1}{\partial t^1}+(\omega_{cx}\omega_{cz}+\nu\omega_{cy})\frac{\partial^0}{\partial t^0}\right]E_z\end{aligned} \tag{2-27}$$

Similar to Method 2 above, the latest time step of $\vec{E}$ is now solved for in terms of previous time steps of $\vec{E}$ and the current and past time steps of $\vec{D}$. The result is expressed:

$$\begin{aligned}[K]\vec{E}^{n+1}=[L]\vec{E}^n+[M]\vec{E}^{n-1}+[N]\vec{E}^{n-2}+[P]\vec{E}^{n-3}\\ +q\vec{D}^{n+1}+r\vec{D}^n+s\vec{D}^{n-1}+t\vec{D}^{n-2}+u\vec{D}^{n-3}\end{aligned} \tag{2-28}$$

where K, L, M, N and P are 3x3 matrices and q, r, s, t and u are scalars, all of which are provided in the Appendix. Again, similar to Method 2, in order to solve for the latest time step of $\vec{E}$, the inverse of matrix K is calculated numerically and Eq. 2-28 is multiplied through by $[K]^{-1}$ resulting in an update for $\vec{E}^{n+1}$ as shown below:

$$\begin{aligned}\vec{E}^{n+1}=[K]^{-1}[L]\vec{E}^n+[K]^{-1}[M]\vec{E}^{n-1}+[K]^{-1}[N]\vec{E}^{n-2}+[K]^{-1}[P]\vec{E}^{n-3}\\ +q[K]^{-1}\vec{D}^{n+1}+r[K]^{-1}\vec{D}^n+s[K]^{-1}\vec{D}^{n-1}+t[K]^{-1}\vec{D}^{n-2}+u[K]^{-1}\vec{D}^{n-3}.\end{aligned} \tag{2-29}$$

In order to efficiently implement Eq. 2-29 for a linear plasma, $[K]^{-1}$ should be calculated only once and used to multiply and create new 3x3 matrices for $[K]^{-1}[L]$, $[K]^{-1}[M]$, $[K]^{-1}[N]$, $[K]^{-1}[P]$, $q[K]^{-1}$, $r[K]^{-1}$, $s[K]^{-1}$, $t[K]^{-1}$ and $u[K]^{-1}$. Because these update coefficients do not change each iteration, they can be computed once at the beginning. For a nonlinear plasma, the update coefficients have to be recalculated. This would require $[K]^{-1}$, a $3x3$ matrix inversion, to be calculated and multiplied through to create the new nine $3x3$ coefficient matrices at every grid cell every iteration. Analytically solving and implementing $[K]^{-1}$ is expected to provide a similar speedup to that seen for Method 2.

2.1.5 Method 4

The fourth method this work considers is similar to Method 3 and couples the modified Maxwell's Equations with Eq. 2-9 as the ADE shown together in Eq. 2-30. Method 4 differs from Method 3 in the way that it solves for each component of $\vec{E}$. This also causes the maximum differential order to be different as well. For Method 4, to solve for the coupled components of $\vec{E}$ individually, the effective permittivity tensor is inverted (Eq. 2-9).

$$\nabla \times \vec{E} = -\mu_0 \frac{\partial \vec{H}}{\partial t} \qquad \nabla \cdot \vec{D} = 0$$
$$\nabla \times \vec{H} = \frac{\partial \vec{D}}{\partial t} \qquad \nabla \cdot \vec{H} = 0$$
$$\vec{E} = \bar{\bar{\epsilon}}_{\text{eff}}^{-1} \vec{D}$$
$$\bar{\bar{\epsilon}}_{\text{eff}} = \epsilon_0 \bar{\bar{I}} + \frac{\epsilon_0 \omega_p^2}{\omega(\omega - j\nu)\left[(\omega - j\nu)^2 - \omega_c^2\right]} \begin{bmatrix} \omega_{cx}^2 - (\omega - j\nu)^2 & \omega_{cx}\omega_{cy} - (\nu + j\omega)\omega_{cz} & \omega_{cx}\omega_{cz} + (\nu + j\omega)\omega_{cy} \\ \omega_{cx}\omega_{cy} + (\nu + j\omega)\omega_{cz} & \omega_{cy}^2 - (\omega - j\nu)^2 & \omega_{cy}\omega_{cz} - (\nu + j\omega)\omega_{cx} \\ \omega_{cx}\omega_{cz} - (\nu + j\omega)\omega_{cy} & \omega_{cy}\omega_{cz} + (\nu + j\omega)\omega_{cx} & \omega_{cz}^2 - (\omega - j\nu)^2 \end{bmatrix} \tag{2-30}$$

This method is valid for an arbitrarily directed background magnetic field and results in an update equation with twelfth-order differentials. It is presented here for a background magnetic field, $\vec{B}_0$, in the $\hat{z}$-direction which decreases the update equation to a sixth-order differential for ease of presentation. With this assumption, the inverse of the effective permittivity matrix can be expressed as:

$$\bar{\bar{\epsilon}}_{\text{eff}}^{-1} = \frac{1}{\epsilon_0}\begin{bmatrix} \frac{A}{D_1} & -\frac{B}{D_1} & 0 \\ \frac{B}{D_1} & \frac{A}{D_1} & 0 \\ 0 & 0 & \frac{C}{D_2} \end{bmatrix} \tag{2-31}$$

where:

$$\begin{aligned} A = (j\omega)^6 + (j\omega)^5(4\nu) + (j\omega)^4(\omega_p^2 + 2\omega_c^2 + 6\nu^2) + (j\omega)^3(3\omega_p^2\nu + 4\omega_c^2\nu + 4\nu^3) \\ +(j\omega)^2(\omega_p^2\omega_c^2 + 3\omega_p^2\nu^2 + \omega_c^4 + 2\omega_c^2\nu^2 + \nu^4) + (j\omega)^1(\omega_p^2\omega_c^2\nu + \omega_p^2\nu^3) \end{aligned} \tag{2-32}$$

$$B = (j\omega)^3(\omega_p^2\omega_c) + (j\omega)^2(2\omega_p^2\omega_c\nu) + (j\omega)^1(\omega_p^2\omega_c^3 + \omega_p^2\omega_c\nu^2) \tag{2-33}$$

$$\begin{aligned} D_1 = (j\omega)^6 + (j\omega)^5(4\nu) + (j\omega)^4(2\omega_p^2 + 2\omega_c^2 + 6\nu^2) + (j\omega)^3(6\omega_p^2\nu + 4\omega_c^2\nu + 4\nu^3) \\ +(j\omega)^2(2\omega_p^2\omega_c^2 + 6\omega_p^2\nu^2 + \omega_c^4 + 2\omega_c^2\nu^2 + \nu^4) + (j\omega)^1(2\omega_p^2\omega_c^2\nu + 2\omega_p^2\nu^3 + 2\omega_p^4\nu) \\ +(j\omega)^0(\omega_p^4\nu^2 + \omega_p^4\omega_c^2) \end{aligned} \tag{2-34}$$

$$C = (j\omega)^2 + (j\omega)^1\nu \tag{2-35}$$

$$D_2 = (j\omega)^2 + (j\omega)^1\nu + (j\omega)^0\omega_p^2. \tag{2-36}$$

Expanding Eq. 2-9 using Eq. 2-31 yields:

$$\epsilon_0 D_1 E_x = AD_x - BD_y \tag{2-37}$$

$$\epsilon_0 D_1 E_y = BD_x + AD_y \tag{2-38}$$

$$\epsilon_0 D_2 E_z = CD_z. \tag{2-39}$$

It is noted that the coupling of E_x with D_y in Eq. 2-37 and similarly E_y with D_x in Eq. 2-38 is not an issue because the latest time step of all components of $\vec{D}$ are already known and are available to be used.

Now the frequency-domain expression for $\bar{\bar{\epsilon}}_{\text{eff}}^{-1}$ is converted back to the time domain and A, B, C, D_1 and D_2 become differential operators:

$$A = \partial_t^6 + \partial_t^5(4\nu) + \partial_t^4(\omega_p^2 + 2\omega_c^2 + 6\nu^2) + \partial_t^3(3\omega_p^2\nu + 4\omega_c^2\nu + 4\nu^3) \\ +\partial_t^2(\omega_p^2\omega_c^2 + 3\omega_p^2\nu^2 + \omega_c^4 + 2\omega_c^2\nu^2 + \nu^4) + \partial_t^1(\omega_p^2\omega_c^2\nu + \omega_p^2\nu^3) \tag{2-40}$$

$$B = \partial_t^3(\omega_p^2\omega_c) + \partial_t^2(2\omega_p^2\omega_c\nu) + \partial_t^1(\omega_p^2\omega_c^3 + \omega_p^2\omega_c\nu^2) \tag{2-41}$$

$$D_1 = \partial_t^6 + \partial_t^5(4\nu) + \partial_t^4(2\omega_p^2 + 2\omega_c^2 + 6\nu^2) + \partial_t^3(6\omega_p^2\nu + 4\omega_c^2\nu + 4\nu^3) \\ +\partial_t^2(2\omega_p^2\omega_c^2 + 6\omega_p^2\nu^2 + \omega_c^4 + 2\omega_c^2\nu^2 + \nu^4) + \partial_t^1(2\omega_p^2\omega_c^2\nu + 2\omega_p^2\nu^3 + 2\omega_p^4\nu) \\ +\partial_t^0(\omega_p^4\nu^2 + \omega_p^4\omega_c^2) \tag{2-42}$$

$$C = \partial_t^2 + \partial_t^1\nu \tag{2-43}$$

$$D_2 = \partial_t^2 + \partial_t^1\nu + \partial_t^0\omega_p^2 \tag{2-44}$$

where $\partial_t = \frac{\partial}{\partial t}$. It is clear from Eqs. 2-37 to 2-39 that E_x, E_y, D_x and D_y are independent from E_z and D_z when $\vec{B}_0$ is directed in the $\hat{z}$-direction. Additionally, it is clear from Eqs. 2-40 to 2-44 that equations for E_x and E_y are sixth-order differential equations where the equation for E_z is only a second-order differential equation. As a result, the equations for E_x and E_y will be handled differently from the equation for E_z. For E_z, Eqs. 1-8 to 1-10 are used and for E_x and E_y, the sixth-order differentials as given by the Möbius transformation are used. For an arbitrarily directed $\vec{B}$-field, all of the update equations are 12^{th}-order.

In order to solve for the latest time step of $\vec{E}$, Eqs. 1-8 to 1-10 and the sixth-order differentials as given by the Möbius transformation are substituted into Eqs. 2-40 to 2-44. A, B, C, D_1, and D_2 are then used in Eqs. 2-37 to 2-39 and E_x^{n+1}, E_y^{n+1}, and E_z^{n+1} are solved for. This yields a set of equations in the form of:

$$
\begin{aligned}
E_x\Big|_k^{n+1} &= k_{E2}E_x\Big|_k^{n} + k_{E3}E_x\Big|_k^{n-1} + k_{E4}E_x\Big|_k^{n-2} \\
&+ k_{E5}E_x\Big|_k^{n-3} + k_{E6}E_x\Big|_k^{n-4} + k_{E7}E_x\Big|_k^{n-5} \\
&+ k_{Dx1}D_x\Big|_k^{n+1} + k_{Dx2}D_x\Big|_k^{n} + k_{Dx3}D_x\Big|_k^{n-1} + k_{Dx4}D_x\Big|_k^{n-2} \\
&+ k_{Dx5}D_x\Big|_k^{n-3} + k_{Dx6}D_x\Big|_k^{n-4} + k_{Dx7}D_x\Big|_k^{n-5} \\
&+ k_{Dy1}D_y\Big|_k^{n+1} + k_{Dy2}D_y\Big|_k^{n} + k_{Dy3}D_y\Big|_k^{n-1} + k_{Dy4}D_y\Big|_k^{n-2} \\
&+ k_{Dy5}D_y\Big|_k^{n-3} + k_{Dy6}D_y\Big|_k^{n-4} + k_{Dy7}D_y\Big|_k^{n-5}
\end{aligned}
\tag{2-45}
$$

where the constants in the above equation are easily derived when solving for the latest time step of $\vec{E}$. Similar to Eq. 2-45, update equations for E_y and E_z can be written out. In a nonlinear implementation, the effective permittivity tensor will change every iteration at each grid cell. The inversion of the effective permittivity tensor and subsequent derivation of the update coefficients would need to be recalculated.

2.1.6 Method 5

The fifth method presented and compared in this work is a direct discretization of the cold plasma wave equation for the electric field as shown in Eq. 2-46. A unique feature of using the wave equation is that there is no leap-frogging in time or space between $\vec{E}$ and $\vec{H}$ which is common and standard in most FDTD schemes. There are no field values of the magnetic field, plasma current density, or effective electric flux density utilized in this method. Instead, the electric field is updated wholly from previous iterations of itself.

$$
\boxed{
\begin{aligned}
&\frac{\partial(\nabla\times\nabla\times\vec{E})}{\partial t} - \frac{q_e}{m_e}(\nabla\times\nabla\times\vec{E})\times\vec{B}_0 + \nu(\nabla\times\nabla\times\vec{E}) = \\
&-\frac{\mu_0 q_e^2 N_e}{m_e}\frac{\partial\vec{E}}{\partial t} + \frac{q_e\mu_0\epsilon_0}{m_e}\left(\frac{\partial^2\vec{E}}{\partial t^2}\times\vec{B}_0\right) - \mu_0\epsilon_0\nu\frac{\partial^2\vec{E}}{\partial t^2} - \mu_0\epsilon_0\frac{\partial^3\vec{E}}{\partial t^3}
\end{aligned}
}
\tag{2-46}
$$

The wave equation can be discretized in 3-D for an arbitrary directed background magnetic field and requires time differentials of third-order. As an example shown in Eq. 2-47, the E_x component of the wave equation has been discretized assuming 1-D propagation and

background magnetic field alignment in the $\hat{z}$ direction. A similar equation can be derived for the E_y component. Under these propagation assumptions with a source in the x-y plane, E_x and E_y are independent of E_z and update equations for only E_x and E_y are required. $\vec{H}$, $\vec{J}$, and $\vec{D}$ can be calculated directly from $\vec{E}$ during the simulation or after the simulation is complete.

$$
\begin{aligned}
&-\frac{1}{(\Delta z)^2}\left(\frac{1}{\Delta t}\left[(E_x^{z+1})^{n+1/2}-(E_x^{z+1})^{n-1/2}\right]-\right.\\
&\left.\frac{2}{\Delta t}\left[(E_x^{z})^{n+1/2}-(E_x^{z})^{n-1/2}\right]+\frac{1}{\Delta t}\left[(E_x^{z-1})^{n+1/2}-(E_x^{z-1})^{n-1/2}\right]\right)\\
&+\frac{q_e B_{0z}}{m_e(\Delta z)^2}\left(\frac{1}{2}\left[(E_y^{z+1})^{n+1/2}-(E_y^{z+1})^{n-1/2}\right]-\right.\\
&\left.\frac{2}{2}\left[(E_y^{z})^{n+1/2}-(E_y^{z})^{n-1/2}\right]+\frac{1}{2}\left[(E_y^{z-1})^{n+1/2}-(E_y^{z-1})^{n-1/2}\right]\right)\\
&-\frac{\nu}{(\Delta z)^2}\left(\frac{1}{2}\left[(E_x^{z+1})^{n+1/2}-(E_x^{z+1})^{n-1/2}\right]-\right.\\
&\left.\frac{2}{2}\left[(E_x^{z})^{n+1/2}-(E_x^{z})^{n-1/2}\right]+\frac{1}{2}\left[(E_x^{z-1})^{n+1/2}-(E_x^{z-1})^{n-1/2}\right]\right)\\
&=-\frac{\mu_0 q_e^2 N_e}{m_e}\frac{1}{4\Delta t^1}\left((E_x^{z})^{n+3/2}+(E_x^{z})^{n+1/2}-(E_x^{z})^{n-1/2}-(E_x^{z})^{n-3/2}\right)\\
&+\frac{q_e\mu_0\epsilon_0}{m_e}\frac{B_{0z}}{2\Delta t^2}\left((E_y^{z})^{n+3/2}-(E_y^{z})^{n+1/2}-(E_y^{z})^{n-1/2}+(E_y^{z})^{n-3/2}\right)\\
&-\mu_0\epsilon_0\nu\frac{1}{2\Delta t^2}\left((E_x^{z})^{n+3/2}-(E_x^{z})^{n+1/2}-(E_x^{z})^{n-1/2}+(E_x^{z})^{n-3/2}\right)\\
&-\mu_0\epsilon_0\frac{1}{\Delta t^3}\left((E_x^{z})^{n+3/2}-3(E_x^{z})^{n+1/2}+3(E_x^{z})^{n-1/2}-(E_x^{z})^{n-3/2}\right)
\end{aligned}
\tag{2-47}
$$

There are a few things to note about the discretization of this update equation. The double curls on the left hand side of Eq. 2-46 cause the electric field update equation to include electric field terms spatially surrounding the intended update term. This can be seen by the inclusion of the E_x^{z+1} and E_x^{z-1} terms in Eq. 2-47. Second, the spatially surrounding terms are only differenced or averaged over the $E^{n+1/2}$ and $E^{n-1/2}$ time steps because they are already the averaged values and do not require the additional terms brought on due to the higher order differentials on the right hand side of Eq. 2-46. If the spatially surrounding terms were averaged over the four time steps, including the latest time step, $E^{n+3/2}$, then the update

equation for a singular point would be coupled with the update equations of the surrounding points. This would require solving for the electric field update of the entire gird simultaneously. Third, the cross product of $\vec{E}$ and $\vec{B}_0$ on the right hand side of Eq. 2-46 couples the update equations for the different directional components, E_x and E_y. This is similar to what occurs for the four above methods.

In order to update the electric field, $(E_x^z)^{n+3/2}$ in Eq. 2-47 and $(E_y^z)^{n+3/2}$ in the $\hat{y}$-component equation (not shown) are solved for. The two equations are then combined into matrix form as shown in Eq. 2-48. Similar to the methods above, the inverse of matrix A is solved for and multiplied through Eq. 2-48. The 2x2 update coefficient matrices are provided in the Appendix. For a nonlinear implementation, A^{-1} would be calculated and then the update coefficients would need to be recalculated every iteration at each grid cell.

$$\begin{aligned} A\begin{bmatrix}\vec{E}_x^{n+3/2}\\ \vec{E}_y^{n+3/2}\end{bmatrix}^z = B\begin{bmatrix}\vec{E}_x^{n+1/2}\\ \vec{E}_y^{n+1/2}\end{bmatrix}^z + C\begin{bmatrix}\vec{E}_x^{n-1/2}\\ \vec{E}_y^{n-1/2}\end{bmatrix}^z + D\begin{bmatrix}\vec{E}_x^{n-3/2}\\ \vec{E}_y^{n-3/2}\end{bmatrix}^z \\ +F\begin{bmatrix}\vec{E}_x^{n+1/2}\\ \vec{E}_y^{n+1/2}\end{bmatrix}^{z+1} + G\begin{bmatrix}\vec{E}_x^{n-1/2}\\ \vec{E}_y^{n-1/2}\end{bmatrix}^{z+1} + H\begin{bmatrix}\vec{E}_x^{n+1/2}\\ \vec{E}_y^{n+1/2}\end{bmatrix}^{z-1} + I\begin{bmatrix}\vec{E}_x^{n-1/2}\\ \vec{E}_y^{n-1/2}\end{bmatrix}^{z-1} \end{aligned} \tag{2-48}$$

2.2 Demonstration of Methods

Method 2 was chosen to compare against a number of analytical solutions in order to verify that these methods are accurately modeling a cold plasma. Some of the tests presented here are similar to those presented by *Gamliel* [2017] for Method 3 which are considered here to be excellent tests of cold plasma accuracy. All figures are produced from numerical results from a 1-D implementation and unless otherwise stated, the plasma parameters used are: $\omega_p = 2\pi E9$, $\nu = 2E9$ and $\omega_c = 4\pi E9$. Furthermore, the background magnetic field is in the direction of propagation, along the $\hat{z}$-axis.

2.2.1 Möbius: Unit Step and Impulse Response

The first tests are the unit step and impulse response from free-space to a constant, isotropic cold plasma slab shown in Figure 2-1. An ideal impulse is impossible to model so the Dirac Delta function was simulated by turning the source on for only one iteration. The unit

step was simulated in a similar fashion where the source was turned on to its peak value and left on. The analytical ideal response for the unit step and impulse for a plasma slab are taken from *Wait* [1969] and are:

$$\text{Unit Step Response} = [J_2(\omega_p t) + J_0(\omega_p t) - 1]\, u(t) \tag{2-49}$$

$$\text{Impulse Response} = -(2/t) J_2(\omega_p t) u(t) \tag{2-50}$$

where J_n is the Bessel function of first kind of order n and u(t) is the unit step function.

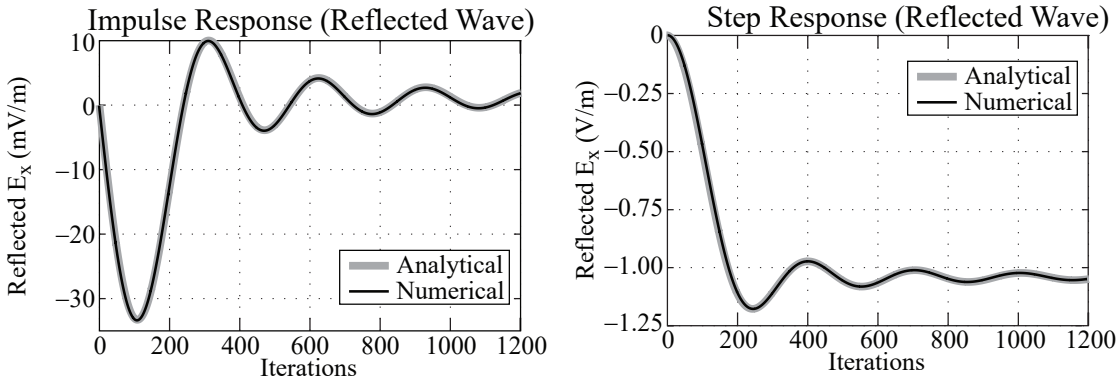

Figure 2-1. (left) Unit impulse response and (right) unit step response

The reflected wave is recorded for the first 1200 iterations which is approximately 4 ns. The calculated error for the reflected wave is 0.4536% for the impulse response and 0.2560% for the unit step response, respectively. The simulated plasma response is plotted on top of the analytical response in Figure 2-1. From the plotted response and the calculated error, it is clear that Method 2 is able to closely reproduce the ideal response for the impulse and unit step.

2.2.2 Möbius: Faraday Rotation

The second test is Faraday rotation in the lossless and lossy case shown in Figure 2-2. In these tests, the cyclotron frequency used is $\omega_c = 1\pi E9$, the collision frequency is $\nu = 4E9$ and the angular frequency of the wave is $\omega = 10\pi E9$. In both cases, a linearly polarized wave in the $\hat{x}$-direction is incident upon a magnetized plasma. In the lossless (no collisions) case, the linear polarization is maintained, but rotates as a function of propagation distance. This is due to the difference in phase propagation constants of the right hand and left hand circularly

polarized waves which can be considered to make up the linearly polarized wave. The angle of rotation as a function of distance is given by *Inan and Inan* [1999] as:

$$\theta_F = \frac{|q_e|^3 N_e B_0}{2m_e^2 \epsilon_0 \omega^2 c} d. \tag{2-51}$$

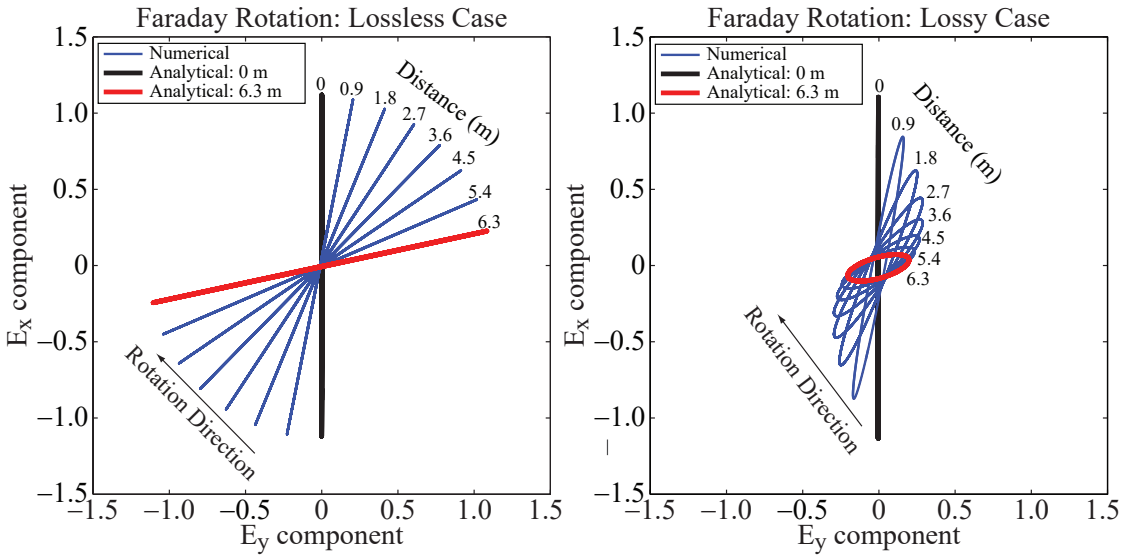

Figure 2-2. (left) Faraday rotation without collisions and (right) with collisions

The the analytical initial and end values plotted for the lossless and lossy cases are plotted in Figure 2-2. Each numerically simulated wave is sampled 15 wavelengths apart or 0.9 meters. The total distance of wave propagation is 6.3 meters which we analytically calculate an angle of rotation of $75.65°$. As can be seen here, when there are no collisions, perfect linear polarization is maintained as a function of distance. When collisions are included, the linear polarization becomes elliptical with a decreasing amplitude due to attenuation. For the lossy case, the percent error of the eccentricity along with the absolute tilt angle error in degrees for the numerical model are shown in Table 2-1. The Faraday rotation accuracy shown here is comparable to that shown in *Gamliel* [2017].

Hunsberger et al. [1992] and *Yu and Simpson* [2010] demonstrated Faraday rotation of a linearly polarized wave in a lossless, magnetized plasma. As was shown in Figure 2-2 for the lossless case, the perfect linear polarization should be maintained as the wave propagates.

Distance (m)	Eccentricity Error (%)	Tilt Angle Error (°)
0	6.71e-5	0
0.9	0.1229	0.30
1.8	0.4813	0.11
2.7	1.0343	0.92
3.6	2.0407	0.72
4.5	2.8011	1.03
5.4	4.5901	1.34
6.3	5.7189	1.65

Table 2-1. Eccentricity percent error and tilt angle absolute error for Method 2 for Faraday rotation with collisions

Instead, *Hunsberger et al.* [1992] and *Yu and Simpson* [2010] incorrectly showed the wave becoming more elliptical as a function of distance. *Gamliel* [2017] incorrectly explained the phenomenon shown in *Yu and Simpson* [2010] as a coupling between the intended linearly polarized source in E_x with J_y and E_y in the plane of the source. If this was the case, then the elliptically polarized plane wave incident on the plasma slab would maintain its eccentricity as a function of distance. Instead, the eccentricity of the wave is changing as a function of distance. An additional unknown loss mechanism (whether numerical or otherwise) in the FDTD implementations of *Hunsberger et al.* [1992] and *Yu and Simpson* [2010] must be present to explain the change of eccentricity of the polarization as a function of distance in the lossless case.

2.2.3 Möbius: Reflection and Transmission Characteristics

The third test is the reflection and transmission coefficients along with propagation constants for four different cold plasmas: 1) isotropic and lossless (Figure 2-3), 2) isotropic and lossy (Figure 2-4), 3) anisotropic and lossless (Figures 2-5, 2-6), and 4) anisotropic and lossy (Figures 2-7, 2-8). When there is a background magnetic field, the reflection, transmission and propagation constant components are separated between the right-hand (RCP) and left-hand (LCP) circular polarization. For normal incidence, which is simulated here, the analytical solution for the reflection coefficient can be calculated as follows:

$$\Gamma = \frac{n_2 - n_1}{n_2 + n_1} \tag{2-52}$$

and for the transmission coefficient:

$$T = \frac{2n_2}{n_2 + n_1}. \tag{2-53}$$

The analytical reflection and transmission magnitude and phase can be calculated from Eq. 2-52 and Eq. 2-53. The analytical solution for the propagation constant is:

$$k = \omega\sqrt{\mu_0\epsilon_0}n \tag{2-54}$$

where:

$$\beta = \text{real}(k) \tag{2-55}$$

$$\alpha = \text{imaginary}(k). \tag{2-56}$$

In the above calculations, $n_i = \sqrt{\epsilon_i}$, where $\epsilon_1 = 1$ and $\epsilon_2 = 1 - \frac{X}{1-jZ\pm Y}$, $X = \frac{\omega_p^2}{\omega^2}$, $Y = \frac{\omega_c}{\omega}$ and $Z = \frac{\nu}{\omega}$.

In Figures 2-3 - 2-8, the numerical results are plotted as circles or squares on top of the analytical calculations shown as continuous lines. Γ and τ are the reflection and transmission coefficient, respectively. The percent error for each test case is shown in Table 2-2. In general, the largest errors exist at sharp frequency transition points which occur mostly at the plasma frequency or the cyclotron frequency. When collisions are included, the plots are 'smoothed' and the accuracy increases, especially around these transition points. This can further be verified by referencing Table 2-2, wherein the error decreases when collisions are included. For example, comparing an electron only plasma and an electron and collisional plasma, it is seen that the reflection magnitude error decreases by approximately a factor of 10 in the collisional case.

Plasma	Reflection Magnitude Error (%)	Transmission Magnitude Error (%)	Propagation Constant Error (%)
$\nu = 0, \vec{B}_0 = 0$	0.4840	0.3719	0.960
$\nu \neq 0, \vec{B}_0 = 0$	0.0525	0.1968	0.9666
$\nu = 0, \vec{B}_0 \neq 0$ RCP	1.3306	0.8349	4.3523
$\nu = 0, \vec{B}_0 \neq 0$ LCP	1.4471	0.0463	1.1208
$\nu \neq 0, \vec{B}_0 \neq 0$ RCP	0.1632	0.4972	1.2659
$\nu \neq 0, \vec{B}_0 \neq 0$ LCP	0.6251	0.0342	1.1191

Table 2-2. Percent error for Method 2 for the four plasma test cases

The first plasma configuration is an electron only plasma shown in Figure 2-3 and the largest deviations of the numerical results from the analytical solution occur at the plasma frequency, 1 GHz. Below this frequency, the wave does not propagate into the plasma as shown by the real part of the propagation constant equaling zero, but above this frequency it does, as signified by the real part of the propagation constant being non-zero. At the plasma frequency, the real part of the propagation constant changes from zero to rapidly increasing positive values. The imaginary part of the propagation constant changes from a large negative value to a constant value of zero. The reflection magnitude starts to decrease from one and the reflection and transmitted angle reach a value of zero degrees. This transition point is difficult to model and for all plots it is seen that the modeled results differ slightly from the analytical values at this frequency. Just 0.1 GHz on either side of the plasma frequency, the model accurately reproduces the analytical results.

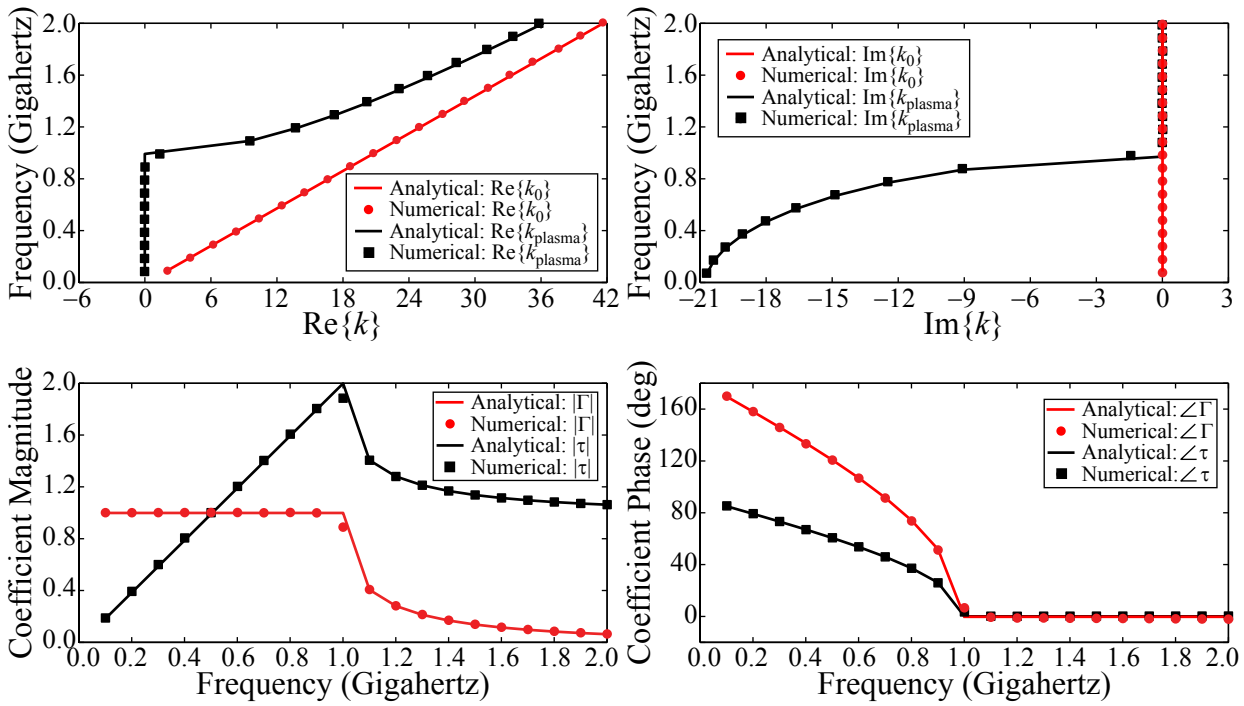

Figure 2-3. Response to an electron only plasma (top left) Real part of the phase constant for free space and plasma, (top right) imaginary part of the phase constant for free space and plasma, (bottom left) reflection and transmission coefficient magnitude, and (bottom right) reflection and transmission coefficient phase

Collisions are included in the second plasma configuration shown in Figure 2-4. All four plots become rounded, and no significant deviation from the analytical solution is observed, even near the plasma frequency. The real part of the propagation constant shows that the wave propagates into the plasma at frequencies below the plasma frequency although the imaginary component indicates that there is large attenuation below the plasma frequency. Both of these parameters are modeled well across the frequency range. The reflection and transmission magnitude show only minor deviations from the analytical result across the frequency range modeled, and specifically at the plasma frequency, 1 GHz. Additionally, the reflection and transmission angle is accurately modeled across the frequency range.

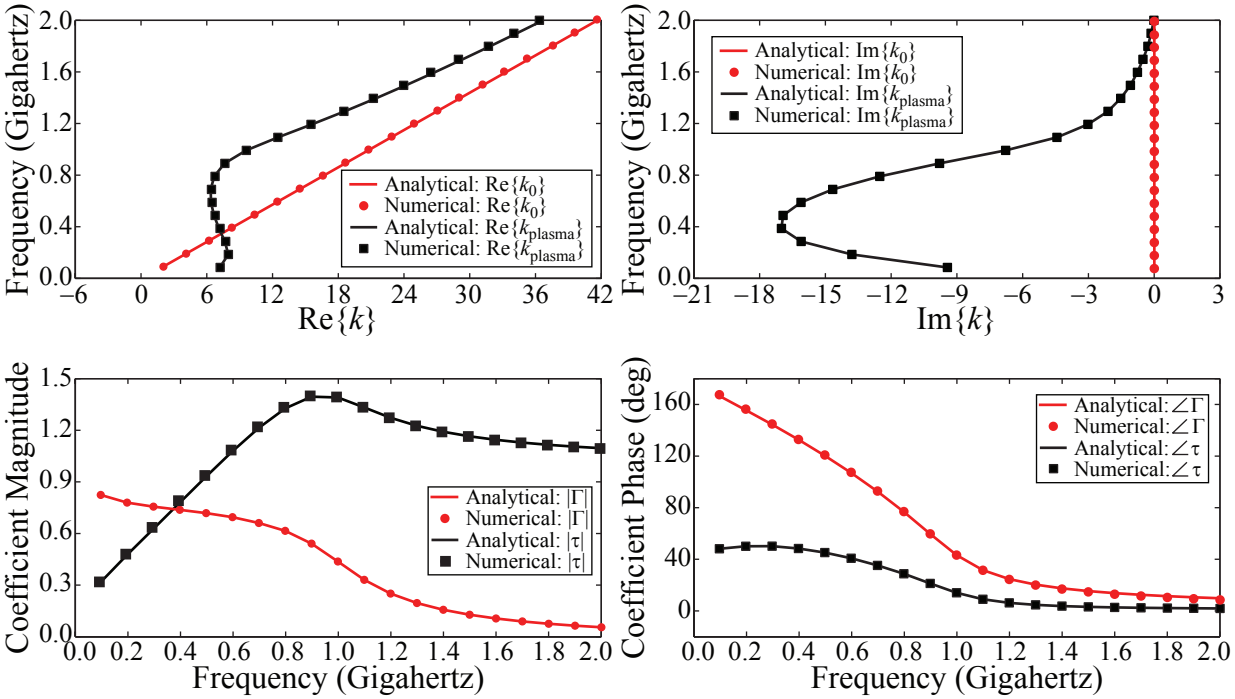

Figure 2-4. Response to an electron plasma with collisions (top left) Real part of the phase constant for free space and plasma, (top right) imaginary part of the phase constant for free space and plasma, (bottom left) reflection and transmission coefficient magnitude, and (bottom right) reflection and transmission coefficient phase

The third plasma configuration includes a static magnetic field, but no collisions, the results for which are shown in Figures 2-5 - 2-6. The LCP component plots closely resemble those of an electron only plasma shown in test case 1. In this case, below approximately half

the plasma frequency, the LCP component does not propagate into the plasma. The reflection and transmission magnitude and phase are all accurately modeled across the frequency range (0.1 to 3 GHz). Additionally, the real and imaginary parts of the propagation constant are modeled accurately. The sharpest transition occurs around 0.5 GHz and it is seen across the four plots that there are no large deviations from the analytical solutions. The model can accurately reproduce the propagation characteristics at frequencies close to resonances.

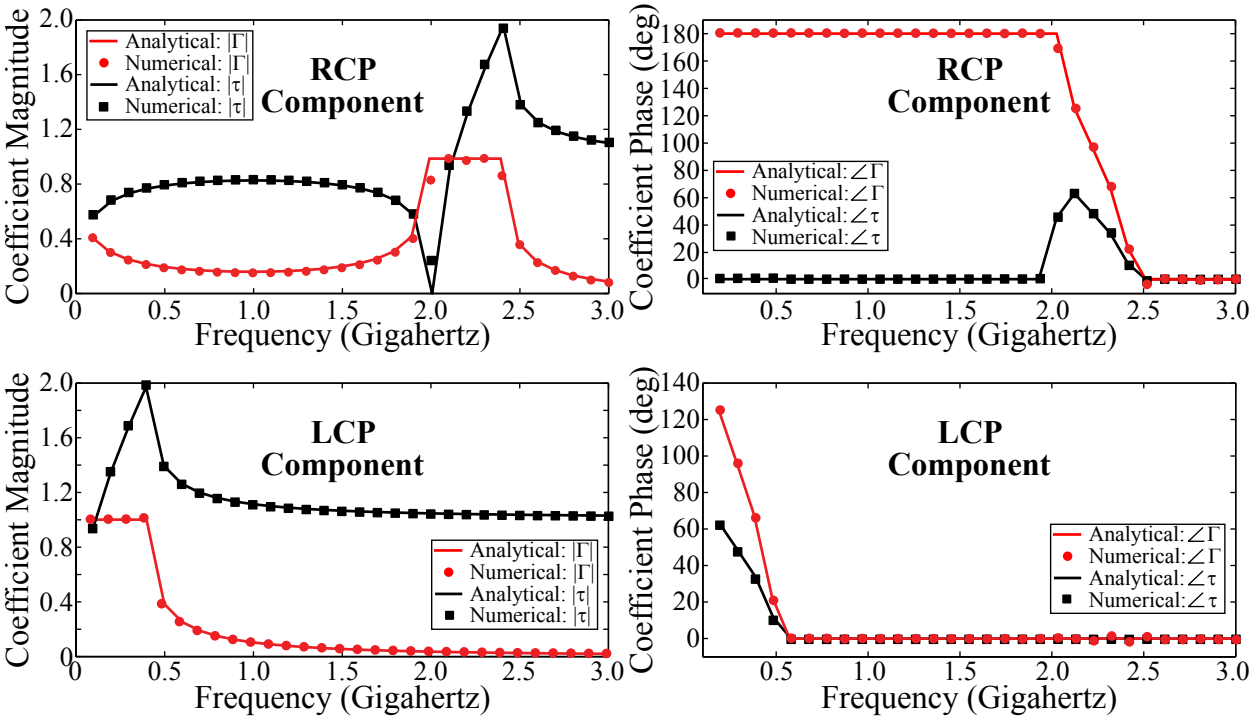

Figure 2-5. Response to an electron plasma with a background magnetic field (top left) RCP component reflection and transmission coefficient magnitude, (top right) RCP component reflection and transmission coefficient phase, (bottom left) LCP component reflection and transmission coefficient magnitude, and (bottom right) LCP component reflection and transmission coefficient phase

The RCP component plots of the third plasma configuration are more complicated than the LCP component and are therefore more difficult to model at a number of frequencies. The RCP component propagates through the plasma at frequencies below the cyclotron frequency, ω_c, and at frequencies above 2.4 GHz. The real part of the propagation constant approaches infinity as ω approaches ω_c from below. Between ω_c and 2.4 GHz, the real part of

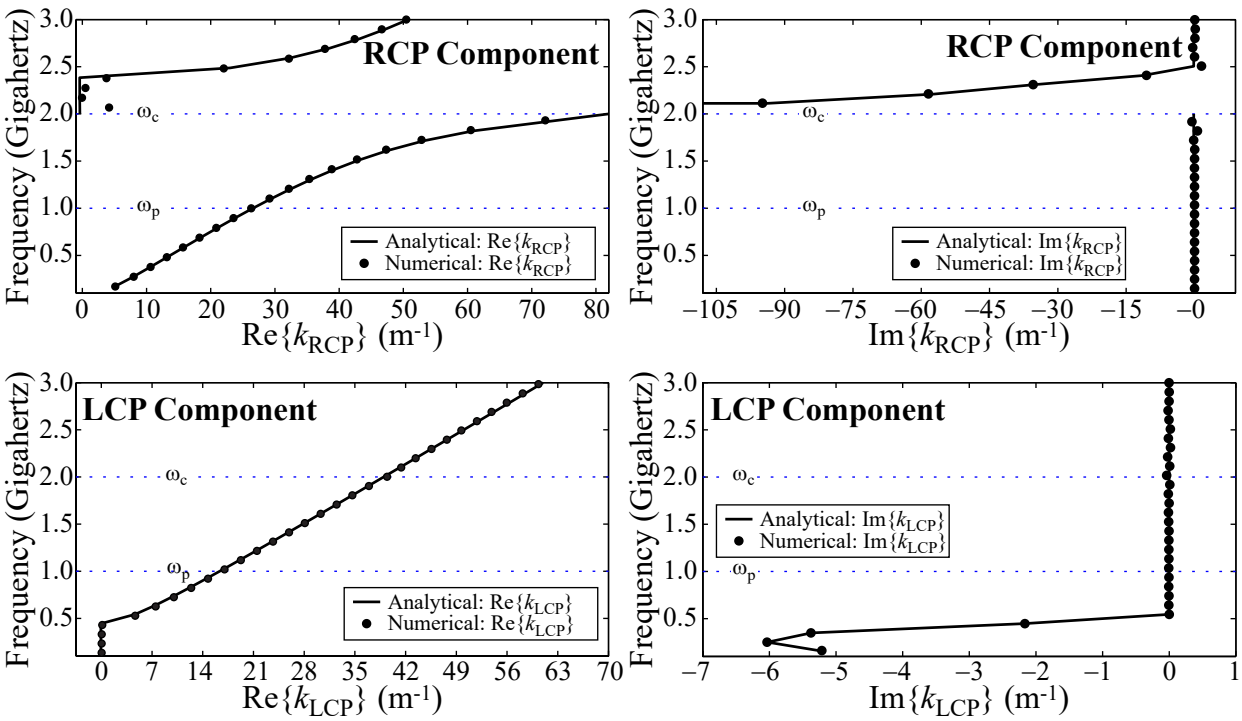

Figure 2-6. Response to an electron plasma with a background magnetic field (top left) RCP component real part of the phase constant, (top right) RCP component imaginary part of the phase constant, (bottom left) LCP component real part of the phase constant, and (bottom right) LCP component imaginary part of the phase constant

the propagation constant is zero, and above 2.4 GHz, it begins to increase again. Conversely, the imaginary part of the propagation constant is zero everywhere besides between ω_c and 2.4 GHz. As ω approaches ω_c from above, the imaginary part of the propagation constant goes to negative infinity. This asymptotic behavior is difficult to reproduce and deviations from the analytical results occur between ω_c and 2.4 GHz for the real part of the propagation constant. The reflection and transmission magnitude and phase likewise experience significant transitions at ω_c and 2.4 GHz. At ω_c, the reflection magnitude should be one and the transmission magnitude zero, although it is seen that these values are not quite achieved. At 2.4 GHz, the transmission magnitude is well modeled, but the reflection magnitude differs slightly from expectations. The reflection and transmission phase is well modeled across the frequency range. The only deviation occurs at ω_c for the reflection phase which is about 10° off from the analytical solution.

The fourth plasma configuration, the results for which are shown in Figures 2-7 - 2-8, includes collisions and a static background magnetic field. as with the second plasma configuration, when collisions are included, all plots are rounded removing any sharp transitions and asymptotic behavior. Comparing with the third plasma configuration for the LCP component, the transitions that occur at ω_{01} are now more gradual and smoother. The reflection and transmission magnitude and phase do not have a discontinuity in slope at ~0.5 GHz. There are no apparent significant deviations in the numerical results from the analytical values for these plots. Similarly, the transition at ~0.5 GHz is more gradual now for both the real and imaginary part of the propagation constant and the modeled results closely follow the analytical values.

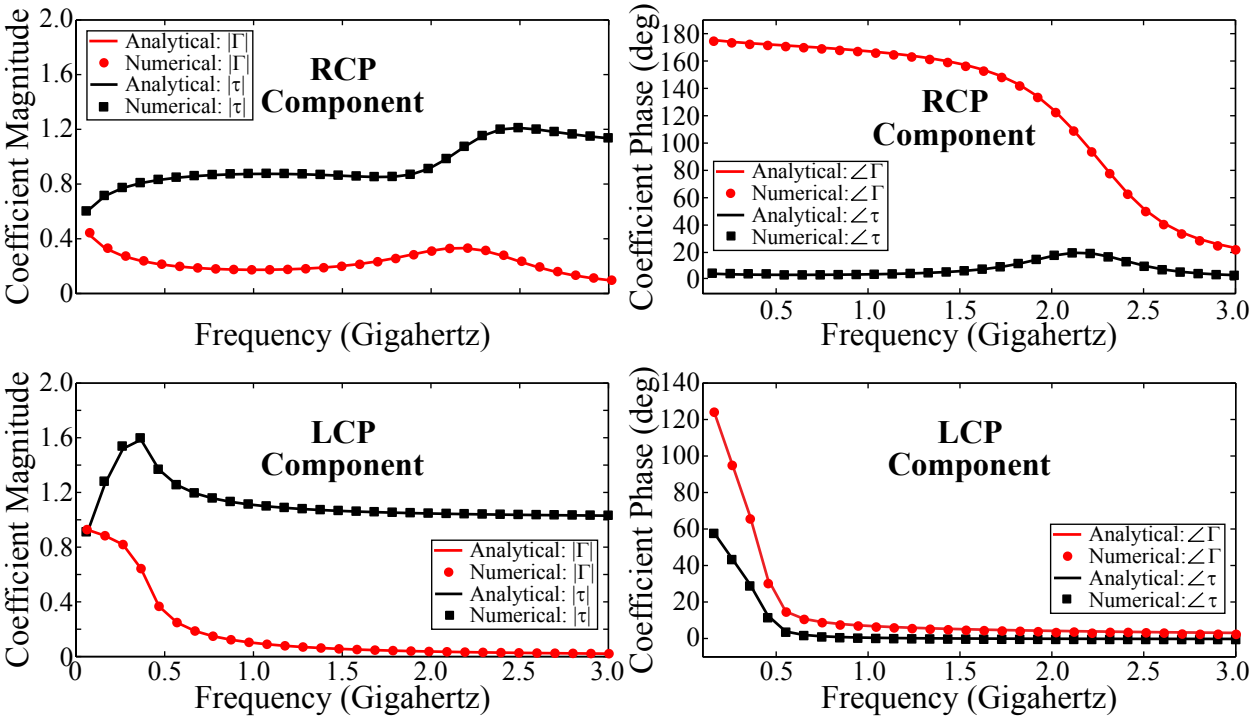

Figure 2-7. Response to an electron plasma with collisions and background magnetic field (top left) RCP component reflection and transmission coefficient magnitude, (top right) RCP component reflection and transmission coefficient phase, (bottom left) LCP component reflection and transmission coefficient magnitude, and (bottom right) LCP component reflection and transmission coefficient phase

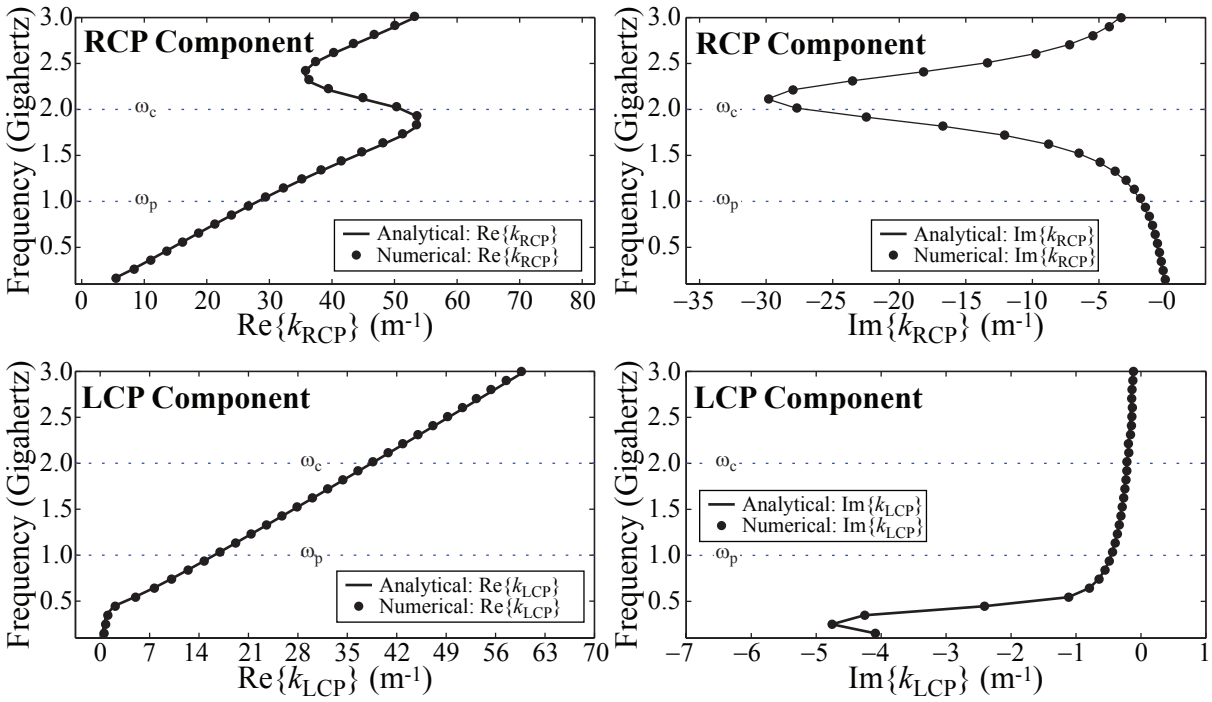

Figure 2-8. Response to an electron plasma with collisions and background magnetic field (top left) RCP component real part of the phase constant, (top right) RCP component imaginary part of the phase constant, (bottom left) LCP component real part of the phase constant, and (bottom right) LCP component imaginary part of the phase constant

The RCP component plots of the fourth plasma configuration are also improved in their accuracy. In the third plasma configuration for the RCP component, significant deviations from the analytical values occurred at ω_c and 2.4 GHz. There are no more discontinuities in slope for the reflected and transmitted magnitude and phase and the modeled results align closely with the analytical values. Additionally, there is no more asymptotic behavior at ω_c in the real and imaginary part of the propagation constant. Across the frequency range, the real and imaginary part of the propagation constant are now more accurately modeled.

Overall, as can be seen from the Figs. 2-3 to 2-6 and Table 2-2, excellent accuracy, similar to that shown in *Hunsberger et al.* [1992] and *Gamliel* [2017] for Method 3, is achieved for all four plasma configurations across the range of frequencies tested. As described above and can be seen in Table 2-2, the error percentage decreases and the accuracy increases for all cases when collisions are included. This is mainly due to a decrease in error that occurs at sharp

transition points such as the asymptotic behavior of the propagation constant for the RCP in test case 3.

2.2.4 Non-Möbius: Reflection and Transmission Characteristics

To highlight the importance of utilizing the Möbius transformation to discretize the update equations, the results from Method 2 discretized with and without using the Möbius transformation are presented in Figure 2-9. In this test, sinusoidal waves at various frequencies around the plasma frequency (1 GHz) and cyclotron frequency (2 GHz) were injected into free space and the reflection and transmission characteristics of a constant, collisional, anisotropic plasma slab were calculated. Shown in the top panels of Figure 2-9 are the right hand circularly polarized (RCP) components and in the bottom panels are the left hand circularly polarized (LCP) components. The left panels show the reflection (Γ) and transmission (τ) magnitudes and the right panels show the reflection and transmission angles. In all panels the solid lines represent the analytical solution, the squares represent the numerical results of Method 2 discretized using the Möbius transformation, and the circles represent the numerical results of Method 2 discretized without using the Möbius transformation.

For the Möbius transformation method, the magnitude of the reflection and transmission coefficients align well with the analytical solution across the frequencies simulated here for both the RCP and LCP components. The non-Möbius transformation method does not align as well as the Möbius transformation method with the analytical solution. The RCP components of the reflection and transmission magnitude do not agree well with the analytical solution for any frequency evaluated. The transmission magnitude is consistently overestimated below the cyclotron frequency and then underestimated above it. The reflection magnitude is consistently underestimated at all frequencies. The LCP component of the reflection and transmission magnitude deviates significantly from the analytical solution at frequencies below the plasma frequency. As the frequency increases, the analytical and numerical results appear to converge.

The Möbius transformation method accurately calculates the transmission angle for the RCP and LCP components with little deviation from the analytical solution shown. There

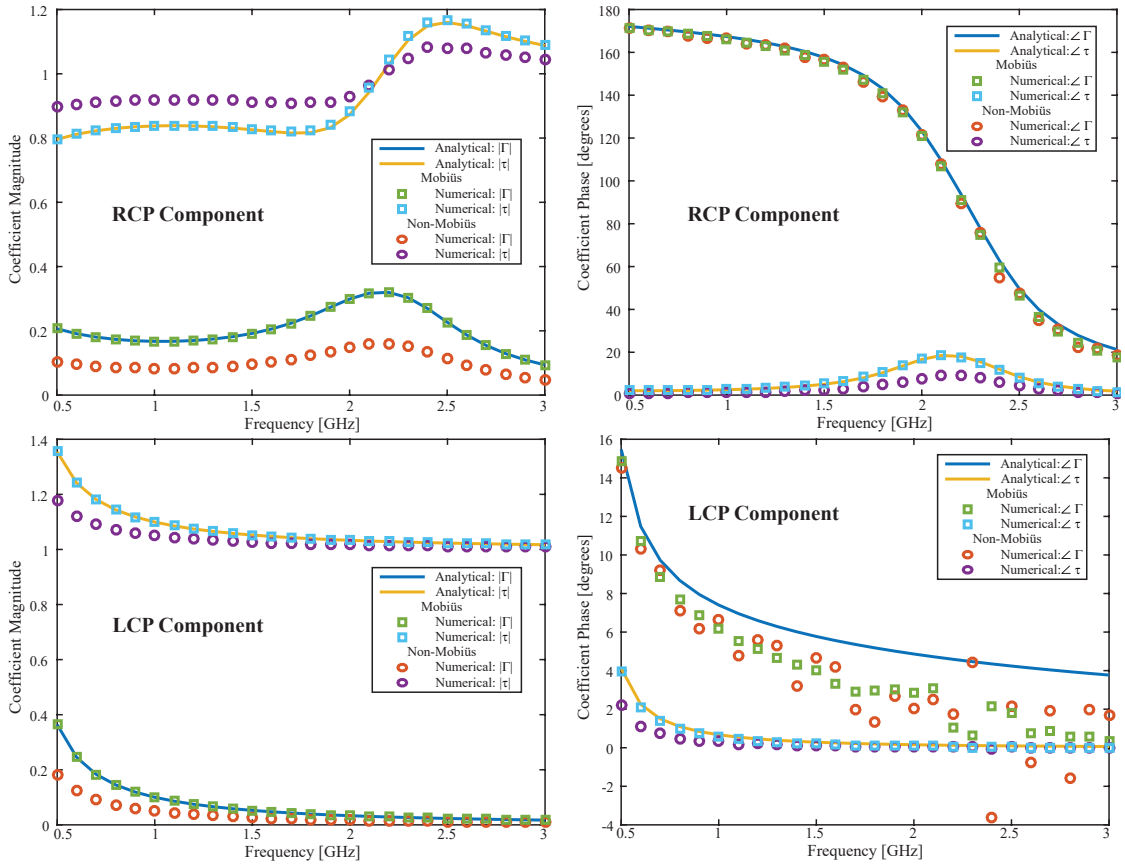

Figure 2-9. Analytical solutions are shown as solid lines and numerical results are shown as squares for the Möbius transformation method and circles for the non-Möbius transformation method (top left) reflection and transmission magnitude for the RCP component, (top right) reflection and transmission angle for the RCP component, (bottom left) reflection and transmission magnitude for the LCP component (bottom right) reflection and transmission angle for the LCP component

is deviation from the analytical solution for the reflection angle in both the RCP and LCP components of up to 4°. The deviation becomes larger as the frequency increases. The non-Möbius transformation method has larger deviations from the analytical solutions than the Möbius transformation method. The transmission angle around the cyclotron frequency deviates by up to 10° for both the RCP and LCP components. The reflection angle accuracy appears similar to the Möbius transformation method for the RCP component but for the LCP component, the non-Möbius transformation method begins to deviate from the analytical solution at lower frequencies.

Figure 2-9 shows that there are significant deviations in the numerical results from the analytical solution when the Möbius transformation is not used to discretize Method 2. These deviations become significantly smaller when Method 2 is discretized using the Möbius transformation. Additionally, the non-Möbius transformation version of Method 2 is found to be unstable at a stability factor of 1. Instead, a stability factor of 0.99 was found to be stable. This is a minor change in simulation time. However, the change from a stability factor of 1 in 1-D does introduce additional simulation noise and reduces accuracy.

2.3 Linear Method Comparison

The maximum time-differential order of each method is expected to greatly affect the performance of each method. Therefore, the five methods are compared to each other in a variety of ways: 1) the numerical results of each method will be compared on an iteration to iteration basis and over an entire simulation, 2) the stability criteria of each method will be found empirically, 3) the memory requirement and computational cost per iteration of each method will be calculated, and 4) how each method is applicable to a nonlinear implementation is determined.

2.3.1 Numerical Comparisons

To determine whether the discretization process has affected the numerical output of each method, the five methods were compared in two ways: 1) from iteration to iteration and 2) over an entire simulation.

The first numerical comparison provides each method with the same inputs and evaluates them on an iteration to iteration basis. This will allow a direct assessment of how the output from the update equations discretized using the MT vary from each other. In order to do this, the field values as calculated by Method 2 are used as the previous time step inputs to the four other methods update equations. The difference between the latest time step of the electric field components of Method 2 and the four other methods is then determined. The peak electric field value in the plasma during this simulation is 1 V/m. The maximum differences in the simulated plasma for the E_x field components between Method 2 and the four other

methods for each iteration are shown in Figure 2-10. It is found that Methods 1 and 5 are negligibly different (on the order of 10^{-15}) from Method 2 on an iteration to iteration basis. Method 3 differs from Method 2 by approximately 2×10^{-15} and Method 4 differs from Method 2 by approximately 5×10^{-15} iteration to iteration. This shows that the five update equations produce nearly identical output values within fifteen orders of magnitude given the same input values on an iteration to iteration basis.

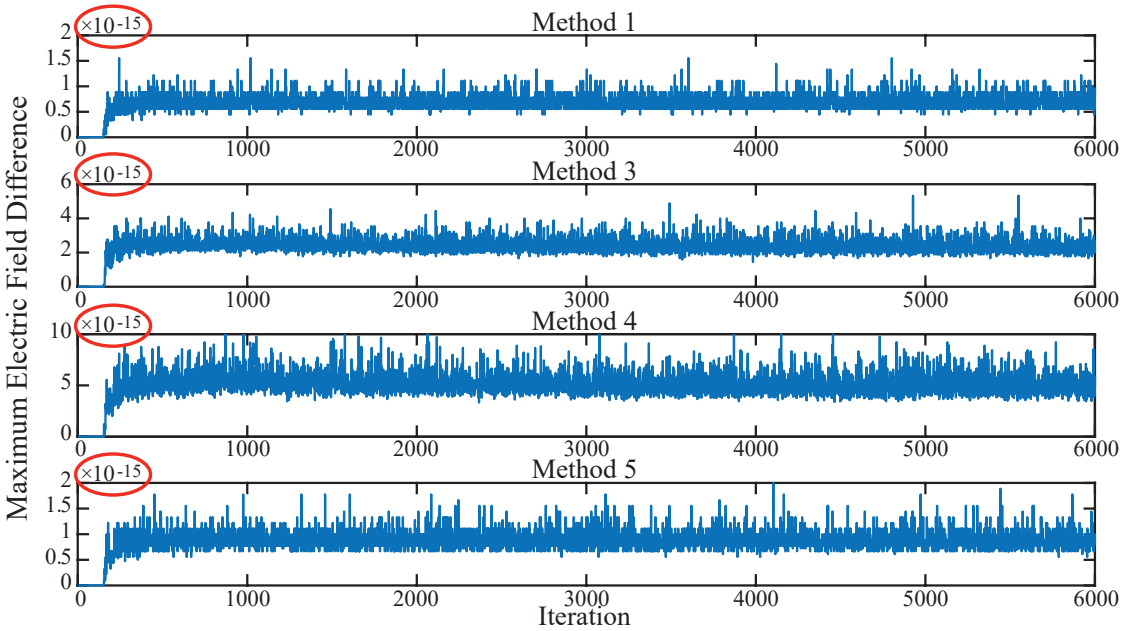

Figure 2-10. The maximum difference in E_x between Method 2 and the four other methods on an iteration to iteration basis.

The second numerical comparison is to allow each method to model propagation from free space into a constant plasma slab for 4800 iterations and compare their output. This allows a comparison of how each method handles a sharp free space to plasma boundary, propagation within the plasma and allows differences to build up over time.

Figure 2-11 shows E_x of Method 2 at iteration 4800 and the difference between E_x of Method 2 and the four other methods. Methods 1 and 5 show the closest agreement to the field values of Method 2, with a difference on the order of 10^{-13}. This is 12 orders of magnitude lower than the peak electric field present inside the plasma. Methods 3 and 4 also

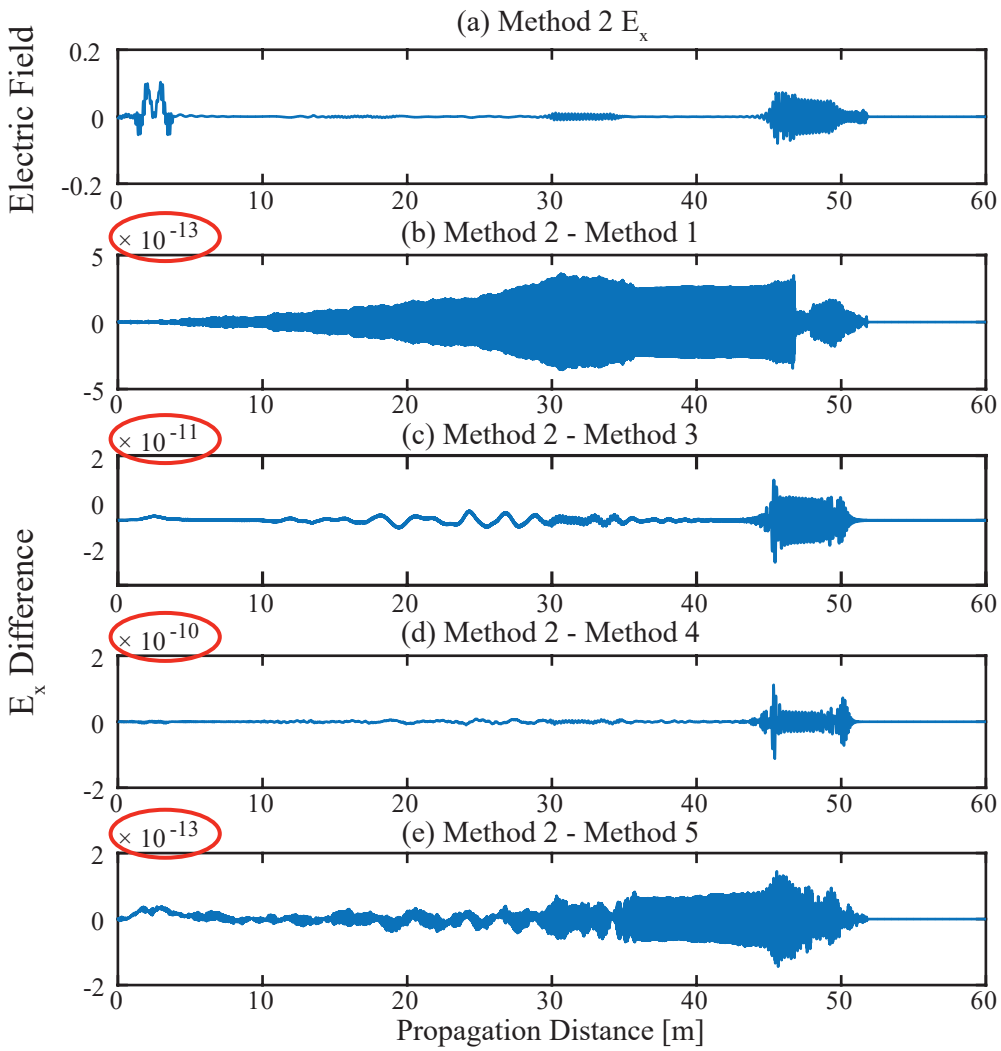

Figure 2-11. (a) E_x of Method 2 at iteration 4800 and (b-e) difference between Method 2 E_x and the four other methods E_x at iteration 4800.

agree well with Method 2 with a peak difference between the two on the order of 10^{-11} and 10^{-10}. Again, these are 10 and 9 orders of magnitude less than the peak electric field.

From these two numerical comparisons, it is seen that all five methods model the cold plasma similarly. The first comparison shows that, provided the same inputs, all five methods will effectively produce the same output at the next iteration. The second comparison shows that all five methods produce a very similar output over many iterations even in the presence of sharp boundaries and when the differences are allowed to build up over time. From these

two comparisons, it is concluded that discretization using the Möbius transformation results in methods that produce nearly identical numerical results.

2.3.2 Stability

Pereda et al. [2002] showed that when the Möbius transformation is used to discretize an Mth-order medium, the stability limit of the conventional FDTD method is preserved. All five methods compared are discretized utilizing the MT. It is found empirically that Methods 1, 2, 3, and 5 are stable in 1-D with a stability factor of 1. In the tests performed, which are described in Section 2.2, no dependence or variation from a stability factor of 1 based upon the values used for ω_p, ν and ω_c were found.

Method 4 is found to have an instability at the free-space to plasma boundary when modeling an electron-only plasma (i.e., $\nu = 0$, $\vec{B}_0 = 0$). This method is stable in all other plasma configurations. The authors are unsure of the exact cause of this instability. A possible explanation is that this method was derived assuming the background magnetic field was along a coordinate axis ($\hat{z}$). This assumption reduced Method 4 from 12^{th}-order time-differentials to 6^{th}-order time-differentials. Implementing this method utilizing the full 12^{th}-order time-differentials may result in a stable electron-only plasma implementation.

2.3.3 Memory and Speed

Two major differences between the five methods considered here are their memory requirements and computational cost per iteration. The main factor that plays into the different memory usage is the order of differentials used for each implementation. For a 3-D FDTD implementation, Method 1 uses first-order differentials, Method 2 uses second-order differentials, Method 3 uses fourth-order differentials, Method 4 uses twelfth-order differentials and Method 5 uses third-order differentials. The higher the differential order, the larger number of previous time steps that are required to be saved and used in the next iteration. This increase in previous time steps required will increase the memory requirement and the computational cost per iteration.

The memory requirement for each method has been split-up between field variables per grid cell and update coefficients per grid cell as shown in Table 2-3 for a 3-D implementation. This distinction is made because a homogenous plasma does not require the additional memory requirement of the update coefficients every grid cell whereas a spatially varying plasma does. It is clear from Table 2-3 that for a 3-D spatially varying plasma that Method 2 uses the least amount of memory. Method 1 uses the next least amount of memory, but still uses about a third more memory than Method 2. The memory usage for Methods 3, 4, and 5 are all substantially more than Method 2.

Method	Field Variables per grid cell	Coefficients per grid cell	Total Memory per grid cell
1	15	72	87
2	21	45	66
3	33	81	114
4	81	114	195
5	12	360	372

Table 2-3. For a 3-D implementation, the memory requirement per grid cell for each method including the field component variables and the update coefficients.

Another significant factor when choosing a numerical method is the computational cost or speed of that method. One way to quantify the computational cost of each method is to determine the number of floating point operations (FLOPs) needed for the update equations. FLOPs include any addition, subtraction, multiplication or division required in the update equations for any field component. This comparison does not include the computational time to reassign memory due to setting field components back in time. Table 2-4 shows the number of FLOPs needed for each method for a 1-D, 3-D without spatial averaging, and 3-D with spatial averaging included implementations. Spatial averaging is required in 3-D in order to collocate field components in the update equations. *Gamliel* [2017] created a grid that collocated all $\vec{E}$, $\vec{D}$, and $\vec{J}$ field values, and collocated all $\vec{H}$ field values. This grid reduces the computational need for spatial averaging, but increases the memory requirements.

The 1-D implementation assumes that the background magnetic field is in the direction of propagation. This way only the two perpendicular field components to the direction of propagation need to be updated. Method 2 is determined to require the fewest FLOPs in 1-D

followed closely by Method 5. The number of FLOPs needed per grid cell in 3-D increases dramatically over the number needed in 1-D. When including the necessary spatial averaging, Methods 1 through 5 increase by a factor of approximately 7.5, 5, 5, 7 and 31, respectively. In 3-D Method 2 requires the fewest FLOPs per grid cell. The method that requires the next fewest is Method 3 that requires 67% more than Method 2. Method 1 requires nearly twice as many FLOPs as Method 2 in 3-D. This is surprising because Method 1 requires differentials of the first-order and Method 2 requires differentials of the second-order. There are two reasons why Method 1 requires so many more FLOPs per grid cell. The first is that the update equations for $\vec{J}$ and $\vec{E}$ include the $\nabla \times \vec{H}$ term. In order to properly locate all of the $\vec{H}$ field components, a large amount of spatial averaging is needed. The second reason is that the six field components of $\vec{J}$ and $\vec{E}$ are updated through a complex and long update equation. In comparison, Methods 2 to 5 only require complex update equations for the three field components of $\vec{E}$. The most drastic difference is the number of FLOPs required for a 1-D versus 3-D implementation of Method 5. The reason for this is that the $\nabla \times \nabla \times \vec{E}$ terms of the wave equation for Method 5 simplify significantly when in 1-D. In 3-D, many more terms spatially surrounding the update location are required which increases the FLOPs because of terms to multiply and add plus the number of FLOPs needed to spatially average.

Method	1-D FLOPs per grid cell	3-D FLOPs per grid cell w/o spatial averaging	3-D FLOPs per grid cell w/ spatial averaging
1	62	201	465
2	50	129	249
3	82	201	417
4	90	345	657
5	54	717	1677

Table 2-4. Floating Point Operations (FLOPs) per grid cell for each method including the field component variables and the update coefficients.

2.3.4 Nonlinear Applicability

In order to properly model nonlinear phenomena, the electron density, N_e, and effective collision frequency, ν, must be treated as time dependent variables in the FDTD methods derivation. Examining the derivations of Methods 1 and 2, it is found that no temporal derivatives of N_e or ν are taken and the methods do not need to be modified in order to take into account a nonlinear plasma. In the process of deriving Methods 3 and 4, frequency

domain analysis is used. This analysis as implemented above is not strictly valid when N_e or ν are allowed to vary temporally. Because of this, these methods would require significant modification to model a nonlinear plasma. Method 5 depends on the derivation of the cold plasma wave equation which in Eq. 2-15, N_e and ν were considered to be constants. Considering N_e and ν as time dependent variables would introduce additional terms into the cold plasma wave equation. By including these additional terms, Method 5 does become a valid method to use to model a nonlinear plasma.

Because Methods 1 and 2 are the only two methods presented here that are able to be used in their current form for a nonlinear plasma, the decision on which method to use is between them. In this dissertation, we are considering electron-only plasmas. In this case, Method 2 is the clear choice because it was shown to require less memory and to be faster than Method 1. Both Method 1 and Method 2 require modification of the update equations when multiple charged species are required in the simulation. *Yu and Simpson* [2010] described how to include multiple charged species for Method 1. Although it is not described in this work, the addition of multiple charged species to Method 2 can be readily implemented. An evaluation of each method's memory and speed when implementing multiple charged species is needed to determine the optimal method, but either method can be utilized to simulate a nonlinear plasma with multiple charged species. Because we consider electron-only plasmas throughout this dissertation, we will use Method 2 in subsequent chapters as applicable.

CHAPTER 3
HF HEATING OF THE D-REGION

In this chapter, an FDTD model of nonlinear HF heating of the lower ionosphere is detailed. The implementation is unique from other nonlinear FDTD models in its focus on discretizing the 1^{st}- and 2^{nd}-order moments of the Boltzmann equation using the Möbius transformation. Simulation results of HF cross modulation are compared to experimental observations performed at HAARP in order to validate the model. The thermal cubic nonlinearity method for VLF wave generation is simulated and the dominant mechanism is confirmed.

3.1 Nonlinear FDTD Model

The basis for the nonlinear FDTD model is Linear Method 2 as described in Chapter 2. This method is chosen for its direct applicability to a nonlinear model, its faster computation time, and its lower memory requirement compared to Linear Method 1. As an electromagnetic wave propagates through a cold, collisional plasma, it interacts with free electrons, heating them. In the most simple case, a variable electron temperature is the main implementation difference between a linear and nonlinear plasma FDTD model. The temperature variation is determined using the second-order moment of the Boltzmann equation (Eq. 3-1), also known as the energy transport equation. Our implementation neglects convection, heat conduction, gravity, and the interaction of the wave magnetic field with the medium:

$$\frac{3}{2}N_e\kappa_B\frac{\partial T_e}{\partial t} = \vec{J}_e\cdot\vec{E} - \frac{3}{2}\kappa_B T_e\frac{\partial N_e}{\partial t} - L(N_e,T_e,T_n) \tag{3-1}$$

where T_e is the electron temperature, N_e is the electron density, κ_B is the Boltzmann constant, and $L(N_e,T_e,T_n)$ is the energy loss due to electron cooling provided by *Rodriguez* [1994] and *Moore* [2007], and references therein.

The inclusion of the second-order moment of the Boltzmann equation further causes the inclusion of numerous other equations. The energy loss term is composed of six equations including the rotational (Eqs. 3-2 and 3-3), vibrational (Eqs. 3-4 and 3-7), and elastic (Eqs.

3-9 and 3-10) excitation of N_2 and O_2 [*Rodriguez*, 1994; *Moore*, 2007]. The total loss is taken to be the sum of these six loss rates (Eq. 3-11).

$$L_{\mathrm{rot}}(\mathrm{e},\mathrm{N_2}) = 4.65\times10^{-39}\mathrm{N_e}\mathrm{N_{N_2}}\left(\frac{\mathrm{T_e}-\mathrm{T_n}}{\mathrm{T_e}^{1/2}}\right) \tag{3-2}$$

$$L_{\mathrm{rot}}(\mathrm{e},\mathrm{O_2}) = 1.11\times10^{-38}\mathrm{N_e}\mathrm{N_{O_2}}\left(\frac{\mathrm{T_e}-\mathrm{T_n}}{\mathrm{T_e}^{1/2}}\right) \tag{3-3}$$

$$L_{\mathrm{vib}}(\mathrm{e},\mathrm{N_2}) = 4.79\times10^{-37}\mathrm{N_e}\mathrm{N_{N_2}}\exp\left(\mathrm{f}\frac{\mathrm{T_e}-2000}{2000\mathrm{T_e}}\right)\left[1-\exp\left(-\mathrm{g}\frac{\mathrm{T_e}-\mathrm{T_n}}{\mathrm{T_e}\mathrm{T_n}}\right)\right] \tag{3-4}$$

where f is a dimensionless parameter given by:

$$\mathrm{f} = 1.06\times10^{4} + 7.51\times10^{3}\tanh\left[0.0011(\mathrm{T_e}-1800)\right] \tag{3-5}$$

and g is a dimensionless parameter given by:

$$\mathrm{g} = 3300 + 1.233(\mathrm{T_e}-1000) - 2.056\times10^{-4}(\mathrm{T_e}-1000)(\mathrm{T_e}-4000) \tag{3-6}$$

$$L_{\mathrm{vib}}(\mathrm{e},\mathrm{O_2}) = 8.32\times10^{-38}\mathrm{N_e}\mathrm{N_{O_2}}\exp\left(\mathrm{f}\frac{\mathrm{T_e}-700}{700\mathrm{T_e}}\right)\left[1-\exp\left(-2700\frac{\mathrm{T_e}-\mathrm{T_n}}{\mathrm{T_e}\mathrm{T_n}}\right)\right] \tag{3-7}$$

where f is :

$$\mathrm{f} = 3300 - 839\sin\left[0.000191(\mathrm{T_e}-2700)\right] \tag{3-8}$$

$$L_{\mathrm{elast}}(\mathrm{e},\mathrm{N_2}) = 1.89\times10^{-44}\mathrm{N_e}\mathrm{N_{N_2}}\left(1-1.21\times10^{-4}\mathrm{T_e}\right)\mathrm{T_e}(\mathrm{T_e}-\mathrm{T_n}) \tag{3-9}$$

$$L_{\mathrm{elast}}(\mathrm{e},\mathrm{O_2}) = 1.29\times10^{-43}\mathrm{N_e}\mathrm{N_{O_2}}\left(1+3.6\times10^{-2}\mathrm{T_e}^{1/2}\right)\mathrm{T_e}^{1/2}(\mathrm{T_e}-\mathrm{T_n}) \tag{3-10}$$

$$L_{\text{Total}} = L_{\text{rot}}(\text{e}, \text{N}_2) + \text{L}_{\text{rot}}(\text{e}, \text{O}_2) + \text{L}_{\text{vib}}(\text{e}, \text{N}_2) + \text{L}_{\text{vib}}(\text{e}, \text{O}_2) + \text{L}_{\text{elast}}(\text{e}, \text{N}_2) + \text{L}_{\text{elast}}(\text{e}, \text{O}_2) \quad (3\text{-}11)$$

In order to solve for the time rate of change of the electron density, a simple four-species chemistry model of the D-region is implemented [*Rodriguez*, 1994; *Rodriguez and Inan*, 1994; *Moore et al.*, 2013]. Compared to the short timescales of microseconds to milliseconds, which apply for many HF heating experiments, changes in species density, and specifically, the electron density, occur on much longer timescales and, therefore, can be neglected. For HF heating experiments that heat continuously for multiple seconds, these chemistry changes cannot be ignored, however. In order to account for both HF heating possibilities in this model, the simple 4-species chemistry model is employed. The four species are electrons (N_e), negative ions (N^-), primary positive ions (N^+), and positive water cluster ions (N_x^+). The inputs to this model are N_2, O_2 and electron density profiles and a neutral species temperature profile, which is also used as the ambient electron temperature profile. Using these inputs, the ambient profiles of the remaining species are calculated. When calculating for the ambient profiles, the time rate of change of the four species is set to zero. After calculating the ambient values as described by *Rodriguez and Inan* [1994] and the wave-propagation begins, the species are allowed to vary in time as shown in Eqs. 3-12 to 3-15.

$$\frac{dN_e}{dt} = I_o + \gamma N^- - \beta N_e - \alpha_d N_e N^+ - \alpha_d^c N_e N_x^+ \quad (3\text{-}12)$$

$$\frac{dN^-}{dt} = \beta N_e - \gamma N^- - \alpha_i N^- (N^+ + N_x^+) \quad (3\text{-}13)$$

$$\frac{dN^+}{dt} = I_o - B N^+ - \alpha_d N_e N^+ - \alpha_i N^- N^+ \quad (3\text{-}14)$$

$$\frac{dN_x^+}{dt} = -\alpha_d^c N_e N_x^+ + B N^+ - \alpha_i N^- N_x^+ \quad (3\text{-}15)$$

The updated electron temperature from Eq. 3-1 is used to calculate the average electron-neutral collision frequency. Collisions with O_2 and N_2 are considered and the rates are taken from *Rodriguez* [1994]. and references therein, shown in Eqs. 3-16 and 3-17.

$$\nu_{av}(e, N_2) = 2.33 \times 10^{-17} N_2 (1 - 1.21 \times 10^{-4} T_e) T_e \tag{3-16}$$

$$\nu_{av}(e, O_2) = 1.82 \times 10^{-16} O_2 (1 + 3.6 \times 10^{-2} T_e^{\frac{1}{2}}) T_e^{\frac{1}{2}}. \tag{3-17}$$

The total average electron-neutral collision frequency is equal to the sum of these two equations and was taken by *Moore* [2007] to be:

$$\nu_{av} = \nu_{av}(e, N_2) + \nu_{av}(e, O_2). \tag{3-18}$$

Assuming that $\nu(v) \propto v^2$, for the frequency range of interest, the effective collision frequency is proportional to the average collision frequency [*Sen and Wyller*, 1960; *Budden*, 1988]:

$$\nu_{\text{eff}} = \frac{5}{3} \nu_{av}. \tag{3-19}$$

In Linear Method 2, the current density $\vec{J}$ is not explicitly discretized and calculated. In order to calculate $\vec{J} \cdot \vec{E}$, the Joule heating term, in Equation 3-1, the current density is needed. Equation 1-1 is solved for the current density to create Equation 3-20 which is then discretized.

$$\vec{J} = \frac{\partial \vec{D}_{\text{eff}}}{\partial t} - \epsilon_0 \frac{\partial \vec{E}}{\partial t} \tag{3-20}$$

A full and proper discretization of Eq. 3-1 using the MT is desired, but is not practical to implement. The MT should be applied to all time-varying field components ($\vec{E}$, $\vec{D}$, $\vec{J}$, and $\vec{H}$) along with all time-varying plasma parameters (T_e, ν, and N_e). Practically, this means that all time-varying terms in Eq. 3-1 ($\vec{E}$, $\vec{J}$, L, T_e, and N_e) should either be center-differenced or center-averaged in time. The difficulty is that the latest time step of N_e and L are not known yet, and are complicated functions of T_e.

$$
\begin{aligned}
T_e^{n+1} = T_e^{n-1} + \\
\frac{4\Delta t}{3N_e^n k_B}\left[\frac{\left(J_x^{n+1}E_x^{n+1} + J_y^{n+1}E_y^{n+1} + J_z^{n+1}E_z^{n+1}\right)}{4}\right. \\
\left.+\frac{2\left(J_x^n E_x^n + J_y^n E_y^n + J_z^n E_z^n\right) + \left(J_x^{n-1}E_x^{n-1} + J_y^{n-1}E_y^{n-1} + J_z^{n-1}E_z^{n-1}\right)}{4}\right] \\
-\frac{2\Delta t T_e^n}{N_e^n}\left(I_o + \gamma^n N^{-^n} - \beta^n N_e^n - \alpha_d^n N_e^n N^{+^n} - \alpha_d^{c^n} N_e^n N_x^{+^n}\right) \\
-\frac{4\Delta t}{3N_e^n k_B}\left[\frac{L^n(N_e^n, T_e^n, T_o) + 2L^{n-1}(N_e^{n-1}, T_e^{n-1}, T_o) + L^{n-2}(N_e^{n-2}, T_e^{n-2}, T_o)}{4}\right]
\end{aligned}
\tag{3-21}
$$

The implementation considerations can be seen more clearly by examining the discretized version of Eq. 3-1, shown in Eq. 3-21, without fully utilizing the MT. The first item to note is that Eq. 3-21 is centered at time step n, therefore all other terms need to be valid and centered at this same time step. The second is that in this discretized version, only the $\vec{J} \cdot \vec{E}$ term is center-averaged in time. This is possible because the J^{n+1} and E^{n+1} terms are known. $L(N_e, T_e, T_n)$ is backwards-averaged in time in order to provide as much consistency with the MT as possible. It is not reasonably possible to center-average the loss rates because they are nonlinear functions of T_e and it is difficult to solve $L^{n+1}(N_e^{n+1}, T_e^{n+1}, T_o)$ for T_e^{n+1}. N_e is not center-averaged in time either because N_e^{n+1} is similarly a nonlinear function of T_e. Justification for using the time-centered value of N_e can be found by looking at the time rate of change of N_e. At a period of steady-state CW heating, the max percent change in N_e between iterations is found to be less than $4 \times 10^{-10}\%$, meaning that the time-centered value and the center-averaged value of N_e would be nearly the same. When T_e is used as a coefficient to the electron density time derivative term it should be center-averaged in time where-as a time-centered value is used. Using the same justification as for N_e, at a period of initial CW heating when T_e is changing the most rapidly, T_e is found to change by less than 0.1% each iteration. The third difference from a MT implementation to note is the time derivative of the electron density is not directly discretized. Instead, the right hand side of Equation 3-12 is used, using time-centered values.

Due to the inclusion of many more equations than a standard free-space FDTD, the update loop becomes a more complicated 9 step process.

1. Update $\vec{D}_{\text{eff}}$ using $\vec{H}$: Eq. 1-1
2. Update $\vec{E}$ using $\vec{D}_{\text{eff}}$: Linear Method 2
3. Calculate $\vec{J}$ using $\vec{D}_{\text{eff}}$ and $\vec{E}$: Eq. 3-20
4. Update T_e: Eq. 3-21
5. Calculate ν_{av} using T_e: Eqs. 3-16 to 3-18
6. Calculate ν_{eff} using ν_{av}: Eq. 3-19
7. Update N_e using the chemistry model: Eqs. 3-12 to 3-15
8. Calculate new update coefficients for step 2
9. Update $\vec{H}$ using $\vec{E}$: Eq. 1-2

Having detailed the nonlinear HF heating model in detail, we now simulate cross-modulation and thermal cubic nonlinearity HF heating experiments, and compare with experimental observations.

3.2 HF Cross Modulation

In order to verify that the nonlinear FDTD HF heating model produces the desired nonlinearities, it was compared to observations performed during an HF cross-modulation experiment and presented by *Langston and Moore* [2013]. Cross modulation, also know as the Luxemburg Effect, occurs when a powerful, modulated radio wave modifies the conductivity of the ionosphere and a second radio wave propagating through this same region has the modulation imparted onto it. For this experiment, HAARP was split into two sub-arrays: one array transmitted a high power 3.25 MHz modifying beam and the other array transmitting a low power 4.5 MHz probe pulse. This is shown schematically in Figure 3-1. Using a specific transmitting schedule, *Langston and Moore* [2013] were able to separate the modulation caused by the upward and downward propagation of the probe pulse through the heated region. In this work, the predictions of the HF heating model are compared to observations of the

up-going cross-modulated wave for four amplitude-modulation (AM) schemes: 2.5 kHz sine, 2.5 kHz square, 10 kHz sine, and Continuous Wave (CW).

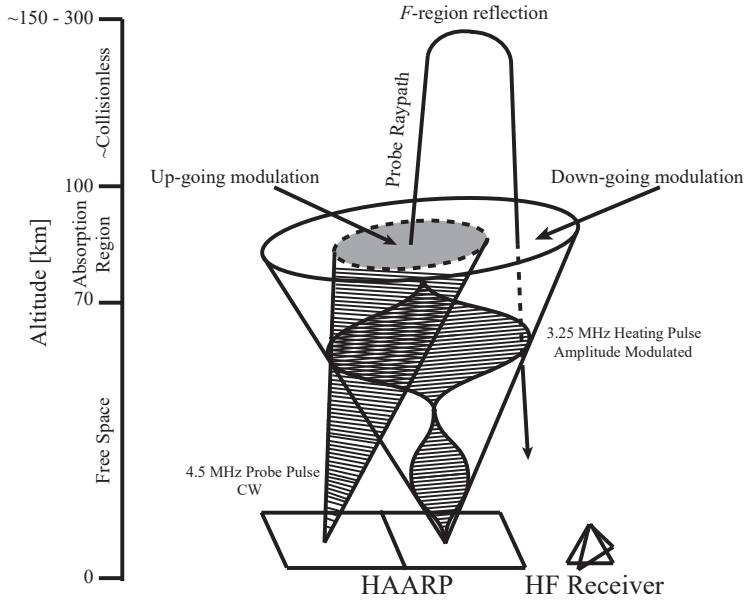

Figure 3-1. Schematic diagram of HF cross-modulation indicating the up-going and down-going modulation of the probe pulse.

To model HF cross modulation, a 1-dimensional FDTD grid was created. The grid spans from 44 km to 103 km altitude with a spatial step size of 3 meters and time step of approximately 10 ns was employed, corresponding to a Courant Stability Factor of 1. This small step size ensured at least 22 grid cells per wavelength for the highest frequency transmitted, 4.5 MHz ($\lambda = 66.6$ m). The wave was injected into free space at 45 km and the lower plasma boundary was set at 50 km. The wave propagated through the plasma and was recorded just before the plasma ended at 100 km. The remaining grid space was set to free space with an absorbing boundary condition to prevent any reflections. It might seem that reflections from the free-space/plasma boundary and the plasma/free-space boundary might cause problems, but this is not the case in practice. At HF frequencies and for ambient conditions at 50 km, the transmission and reflection coefficients are almost identically 1 and 0, respectively. Similarly, at 100 km the reflection coefficient is found to be much less than 1 percent.

In this section, plots of cross modulation 'Magnitude' and 'Phase' are shown. The 'Magnitude' plots are given in dB, and 0 dB represents the magnitude of the probe pulse at the top of the D-region (100 km here) if no heating wave was present. A value, for instance, of -3 dB in the 'Magnitude' plots represents 3 dB of attenuation caused by the increased absorption in the heated plasma. Similarly, the 'Phase' plots are given in degrees where 0 degrees represents the phase of the probe pulse at the top of the D-region if no heating pulse was present. A variation from 0 degrees represents a change in the probe pulses phase caused by the time varying conductivity.

3.2.1 Heating and Cooling

When a high power radio wave propagates through the D-region ionosphere, the wave is absorbed by the collisional plasma. This absorption transfers energy from the radio wave to the plasma, heating the plasma. The D-region ionosphere can be considered a cold plasma, so that the neutral species are not significantly heated and can be considered to remain at their ambient temperature. The electron temperature can change significantly from the ambient value, however, and because the electron-neutral collision frequency is a function of electron temperature, the collision frequency will also vary in time. The time-varying collision frequency also results in a time-varying ionospheric conductivity. This time-varying conductivity thus imparts the modulation of the high power radio wave to the lower power radio wave.

The electron temperature profile was recorded as a function of time for a CW heating wave, as shown on the left of Figure 3-2. As the CW wave propagates through the simulated ionosphere, it can be seen that the electron temperature increases with time. The electron temperature begins at the ambient value, which varies with height, but is approximately 200 K. At $100\ \mu s$ into the simulation, the wavefront is at 75 km altitude and the peak electron temperature is close to 500 K at 68 km. In only $400\ \mu s$, the steady-state heated electron temperature profile is nearly attained. At $800\ \mu s$, the steady-state heated electron temperature profile is attained with a peak electron temperature of almost 1500 K at 79 km altitude. The

heated steady-state profile is maintained when the Joule heating term equals the energy losses from the change in electron density and electron cooling in Eq. 3-1.

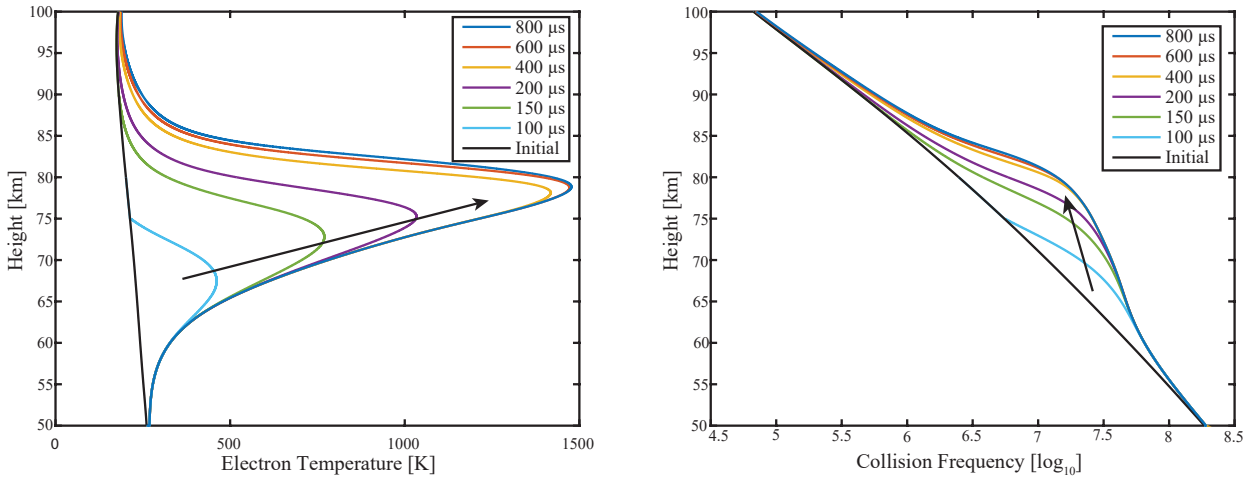

Figure 3-2. (left) Heating of electron temperature and (right) increase in collision frequency from CW wave heating.

The heated collision frequency profile is shown on the right of Figure 3-2. Because the collision frequency is a function of electron temperature, many of the same observations can be made: mainly that the heated steady-state collision frequency is nearly reached in $400\ \mu s$ with steady-state achieved in $800\ \mu s$. The ambient collision frequency profile decreases exponentially with height and the heated profile similarly decreases with height. Because of this, the heated steady-state collision frequency profile does not exhibit a clear and distinct maximum like the electron temperature does. Instead, a maximum increase over ambient can be found to be around 80 km with an increase of nearly a factor of 10.

When the high power radio wave is no longer present in the ionosphere, the Joule heating term is zero. The electron cooling loss rates then dominate Eq. 3-1 and the electron temperature and collision frequency quickly (~0.5 msec) return toward their ambient values. This effect can be demonstrated well using square wave heating. On the left of Figure 3-3, the electron temperature is shown to be recovering toward its ambient value. At $300\ \mu s$, one square wave heating pulse has propagated through the simulation space, increasing the electron temperature to a peak of 1300 K at 77 km. At this time, the transition from heating pulse to

no wave is at 75 km. For the next $200\ \mu s$, there is no heating wave in the upper simulation space because this is the 'OFF' period of the square wave heating. The electron temperature recovers toward ambient, but does not reach ambient, before the next heating pulse is incident upon the ionosphere. The next heating pulse can be seen in the $450\ \mu s$ profile around 57 km and more distinctly in the $500\ \mu s$ profile between 50 and 74 km.

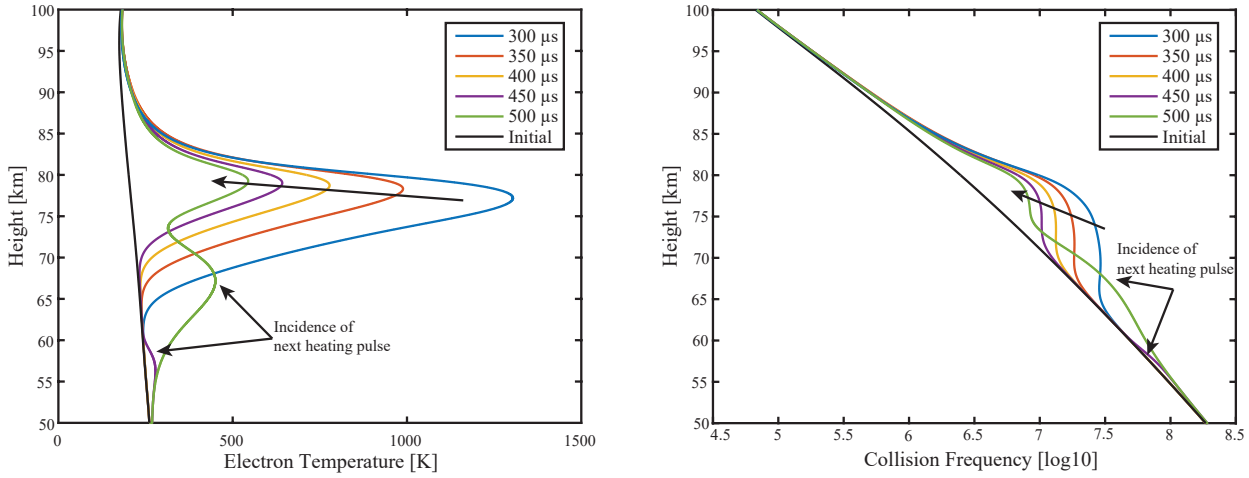

Figure 3-3. (left) Cooling of electron temperature and (right) decrease in collision frequency from 2.5 kHz Square wave heating.

The cooling collision frequency profile is shown on the right of Figure 3-2. Similar to the electron temperature, the collision frequency decreases back toward the ambient value when the heating pulse is not present. Also present in the collision frequency profiles at $450\ \mu s$ and $500\ \mu s$ are the collision frequency increases caused by the next heating pulse incident into the simulation space.

3.2.2 Model Input Observations

With any ionospheric propagation model, the input conditions for the background, steady-state ionosphere will have a significant effect on the results. In this work, three different electron density profiles [*Inan et al.*, 1992; *Moore and Agrawal*, 2011] along with four different neutral density and temperature profiles [*Moore and Agrawal*, 2011] as shown in Figure 3-4 were examined. Electron density profile III is the most dense, followed by profile II, and profile I is the least dense. For the neutral profiles, below 90 km where most of the heating and

absorption occurs, profile 4 is the most dense, followed by profile 3, then 2, and profile 1 is the least dense. The combination of these three electron density profiles and four neutral profiles results in twelve very different background ionospheric profiles.

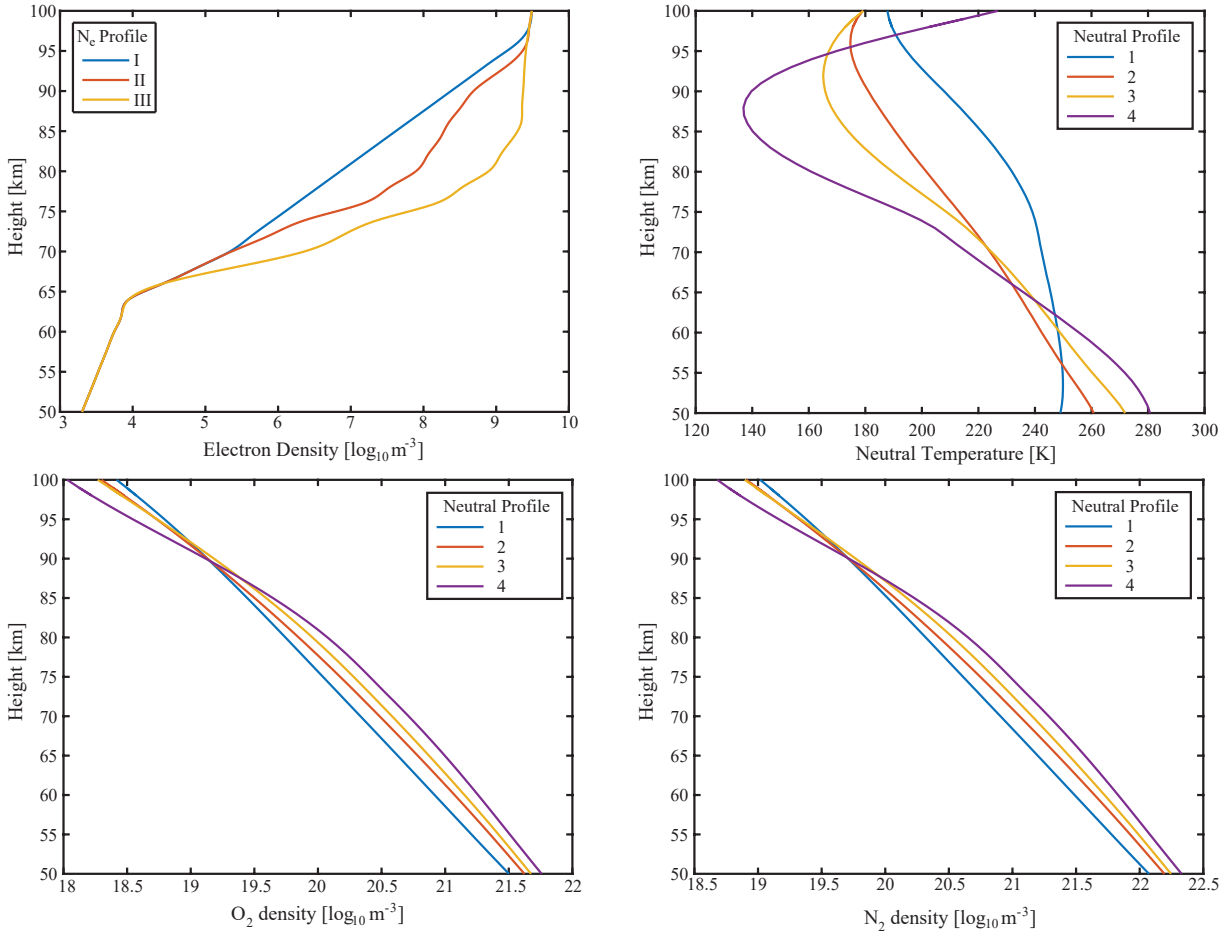

Figure 3-4. (top left) Initial electron density profiles, (top right) neutral temperature profiles, (bottom left) O_2 profiles, and (bottom right) N_2 profiles

The effects of varying the background neutral profile can be seen by plotting the modulation for each neutral profile together using the same electron density profile. Using electron density Profile III, the left panel of Figure 3-5 shows the modulated magnitude of the probe pulse using the 2.5 kHz sine modulation scheme for the four different neutral profiles. At steady-state, the maximum change in magnitude of -3.5 dB is similar for all four profiles. The main difference between the traces is how much the ionosphere recovers back to ambient (the minimum magnitude change). Neutral profile 1, the least dense, recovers the least, and has

a peak to peak amplitude of 1.2 dB. Neutral profile 2 recovers the next least (1.4 dB), then profile 3 (1.6 dB), and profile 4 recovers the most (1.8 dB). The amount of recovery is in order of the profile's density, with profile 4 being the most dense and resulting in the largest recovery.

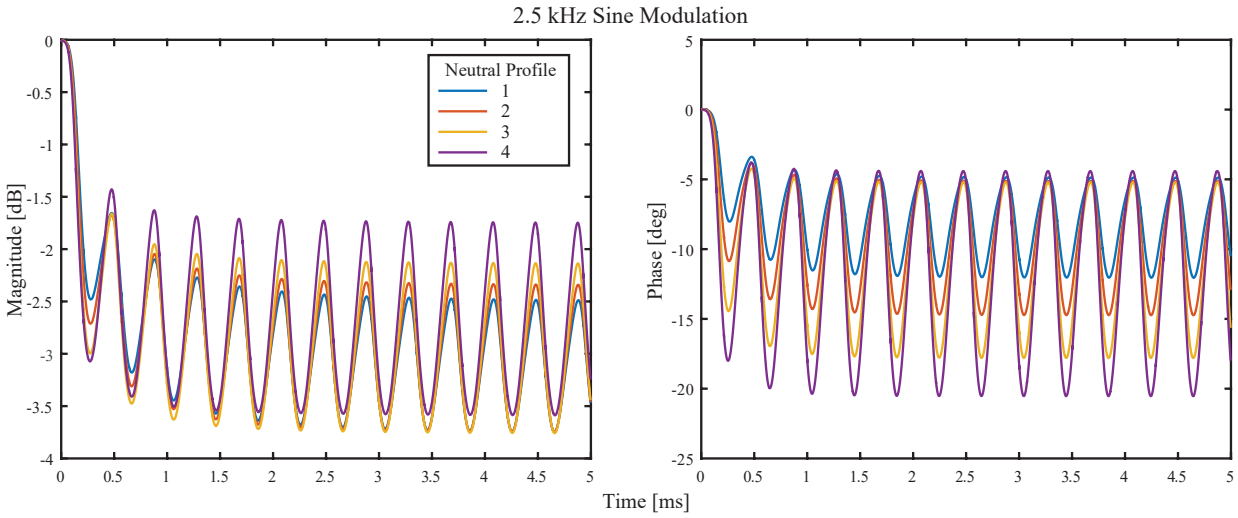

Figure 3-5. Effect of neutral profile on the modulated magnitude and phase

The neutral profile has a more pronounced impact on the modulated phase, however. The right panel of Figure 3-5 shows the modulated phase of the probe pulse for the same electron density Profile III and the four different neutral profiles. Unlike the magnitude, the phase for the four profiles recovers to the same phase of -5°. The maximum phase deviation differs significantly amongst the neutral profiles, from -20.5° to -12°. Again in order of profile density, profile 1 produces the least phase change (-12°), followed by profile 2 (-14.6°), then profile 3 (-17.8°), and then profile 4 the most (-20.5°). Profile 1 experiences a peak to peak phase change of 7° whereas profile 4 has a peak to peak change of 15.5°, more than twice as much.

The ambient electron density profile has a significant effect on both the modulated magnitude and phase as shown in Figure 3-6 for the 10 kHz sine modulation scheme as well. The attenuated magnitude in dB for electron density profile III is 2 and 3 times greater than that of Profiles II and I, respectively. Additionally, peak to peak attenuation is 4 times greater for Profile III over Profile II and 10 times greater for Profile III over Profile I. Similar

observations can be made for the modulated phase. The average steady state phase difference is about 4 times greater for Profile III than for Profile II, and 14 times greater for Profile III than for Profile I. The peak to peak phase change is 5 times greater for Profile III than for Profile II, and 25 times greater for Profile III than for Profile I. It is interesting to note that the magnitude plots for Profiles I and II do not appear to reach steady state in the 5 ms shown here, but that the phase plots do reach steady-state. This effect implies that the attenuation rate depends on collision frequency at high collision frequencies, but the phase propagation constant does not, at least not to the same extent.

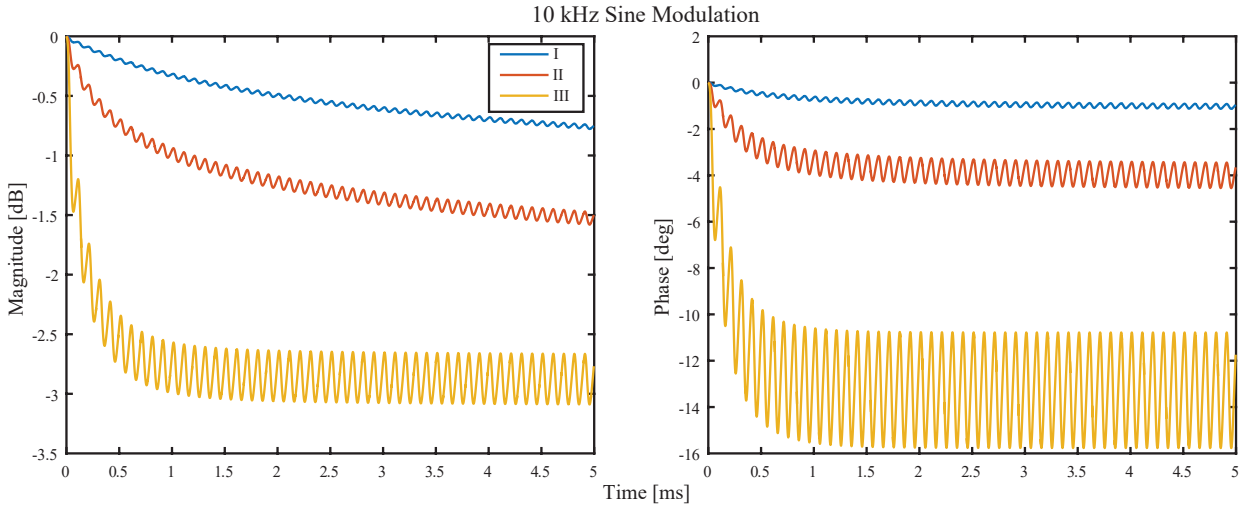

Figure 3-6. Effect of electron density profile on the modulated magnitude and phase for 10 kHz sine wave modulation

Because this is a 1-dimensional FDTD model, spherical spreading of the transmitted wave does not occur. Effectively, the model implements a plane wave infinite in extent in the xy-plane propagating in the $\hat{z}$ direction. This is especially important when determining the input amplitude of the heating pulse. In the experiment of *Langston and Moore* [2013], HAARP transmitted the 3.25 MHz heating pulse with an ERP of 78 dBW. Using the time averaged Poynting flux and assuming spherical spreading, this value can be converted into equivalent electric field amplitudes at altitudes in the D-region. These electric field values vary with altitude in a way not captured by a 1-dimensional attenuating plane wave, and so a range of electric field amplitudes are used to represent an ERP of 78 dBW. The calculated electric

field amplitudes can then be used as the input amplitude at the injection height of 45 km. It is important to note that these equivalent electric field amplitudes do not include the effects of absorption (which are expected to be small) in the region below the calculated height, but they do account for the spherical spreading of the wave.

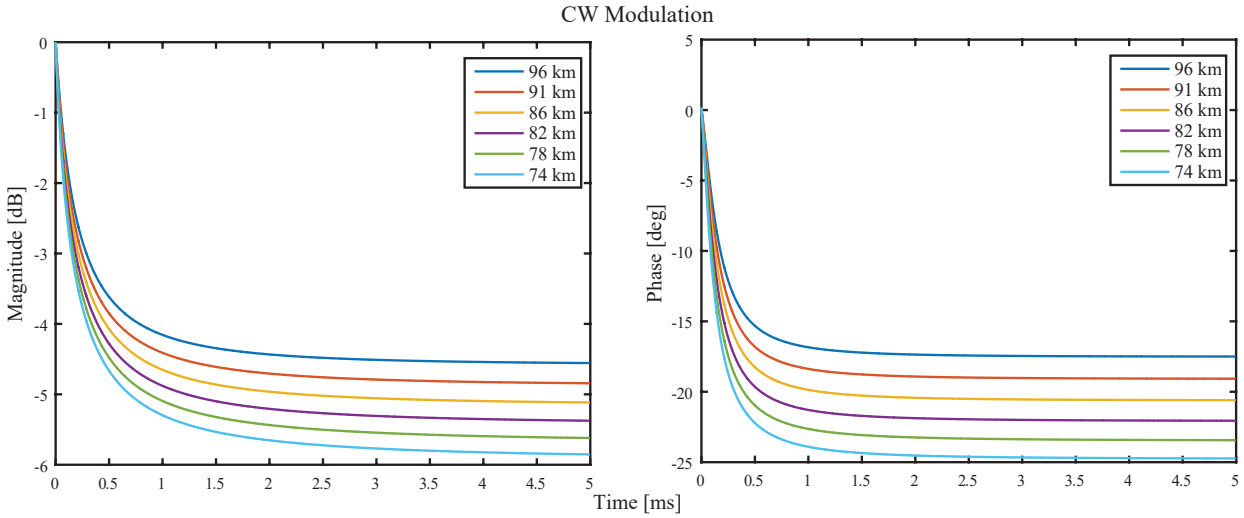

Figure 3-7. Effect of electric field source amplitude on the modulation magnitude and phase. 74 km to 96 km represent the effective electric field at these altitudes from a 78 ERP transmitter on the ground used as the source at 45 km.

As the injection height of the electric field increases, the amplitude of the input electric field decreases. The weak electric field will therefore heat and modify the ionosphere to a lesser extent. This will cause the 4.5 MHz probe pulse to be modulated less as the injection altitude increases. The effect of varying the input electric field amplitude on the modulation magnitude and phase can be seen in Figure 3-7 for the CW modulation scheme. By varying the input electric field amplitude corresponding to spherical spreading amplitudes achieved between 74 km to 96 km, it can be seen that the steady-state modulation magnitude varies by approximately 1 dB. Additionally, it is seen that the steady-state phase varies by approximately 8°. Roughly speaking, these are variations of ~20 - 30% (in dB and degrees). A 3-D implementation would be required to capture this physical effect properly, but such an implementation is not possible at this point in time due to memory and run-time constraints.

The effect of the grid step size was additionally investigated to verify that the results would not be affected by increased resolution. With a step size of 3 meters, there are 22.2 and 30.75 grid cells per wavelength for 4.5 MHz and 3.25 MHz, respectively. If the step size is decreased by a factor of 2 to 1.5 meters, then there are 44.4 and 61.5 grid cells per wavelength. It was found that this substantial increase in grid density does not have a substantial effect on the output modulated magnitude and phase. For the CW wave at steady-state, the modulated magnitude was found to change by less than 0.03 dB and the modulated phase by less than 0.4 degrees. These changes are minor in comparison to the effects that the neutral density or electron density profile have been shown to have. Decreasing the step size by half also means that the time step decreases by half from 10 ns to 5 ns. This results in a program run-time that is approximately 4 times slower.

3.2.3 Experiment vs Simulation

The experimentally measured cross-modulated magnitude and phase for the up-going wave for the four different modulation schemes (2.5 kHz sine, 2.5 kHz square, 10 kHz sine, and CW) are plotted on top of each other in the top panels of Figure 3-8, which are re-plotted versions of the data shown in Figure 2 from *Langston and Moore* [2013]. The bottom two panels show the FDTD simulation results. All simulations were run using neutral profile 4 and electron density profile 3. In these simulations, 0 dB magnitude or 0 degrees phase express amplitude and phase of the probe pulse at the top of the D-region ionosphere relative to when the heating pulse is not present. The x-axis represents time starting at the beginning of the 3.25 MHz 'ON' pulse.

Similarities between the experimental and simulation data sets are easily seen and comparisons between the different modulation schemes are easily made. All four schemes utilized a 78 km injection height and produce a rapid (0.5 ms) decrease in magnitude and phase. The CW modulation runs reach steady state in about 1 ms in both data sets, and this level appears to provide the lower boundary for all of the the modulated magnitudes and phases. The square wave magnitude and phase precede that of the 2.5 kHz sine wave by

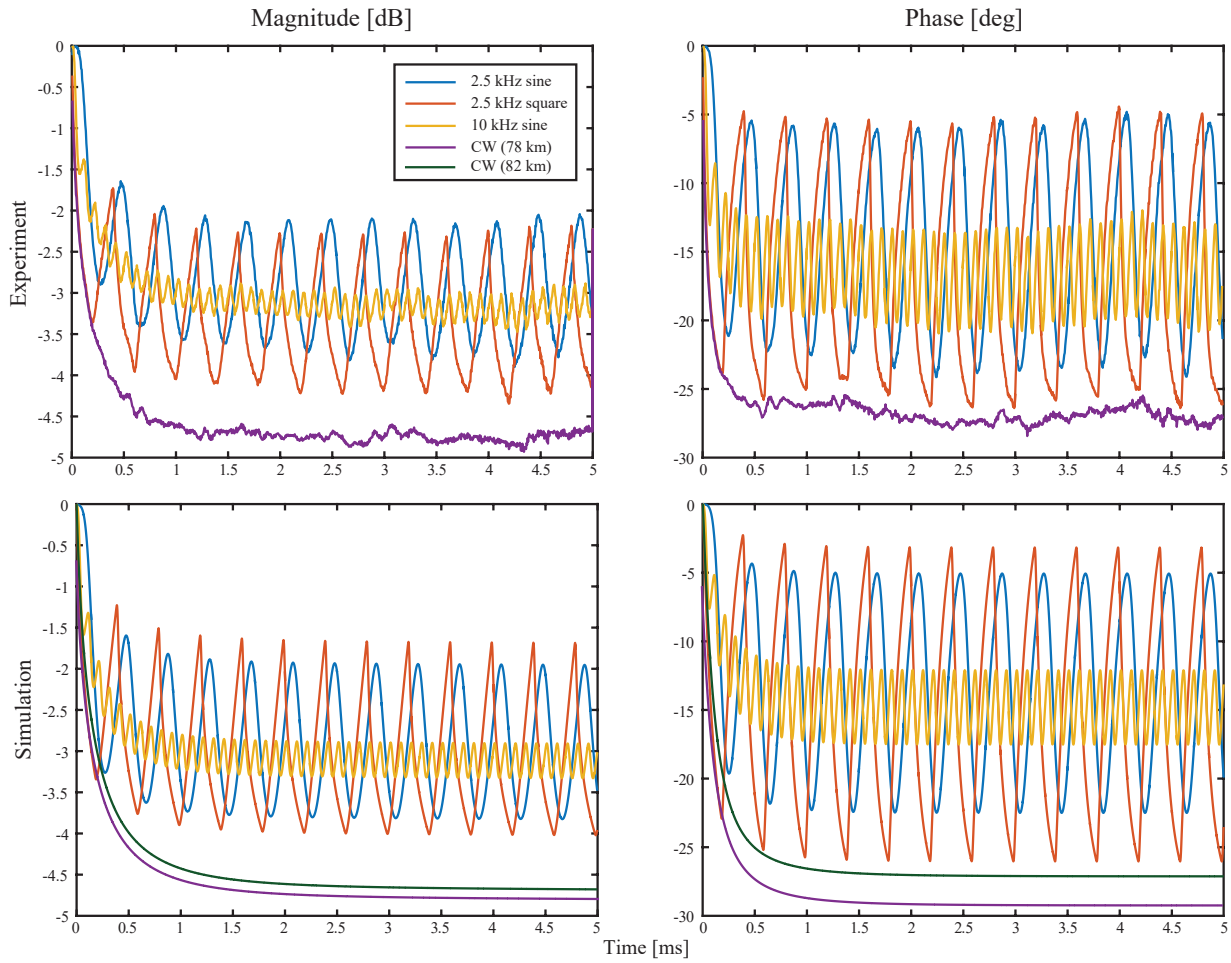

Figure 3-8. Magnitude attenuated and phase change for up-going cross-modulation (top) experiment and (bottom) simulation.

0.125 ms, a time delay corresponding to the ~0.125 ms delay between the $1/2$ power points of the square wave and sinusoidal AM modulation schemes. The peak to peak magnitude and phase of the 10 kHz sine wave is significantly less than that of the 2.5 kHz sine and square wave modulation. The relationship is expected to depend on the heating and cooling rates of the ionosphere and therefore the constituents of the ionospheric plasma. It is noted that in the simulated results, the 2.5 kHz square wave decreases in magnitude and phase at exactly the same rate as the CW wave with the 78 km injection height, similar to the experimental observations. If different injected field amplitudes had been used, the CW modulation scheme would not act as a lower bound. This can be seen with the 82 km injection height for the CW

modulation not acting as a lower bound initially when compared to the 78 km injection height 2.5 kHz square wave modulation. Because the CW wave is slightly weaker than the square wave, the initial drop-off in magnitude and phase is slower than the square wave.

To better compare the two data sets for each individual modulation scheme, Figure 3-9 overlays the experimental and simulated cross-modulation magnitudes and phases. It is clear that the simulations accurately reproduce the experimental observations. For the time-varying modulation schemes, the FDTD model accurately recreates the initial decrease from ambient in modulation magnitude and phase for the first period of heating. The timing of the peaks for the magnitude and phase are found to closely align during the entire heating experiment for the three time varying modulation schemes (2.5 kHz sine, 2.5 kHz square, and 10 kHz sine), implying accurate reproduction at the modulation frequency and its harmonics.

For the modulation magnitude, the peak to peak magnitudes for the 2.5 kHz sine and 2.5 kHz square wave are seen to differ slightly, but by no more than 0.5 dB. The 10 kHz sine wave magnitude peaks nearly perfectly align with that of experimental data. For the modulated phase, the peak to peak phases for the 2.5 kHz sine and 2.5 kHz square wave again differ only marginally, by less than 3°. The 10 kHz sine wave peaks differ slightly more. The main difference for this is because at steady-state, the phase oscillates around -17° for the experimental data and -15° for the modeled data.

For the CW wave using the 82 km field injection amplitude, the initial drop-off in modulated magnitude and phase is replicated well. Furthermore, the steady-state is reached in approximately the same time and with a very similar modulated magnitude and phase. The 78 km field injection amplitude reproduces the initial decrease better than the 82 km field injection amplitude, however, the 78 km field injection amplitude overestimates the steady-state modulated magnitude and phase. Because of this, the 82 km field injection amplitude is shown here.

The accurate reproduction of the initial deviations in magnitude and phase implied accurate modeling of the ambient conditions. The fact that the higher harmonic content of

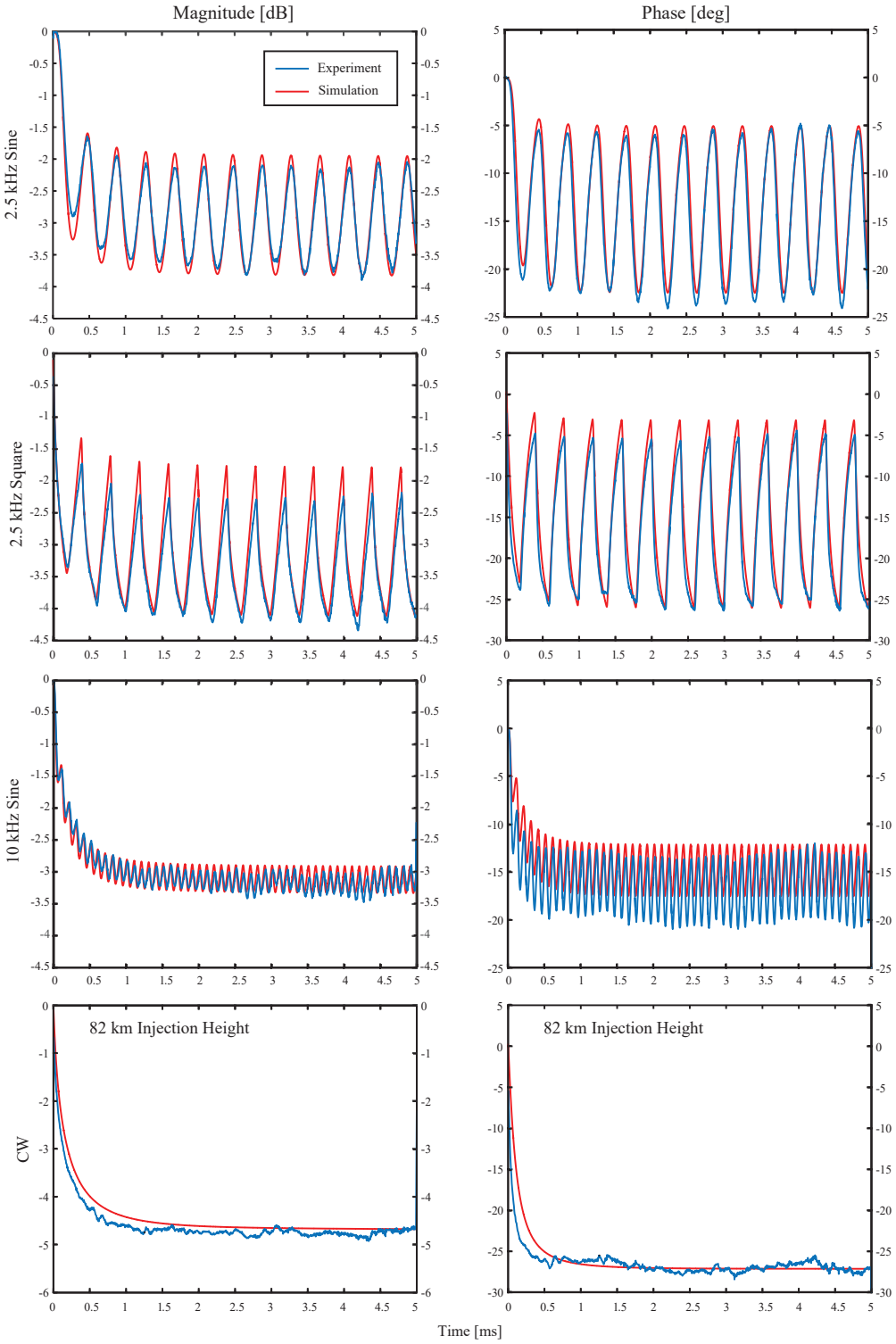

Figure 3-9. Magnitude attenuated and phase change for up-going cross-modulation from experimental data and simulation results plotted together.

the modulation or the steady state value for CW are not matched as well implies that the specific relationship between electron temperature and electron energy loss rate could possibly be improved.

3.2.4 Effective Doppler Shifts

The rapidly varying phase shown in Figure 3-9 can be interpreted as an equivalent Doppler shift. *Langston and Moore* [2013] gave the equivalent Doppler shift velocity as:

$$v(t) = \frac{-c\Delta f(t)}{f_0 + \Delta f(t)} \quad \text{with} \quad \Delta f(t) = \frac{1}{2\pi}\frac{\mathrm{d}\psi(t)}{\mathrm{d}t} \tag{3-22}$$

where $\psi(t)$ is the modulated phase, c is the speed of light, and f_0 is the probe pulse frequency which is 4.5 MHz. The experimental and modeled effective Doppler shift velocity are plotted together in Figure 3-10. It is seen that the experimental and modeled data agree well. The approximately +60 km/sec velocity for 2.5 kHz square and +40 km/sec velocities for 2.5 kHz sine and 10 kHz sine observed by *Langston and Moore* [2013] are all reproduced. This is unsurprising because the Doppler shift velocity is a byproduct of the modulated phase which was seen in Figure 3-9 to align very well for all four modulation schemes. It is interesting that the 10 kHz sine modulated phase did not align well, but the effective Doppler shift velocity does. This is because the Doppler shift is a product of the time rate of change of the modulated phase which was accurately modeled for the 10 kHz sine modulation scheme. Reproduction of these results validates the claim by *Langston and Moore* [2013] that the rapidly varying phase is produced by HF heating and not a change in F-region reflection height, for instance.

3.3 High Frequency Oscillations

A unique feature of this HF heating code is the ability to directly calculate the high frequency oscillations of electron density, electron temperature, and electron-neutral collision frequency. HF oscillations of electron density and electron temperature are shown in this section and HF oscillations of collision frequency are shown in Section 3.4.

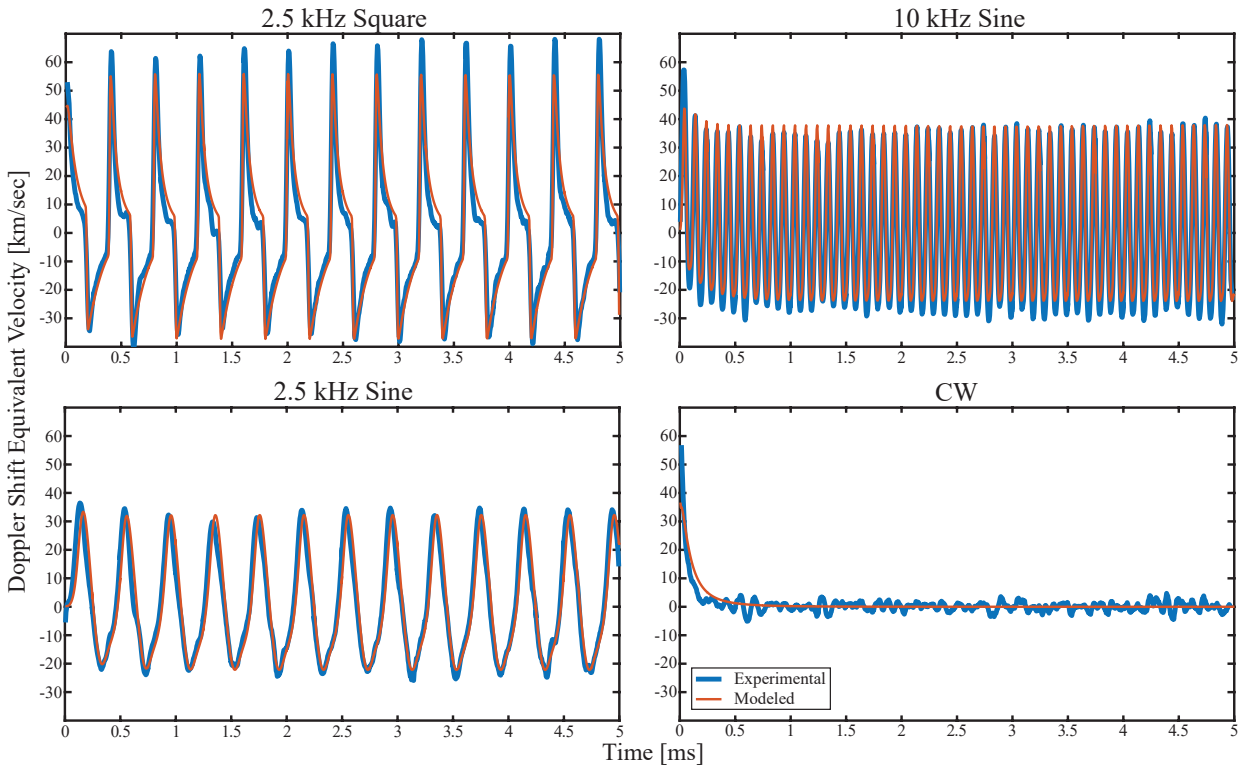

Figure 3-10. Effective Doppler shift velocities on the 4.5 MHz probe signal due to ionospheric heating using four different modulation waveforms

3.3.1 Electron Temperature Oscillations

Electron temperature is calculated through the second-order moment of the Boltzmann equation, Eq. 3-1. The term causing the HF oscillations in the electron temperature is the Joule heating term, $\vec{J} \cdot \vec{E}$. Because the Joule heating term is a dot product of two terms expected to be primarily oscillating at the source frequency, the electron temperature is expected to oscillate at simple combinations of these frequencies.

Shown in the left half of Figure 3-11 is the FFT of electron temperature at 80 km taken from the cross-modulation simulation of 2.5 kHz sine wave amplitude modulation. The source frequencies here are a strong 3.25 MHz wave amplitude modulated at 2.5 kHz and a weaker 4.5 MHz CW wave. There are three peak frequencies that are well over 80 dB higher in magnitude than any other frequency and these are 1.25 MHz, 6.5 MHz, and 7.75 MHz. These can be thought to be the mixing of 4.5 MHz with 3.25 MHz yielding 1.25 MHz and 7.75 MHz, and the mixing of 3.25 MHz with itself to give 6.5 MHz. It is not readily seen due to the scale

of the x-axis, but the magnitude of the electron temperature oscillation at 2.5 kHz is +35.9 dB.

It is interesting to note that there are electron temperature oscillations at 3.25 MHz and 4.5 MHz, but these are not significant. The magnitude of electron temperature oscillations at 3.25 MHz and 4.5 MHz are -150.7 dB and -166.3 dB, which are 122.4 dB and 138 dB less than the magnitude at 6.5 MHz.

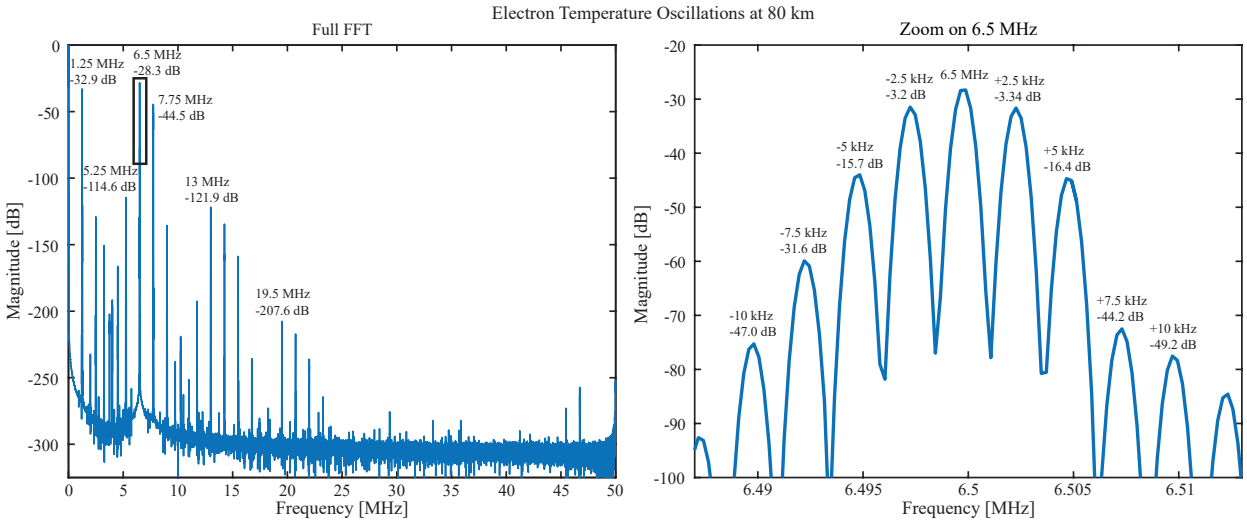

Figure 3-11. (left) FFT of the HF electron temperature oscillations occurring during the 2.5 kHz sine wave cross-modulation experiments. (right) Enlarged portion showing the central oscillation around 6.5 MHz and four harmonics at 2.5 kHz intervals on either side.

The right half of Figure 3-11 shows an enlargement of the electron temperature oscillations around 6.5 MHz. The plot focuses on the central 6.5 MHz and first four harmonics of 2.5 kHz, but the harmonics continue to the noise floor at -300 dB. The FFT clearly shows that the electron temperature oscillates at the expected frequency of 6.5 MHz and mixes with the 2.5 kHz frequency of the amplitude modulation to create numerous harmonics. These harmonics are shown to be slightly asymmetric in magnitude with the positive going harmonics decreasing faster in magnitude than the negative going harmonics. It is noted that harmonics at 2.5 kHz intervals are seen around all of the dominant frequencies shown on the left of Figure 3-11. The spectrum can be thought of as a series of delta functions convolved with

a sinc function, a process that results from the kaiser window applied to the data set before converting to the frequency domain.

3.3.2 Electron Density Oscillations

Electron density changes are not expected to be large for the time scales and power levels involved during cross-modulation and thermal cubic nonlinearity experiments. Similarly, HF oscillations of the electron density are expected to be small. In fact, some models completely neglect the second term on the right hand side of Eq. 3-1, assuming that the change in electron density is zero [*Marshall*, 2014; *Moore*, 2007]. More recent works have accounted for steady-state changes in electron density [*Langston and Moore*, 2013; *Agrawal and Moore*, 2012], however they have not calculated high frequency oscillations of N_e.

The electron density was recorded at 7.5 ms into a thermal cubic nonlinearity simulation (the specifics for which are described in Section 3.4) and compared with the initial ambient profile in Figure 3-12. In this simulation, the source transmitted at two frequencies: $\omega_1 = 2.74$ MHz and $\omega_2 = 5.51$ MHz. The left panel shows the percent change in electron density as compared to the ambient values. It is clear that the largest percent changes in electron density occur between 50 and 75 km with a maximum decrease in electron density of -3.35% at 56 km. Above 75 km, the percent change in electron density is practically zero percent.

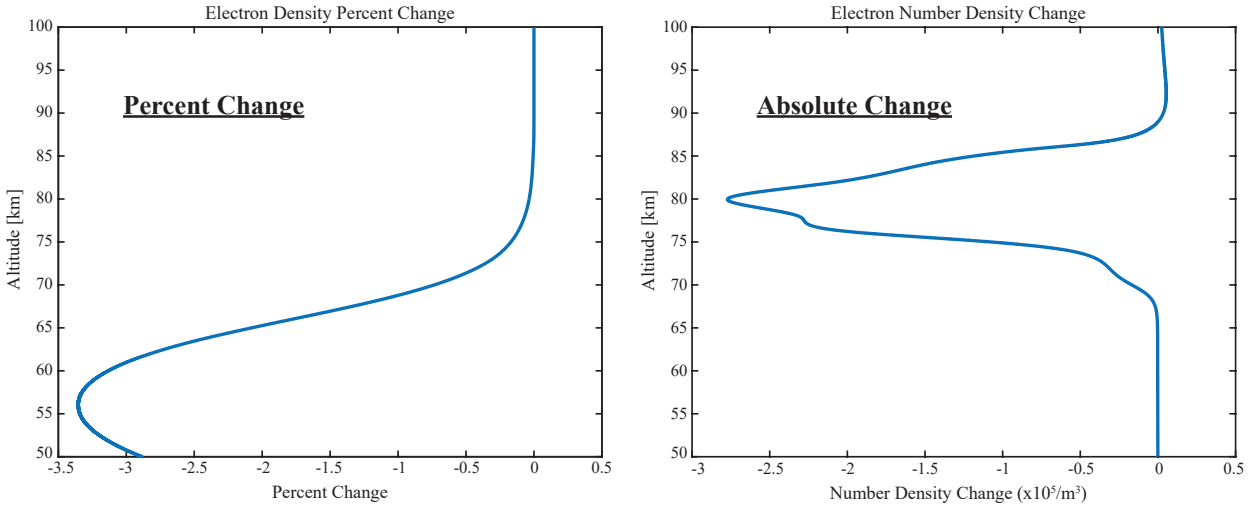

Figure 3-12. 7.5 ms into a thermal cubic nonlinearity simulation: (left) percent change in electron density, and (right) absolute change in electron density.

It is interesting to compare the results of the percent change in electron density to those of the total absolute change in electron density seen in the right panel of Figure 3-12. Below about 75 km in the absolute change, the electron density appears not to change at all. This is contrasted with the percent change which showed the largest variations below 75 km. This discrepancy is due to the fact that the electron density increases nearly exponentially with height in this region. The largest absolute change in electron density occurs at 80 km with a change of $-2.77 \times 10^5\,\mathrm{e/m^3}$. The ambient electron density at this height is nearly $1 \times 10^9\,\mathrm{e/m^3}$ which is nearly four orders of magnitude larger than the change. Conversely, at 56 km the ambient electron density is $3700\,\mathrm{e/m^3}$ and the change in electron density was $-124\,\mathrm{e/m^3}$, which is a 3.35% change. So despite the total number density change being much larger at higher altitudes, the percent change becomes negligible. This is important because many of the nonlinear D-region interactions of interest to this work occur around 80 km. The small percent change in electron density shows that the term involving electron density changes in Eq. 3-1 does not play a significant role in the electron temperature change.

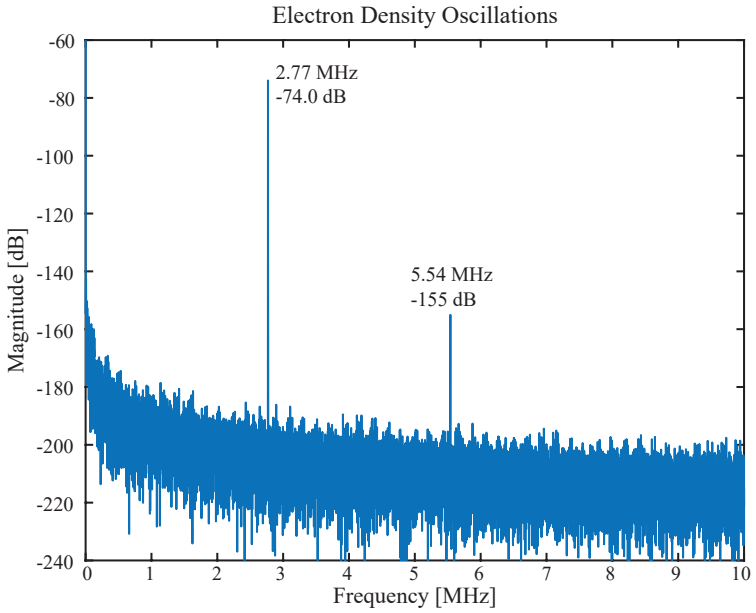

Figure 3-13. Electron density oscillations at 80 km altitude taken from a thermal cubic nonlinearity simulation.

Because the electric field transmitted is in the HF range, the electron density is expected to oscillate at HF frequencies as well. The electron density was recorded at 80 km every iteration up until 7.5 ms into a thermal cubic nonlinearity experiment. The first 1.5 ms were discarded and the electron density was windowed and the FFT taken. The spectrum of electron density oscillations can be seen in Figure 3-13. There are two strong peaks present. The strongest is at 2.77 MHz, which is $|\omega_2 - \omega_1|$, with a magnitude of -74.0 dB. The next peak is at twice the frequency at 5.54 MHz, which is $2|\omega_2 - \omega_1|$, with a magnitude of -155 dB. Because the relative change in electron density is low, these HF oscillations are not thought to play a significant role in the important nonlinear interactions for D-region HF heating experiments.

3.4 Thermal Cubic Nonlinearity

The investigation of ELF/VLF wave generation through the thermal cubic nonlinearity (TCN) [*Ginzburg*, 1964; *Gurevich*, 1978; *Barr*, 1996; *Kotik and Ermakova*, 1998; *Moore et al.*, 2013] is ideally suited for this HF heating model. In the context of ELF/VLF wave generation, most techniques require the presence of the auroral electrojet, a naturally-occurring static current. The thermal cubic nonlinearity is electrojet independent, however, and ELF/VLF wave generation by excitation of the thermal cubic nonlinearity represents an important means to address the reliability of ELF/VLF wave generation.

3.4.1 Dominant Mechanism

This work aims to demonstrate that the dominant mechanism of the thermal cubic nonlinearity for ELF/VLF wave generation involves the mixing of HF oscillations of the plasma with the high power radio waves. In the numerical simulations presented here, ω_1 is set to 2.740 MHz and ω_2 is 5.510 MHz. With these frequency choices, the expected VLF wave generation frequency, $|\omega_2 - 2\omega_1|$, is 30 kHz, the dominant collision frequency oscillation suggested by *Gurevich* [1978] and *Kotik and Ermakova* [1998], $2\omega_1$, is 5.48 MHz, and the dominant collision frequency oscillation suggested by *Moore et al.* [2013], $|\omega_2 - \omega_1|$, is 2.77 MHz. This FDTD model includes the core physics to distinguish which frequency content dominates the interaction.

The simulation space used here is the same as that used in the HF cross modulation simulations: 3 m grid-size, 10 ns time-step, vertical magnetic field, ionospheric plasma between 50 and 100 km, injection source at 45 km, and an absorbing boundary conditions on both ends of the grid. The simulation was run for 7.5 ms which is 225 periods at 30 kHz. It is noted though that the HF phasing effects present when splitting HAARP in a North/South versus East/West configuration are not included [*Moore et al.*, 2013].

The electric field, collision frequency, and plasma current density were all recorded every iteration at 80 km altitude and the frequency spectrum of these can be seen in Figure 3-14. The ionosphere was allowed to reach steady-state which was shown in Section 3.2.1 to be less than 1 ms and values of the electric field, collision frequency, and plasma current density after 1.5 ms into the simulation were used in these plots. These values were windowed with a Kaiser window with beta equal to 32 in order to reduce the noise floor. The FFT was then taken.

The top left plot in Figure 3-14 shows the spectrum of the electric field. Strong peaks of -18.7 dB and -18.0 dB are seen at 2.74 MHz and 5.51 MHz, as expected because these are the source frequencies, ω_1 and ω_2. The next strongest peak is at 30 kHz with a magnitude of -98.4 dB, or 80 dB lower than the source frequencies. An enlargement of the electric field spectrum between DC and 100 kHz is shown in the top right plot. The 30 kHz peak is clearly shown to be about 200 dB above the numerical noise floor. The next strongest peak in the electric field is at 8.28 MHz at -105.2 dB which is close to 90 dB lower than the source peaks and 7 dB lower than the 30 kHz peak. The 8.28 MHz peak is equal to $|2\omega_2 - \omega_1|$ and is created by collision frequency oscillations at $|\omega_2 - \omega_1|$, 2.77 MHz, mixing with the plasma current density at ω_2, 5.51 MHz. The 8.28 MHz peak is also created by a collision frequency oscillation at $2|\omega_2 - \omega_1|$, 5.54 MHz, mixing with the plasma current density at ω_1, 2.74 MHz. This scenario most likely creates a weaker electric field than the first due to the weaker oscillation of the collision frequency at $2|\omega_2 - \omega_1|$ versus $|\omega_2 - \omega_1|$. The last peak identified in the electric field plot is at 2.8 MHz with a magnitude of -167.9 dB or nearly 150 dB lower than the source

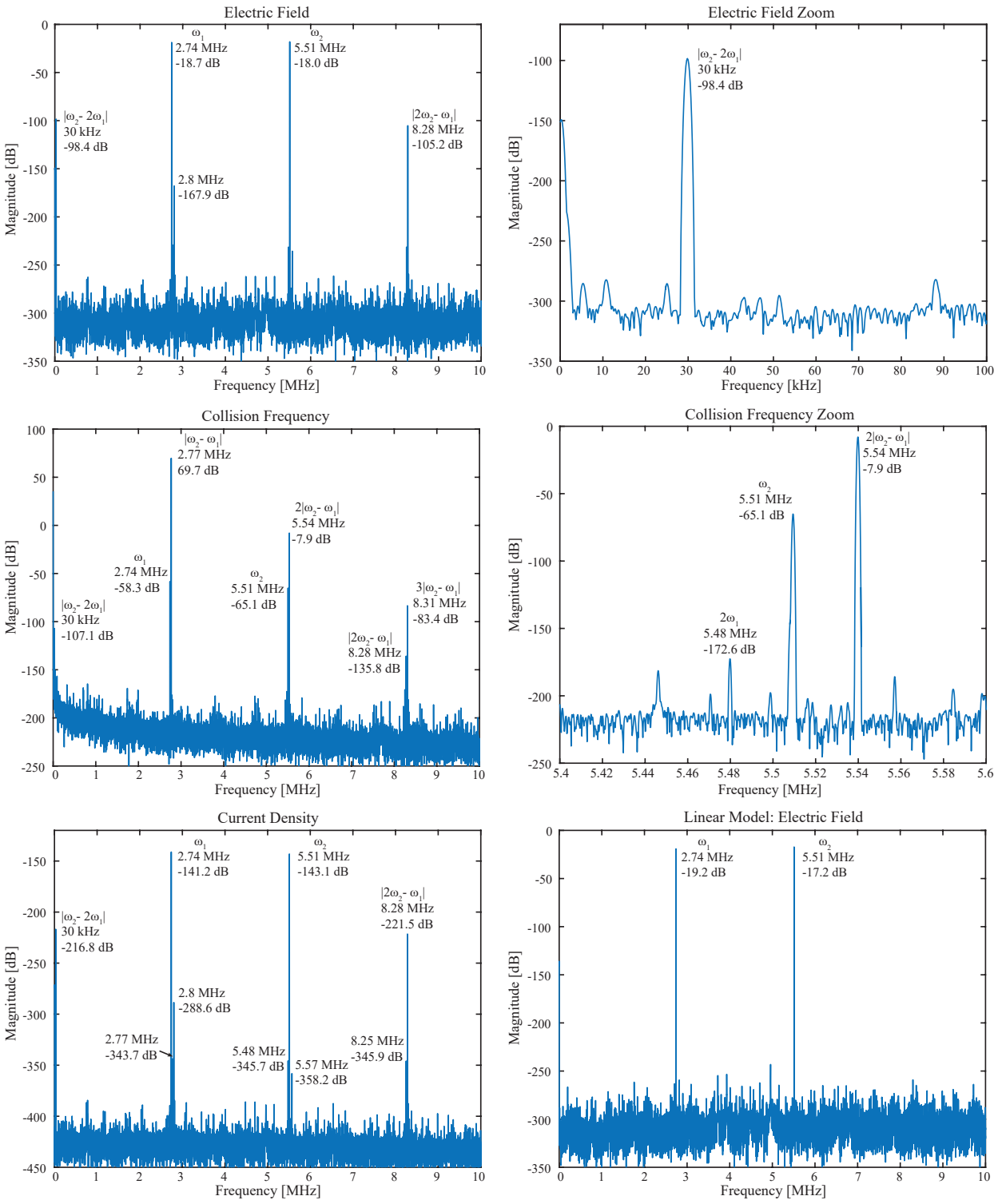

Figure 3-14. (top left) Electric field oscillations showing strong peaks at ω_1, ω_2, and the VLF generated frequency, 30 kHz, (top right) an enlargement of the electric field oscillations clearly showing the 30 kHz peak, (middle left) collision frequency oscillations showing a dominant peak at $|\omega_2 - \omega_1|$, (middle right) an enlargement of the collision frequency oscillations showing the peak at $2\omega_1$ is significantly low, (bottom left) current density oscillations showing strong peaks at ω_1 and ω_2, (bottom right) electric field oscillations from a linear model showing no oscillations at 30 kHz.

frequencies and 70 dB lower at than 30 kHz. The 2.8 MHz peak is a product of the collision frequency oscillation at $|\omega_2 - \omega_1|$, 2.77 MHz, mixing with the plasma current density at 30 kHz.

The middle left plot of Figure 3-14 shows the collision frequency spectrum. The strongest peak is at $|\omega_2 - \omega_1|$, 2.77 MHz, with a magnitude of 69.7 dB. This is the collision frequency peak that *Moore et al.* [2013] determined to be the most strongly involved in the thermal cubic nonlinearity, and the creation of the 30 kHz peak here. The next strongest peak is at $2|\omega_2 - \omega_1|$, 5.54 MHz, with a magnitude of -7.9 dB, or close to 80 dB lower than the peak at $|\omega_2 - \omega_1|$. As mentioned above, this peak also plays a role in the creation of 8.28 MHz electric field oscillations, but because it is 80 dB lower than the other collision frequency source, it is expected to play a substantially smaller role.

The middle right panel shows an enlargement of collision frequency oscillations between 5.4 MHz and 5.6 MHz. In this plot it can be seen that collision frequency oscillations at ω_2 are 60 dB lower than at $2|\omega_2 - \omega_1|$. Also, it can be seen that collision frequency oscillations at $2\omega_1$, 5.48 MHz, the peak suggested by *Gurevich* [1978] and *Kotik and Ermakova* [1998] to be the primary source of the thermal cubic nonlinearity, has a magnitude of -172.6 dB. This is 242.3 dB lower than the peak at $|\omega_2 - \omega_1|$, the peak determined by *Moore et al.* [2013]. It is therefore concluded in this work, in agreement with *Moore et al.* [2013], that the primary mechanism behind the thermal cubic nonlinearity is collision frequency oscillations at $|\omega_2 - \omega_1|$ mixing with plasma current density oscillations at ω_1. This conclusion applies only for the case of a vertical magnetic field, however, as discussed by *Moore et al.* [2013].

The bottom left plot of 3-14 shows the plasma current density spectrum. The strongest peaks are, as expected, at the source frequencies, ω_1 and ω_2, with magnitudes of -141.2 dB and -143.1 dB, which is within 2 dB of each other. The next strongest peaks are at 30 kHz and 8.28 MHz with magnitudes of -216.8 dB and -221.5 dB, respectively. These are about 80 dB lower than the the source frequency peaks. Numerous other peaks 140 dB to 200 dB lower than the peaks at ω_1 and ω_2 are identified in the plot.

The bottom right plot of 3-14 shows the electric field of a linear FDTD simulation of thermal cubic nonlinearity. The strong peaks at ω_1 and ω_2 are still present, as expected, because these are the input source frequencies. There are no peaks observed at 30 kHz, 8.28 MHz, or 2.8 MHz, because this is a linear model and those frequencies are caused by nonlinear interactions. This is further verification of the nonlinear HF heating FDTD model proving that the peaks seen in the nonlinear model are caused by nonlinear interactions in the simulated ionosphere.

Lastly, we note that the electric field value shown in the top-right panel of Figure 3-14 corresponds to ~30 dB fT, a value that is on the correct order of magnitude when compared with observations presented near HAARP by *Moore et al.* [2013].

3.4.2 Generated Frequency Dependence

The amplitude of the ELF/VLF generated wave using the thermal cubic nonlinearity is investigated here. Eleven simulations were run, varying the source frequency of ω_1, so that the generated ELF/VLF frequency ranged from 1 kHz to 35 kHz in steps of 1 kHz up to 5 kHz and steps of 5 kHz up to 35 kHz. The source frequencies for ω_1 were: 2.7545 MHz, 2.7540 MHz, 2.7535 MHz, 2.7530 MHz, 2.7525 MHz, 2.7500 MHz, 2.7475 MHz, 2.7450 MHz, 2.7425 MHz, 2.7400 MHz, and 2.7375 MHz. ω_2 remained constant at 5.51 MHz.

The electric field of each simulation was recorded every iteration at 46 km. Similar to above, the simulations were run for 7.5 ms and the first 1.5 ms were discarded. The electric field was then windowed using a kaiser window and the FFT was taken. The magnitude of the eleven generated ELF/VLF waves are shown in Figure 3-15. An altitude of 46 km was chosen in order to more accurately represent the amplitude of the wave injected into the earth-ionosphere waveguide. This can be seen to be significant when comparing the peak at 30 kHz which is 17.6 dB lower at 46 km (-116 dB) than it was at 80 km (-98.4 dB) as seen in Figure 3-14.

The thermal cubic nonlinearity produces stronger magnitude VLF waves at lower frequencies until a peak is reached near 5 kHz. The largest magnitude frequency produced

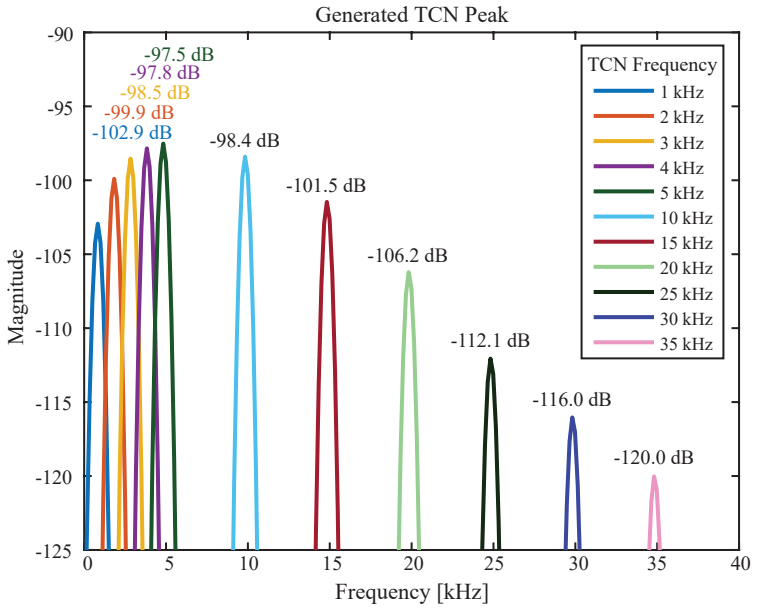

Figure 3-15. VLF generated frequencies using the thermal cubic nonlinearity recorded at 46 km altitude. The amplitude of the generated wave is seen to decrease with increasing frequency.

in these simulations was at 5 kHz with a magnitude of -97.5 dB. The magnitude below 5 kHz slowly decreases down to a minimum at 1 kHz (-102.9 dB) but this is only 5 dB lower than the peak at 5 kHz. There is a much more substantial decrease in peak magnitude when increasing in frequency. The magnitude at 5 kHz of -97.5 dB is 22.5 dB stronger than the magnitude at 35 kHz (-120.0 dB). It is also noted that between 5 kHz and 15 kHz that the magnitude decreases slowly. The peak at 15 kHz (-101.5 dB) is actually larger than the peak at 1 kHz (-102.9 dB). Beyond 15 kHz, the magnitude drops by 4 dB to 6 dB every 5 kHz. From these simulations and utilizing these ambient profiles, it is seen that the thermal cubic nonlinearity is optimal to use below 15 kHz.

These simulation results seem to disagree with observations by *Moore et al.* [2013], where the ELF/VLF observations near 5 kHz were not as detectable as those near 20 kHz. This effect may result from propagation effects similar to "beat-wave" heating, where the spatial offset of the HAARP sub-arrays produces a phasing effect in the sky [e.g., *Moore et al.*, 2012; *Cohen*

et al., 2012b] that results in a strong dependence on modulation frequency observed on the ground benefiting the higher frequencies.

The nonlinear HF heating FDTD model developed in this chapter implemented the 1^{st}- and 2^{nd}-order moments of the Boltzmann equation derived neglecting the convective derivative to simulate cross-modulation and thermal cubic nonlinearity experiments. Additional terms are present in both the 1^{st}- and 2^{nd}-order moments when accounting for the convective derivative and these terms are investigated for VLF heating in Chapter 4.

CHAPTER 4
PLASMA FDTD INCLUDING CONVECTION AND CONDUCTION

Previous simulations presented in this dissertation have utilized versions of the 1^{st}- and 2^{nd}-order moments of the Boltzmann equation that neglect convection and heat conduction. In this chapter, the 1^{st}- and 2^{nd}-order moments of the Boltzmann equation are derived accounting for convection and conduction. Using a 3-D nonlinear VLF heating model, each convective and conductive term in the 1^{st}- and 2^{nd}-order moments of the Boltzmann equation is analyzed to determine its importance to ionospheric heating. Particular attention is focused on the form of Joule heating in the 2^{nd}-order moment and the impact of the form on HF heating during cross-modulation simulations

4.1 Moments of the Boltzmann Equation

Kinetic theory tracks the number density of particles with a velocity $\vec{v}$ in space and time through the velocity distribution function, $f(\vec{r},\vec{v},t)$. Each species, denoted by a subscript s, is tracked through an individual velocity distribution function, $f_s(\vec{r},\vec{v},t)$. For the simulations presented in this work, only electrons are tracked, and the subscript s is dropped. The velocity distribution function depends on seven variables: time (t), three spatial coordinates (x, y, z), and three velocity components (v_x, v_y, v_z). The Boltzmann Equation (Eq. 4-1) describes the dynamic response of each plasma species to to an external force [*Uman*, 1964, p. 34, *Bittencourt*, 2004, p. 195].

$$\frac{\partial}{\partial t}f(\vec{r},\vec{v},t) = -\left(\vec{v}\cdot\nabla\right)f(\vec{r},\vec{v},t) - \left[\left(\frac{\vec{F}}{m}\right)\cdot\nabla_v\right]f(\vec{r},\vec{v},t) + \left.\frac{\partial f(\vec{r},\vec{v},t)}{\partial t}\right|_{coll} \tag{4-1}$$

where:

$$\vec{r} = x\hat{\mathbf{x}} + y\hat{\mathbf{y}} + z\hat{\mathbf{z}} \tag{4-2}$$

$$\vec{v} = v_x\hat{\mathbf{x}} + v_y\hat{\mathbf{y}} + v_z\hat{\mathbf{z}} \tag{4-3}$$

$$\nabla = \frac{\partial}{\partial x}\hat{\mathbf{x}} + \frac{\partial}{\partial y}\hat{\mathbf{y}} + \frac{\partial}{\partial z}\hat{\mathbf{z}} \tag{4-4}$$

$$\nabla_v = \frac{\partial}{\partial v_x}\hat{\mathbf{x}} + \frac{\partial}{\partial v_y}\hat{\mathbf{y}} + \frac{\partial}{\partial v_z}\hat{\mathbf{z}} \tag{4-5}$$

The first term on the right describes the change in number density of particles with velocity $\vec{v}$ entering or exiting the differential volume. It is known as the convective derivative, and it is sometimes neglected. The second term on the right describes the change in number density of particles with velocity $\vec{v}$ due to the external force acting on them and only includes particles already inside the differential volume. The final term on the right describes the collisional effects of the plasma, including changes to species number density through chemical reactions, and changes in species velocity by collisions with neutral particles, for instance.

Solving the Boltzmann equation over all space allows the calculation of the plasma current density for the particular species. The total plasma current density can then be coupled with Maxwell's Equations in order to solve for wave propagation. This process is then repeated throughout time. This is an unmanageable process for the grid size and required time steps of this case, and it is more practical to solve for the moments of the Boltzmann Equation.

Moments of the Boltzmann Equation are derived by multiplying the Boltzmann Equation by the desired property and integrating over velocity. The 0^{th}-, 1^{st}-, and 2^{nd}-order moments presented here are so named because they require the n^{th} power of velocity.

The 0^{th}-order moment of the Boltzmann Equation results in the continuity equation [*Bittencourt*, 2004, p. 197]:

$$\frac{\partial \rho_m}{\partial t} + \nabla \cdot \rho_m \vec{u} = S \tag{4-6}$$

where ρ_m represents the mass density, $\vec{u}$ is the average velocity, and $S = \frac{\delta \rho_m}{\delta t}|_{coll}$ which represents the rate per unit volume that particles are produced or lost as a result of collisions. In the absence of interactions creating production or loss of particles, $S = 0$. When one sums over all species, the sum of $S = 0$, because matter cannot be created or destroyed. Multiplying Eq. 4-6 by the particle charge and dividing by the particle mass leads to the charge continuity equation [*Bittencourt*, 2004, p. 198]:

$$\frac{\partial \rho}{\partial t} = -\nabla \cdot \vec{J}. \tag{4-7}$$

where ρ is charge density and $\vec{J}$ is charge current density. It is noted that $n = \frac{\rho_m}{m}$, $\rho = nq$, and $\vec{J} = \rho\vec{u}$ where n is the species number density, m is the species mass, and q is the species charge. Similarly, Eq. 4-7 has been summed over all species so that the collisional effects sum to zero.

The 1^{st}-order moment of the Boltzmann Equation results in the momentum transfer equation [*Bittencourt*, 2004, p. 202]:

$$\rho_m \frac{D\vec{u}}{Dt} = nq\left(\vec{E} + \vec{u} \times \vec{B}\right) + \rho_m \vec{g} - \nabla \cdot P + \vec{A} - \vec{u}S \tag{4-8}$$

where $\frac{D}{Dt} = \frac{\partial}{\partial t} + \vec{u} \cdot \nabla$ is the total time derivative operator corresponding to the time variation observed in a reference frame moving with the mean velocity $\vec{u}$ which includes the convective derivative, $\vec{g}$ is the acceleration of gravity, P accounts for the pressure forces including viscosity, and $\vec{A} = \frac{\delta(\rho_m \vec{u})}{\delta t}|_{coll}$. Due to the large number of collisions in the D-region ionosphere, it is a good approximation that the off-diagonal, viscosity terms of P are relatively unimportant and the pressure term is isotropic. The pressure term may be approximated as $P = N_e \kappa_B T_e$. Multiplying by the electron charge and dividing by the electron mass, the 1^{st}-order moment may be restated as:

$$\begin{aligned}\frac{\partial}{\partial t}\vec{J} = \frac{q_e^2 N_e}{m_e}\vec{E} + \frac{q_e \mu_0}{m_e}\vec{J} \times \vec{H} + q_e N_e \vec{g} - \nu\vec{J} - \frac{q_e N_e \kappa_B}{m_e}\nabla T_e - \frac{q_e \kappa_B T_e}{m_e}\nabla N_e \\ -\frac{\vec{J}}{q_e N_e}\left(\nabla \cdot \vec{J}\right) - \frac{1}{q_e N_e}\left(\vec{J} \cdot \nabla\right)\vec{J} + \frac{\vec{J}}{q_e N_e^2}\left(\vec{J} \cdot \nabla N_e\right)\end{aligned} \tag{4-9}$$

where $\vec{J}$ is the plasma current density, q_e, N_e, m_e, and T_e are the electron charge, density, mass, and temperature, $\vec{H}$ is the total magnetic field including the wave and background field, and ν is the effective collision frequency.

To better understand the derivation from Eq. 4-8 to Eq. 4-9, the source of each term in Eq. 4-9 will be explained. The four terms of $\frac{\partial \vec{J}}{\partial t}$, $-\frac{\vec{J}}{q_e N_e}\left(\nabla \cdot \vec{J}\right)$, $-\frac{1}{q_e N_e}\left(\vec{J} \cdot \nabla\right)\vec{J}$, and $+\frac{\vec{J}}{q_e N_e^2}\left(\vec{J} \cdot \nabla N_e\right)$ result from the total time derivative operator, $\rho_m \frac{D\vec{u}}{Dt}$, with the last three terms explicitly from the convective derivative, $\vec{u} \cdot \nabla$. The two terms, $\frac{q_e^2 N_e}{m_e}\vec{E}$ and $\frac{q_e \mu_0}{m_e}\vec{J} \times \vec{H}$, are from the Lorentz force, $nq\left(\vec{E} + \vec{u} \times \vec{B}\right)$. The gravity term, $q_e N_e \vec{g}$, is readily apparent from $\rho_m \vec{g}$. There are two pressure terms, $-\frac{q_e N_e \kappa_B}{m_e}\nabla T_e$ and $-\frac{q_e \kappa_B T_e}{m_e}\nabla N_e$, that result from $-\nabla \cdot P$. The final term to mention is $-\nu\vec{J}$ which results from $-\vec{u}S$. The definitions of Term # as shown in Eqs. 4-10 to 4-16 are used throughout this chapter.

$$\text{Term } 1 = \frac{q_e \mu_0}{m_e}\vec{J} \times \vec{H}_w \tag{4-10}$$

$$\text{Term } 2 = -\frac{q_e N_e \kappa_B}{m_e}\nabla T_e \tag{4-11}$$

$$\text{Term } 3 = -\frac{q_e T_e \kappa_B}{m_e}\nabla N_e \tag{4-12}$$

$$\text{Term } 4 = -\frac{\vec{J}}{q_e N_e}\left(\nabla \cdot \vec{J}\right) \tag{4-13}$$

$$\text{Term } 5 = -\frac{1}{q_e N_e}\left(\vec{J} \cdot \nabla\right)\vec{J} \tag{4-14}$$

$$\text{Term } 6 = \frac{\vec{J}}{q_e N_e^2}\left(\vec{J} \cdot \nabla N_e\right) \tag{4-15}$$

$$\text{Term } 7 = q_e N_e \vec{g} \tag{4-16}$$

It is readily seen that if the convective derivative is neglected, pressure is neglected, the wave magnetic field interaction is neglected, and the force of gravity is neglected, we obtain the 1^{st}-order moment used in Chapter 3:

$$\frac{\partial}{\partial t}\vec{J} = \frac{q_e^2 N_e}{m_e}\vec{E} + \frac{q_e \mu_0}{m_e}\vec{J} \times \vec{H}_0 - \nu\vec{J}. \tag{4-17}$$

The 2^{nd}-order moment of the Boltzmann Equation is the energy transport equation [*Bittencourt*, 2004, p. 206]:

$$\frac{D}{Dt}\left(\frac{3p}{2}\right) + \frac{3p}{2}\nabla \cdot \vec{u} + (P \cdot \nabla) \cdot \vec{u} + \nabla \cdot \vec{q} = M - \vec{u} \cdot \vec{A} + \frac{1}{2}u^2 S \tag{4-18}$$

where p is the isotropic pressure, M is an energy loss rate representing the rate of energy density changes due to collisions, and $\vec{q}$ is the heat flux vector. The 2^{nd}-order moment can be written in terms of electron temperature:

$$\begin{aligned} \frac{3}{2}N_e\kappa_B\frac{\partial T_e}{\partial t} = \frac{\nu m_e}{q_e^2 N_e}\left(\vec{J}\cdot\vec{J}\right) - \frac{3\kappa_B}{2q_e}\left(\vec{J}\cdot\nabla T_e\right) + \frac{\kappa_B T_e}{q_e N_e}\left(\vec{J}\cdot\nabla N_e\right) + \\ \frac{m_e}{2q_e^2 N_e^2}\left(\vec{J}\cdot\vec{J}\right)\left.\frac{\partial N_e}{\partial t}\right|_{coll} - \frac{3}{2}\kappa_B T_e\left.\frac{\partial N_e}{\partial t}\right|_{coll} - \frac{\kappa_B T_e}{q_e}\left(\nabla\cdot\vec{J}\right) - \nabla\cdot\vec{q} - L(N_e, T_e, T_N) \end{aligned} \tag{4-19}$$

where $\vec{q}$ is thermal heat flow, or conduction, and is approximated as [*Bittencourt*, 2004]:

$$\vec{q} = \frac{N_e \kappa_B^2 T_e}{m_e \nu}\nabla T_e. \tag{4-20}$$

Eq. 4-19 is the 2^{nd}-order moment of the Boltzmann Equation including convection and conduction. In the D-region ionosphere, the pressure terms are considered isotropic and $\vec{q}$ (Eq. 4-20) which represents thermal heat flow, or conduction, within the plasma is approximated.

Each term in Eq. 4-19 is now correlated to a term in Eq. 4-18 to better understand the derivation. The two terms, $\frac{3}{2}N_e\kappa_B\frac{\partial T_e}{\partial t}$ and $\frac{\nu m_e}{q_e^2 N_e}\left(\vec{J}\cdot\vec{J}\right)$, result from the total time derivative operator term, $\frac{D}{Dt}\left(\frac{3p}{2}\right)$. The two terms, $-\frac{3\kappa_B}{2q_e}\left(\vec{J}\cdot\nabla T_e\right)$ and $+\frac{\kappa_B T_e}{q_e N_e}\left(\vec{J}\cdot\nabla N_e\right)$, result from $+(P\cdot\nabla)\cdot\vec{u}$. The two terms, $+\frac{m_e}{2q_e^2 N_e^2}\left(\vec{J}\cdot\vec{J}\right)\left.\frac{\partial N_e}{\partial t}\right|_{coll}$ and $-\frac{3}{2}\kappa_B T_e\left.\frac{\partial N_e}{\partial t}\right|_{coll}$, result from $+\frac{1}{2}u^2 S$. The term $-\frac{\kappa_B T_e}{q_e}\left(\nabla\cdot\vec{J}\right)$ results from $+\frac{3p}{2}\nabla\cdot\vec{u}$. The $\nabla\cdot\vec{q}$ term remains the same. The loss rates, $L(N_e, T_e, T_N)$, are from M.

If one neglects convection and heat conduction, the 2^{nd}-order moment reduces to:

$$\frac{3}{2}N_e\kappa_B\frac{\partial T_e}{\partial t} = \frac{\nu m_e}{q_e^2 N_e}\vec{J}\cdot\vec{J} - \frac{3}{2}\kappa_B T_e\frac{\partial N_e}{\partial t} - L(N_e, T_e, T_n) \tag{4-21}$$

The first term on the right, the Joule heating term, is different than the version of the 2^{nd}-order moment used in the nonlinear HF heating model in Chapter 3. If one approximates that $\vec{J} = \sigma_{||}\vec{E}$, which is true in the isotropic case, then the following relationship holds:

$$\frac{\nu m_e}{q_e^2 N_e}(\vec{J}\cdot\vec{J}) = \vec{J}\cdot\vec{E}. \tag{4-22}$$

The equality of these two terms is valid even in the anisotropic case when the collision frequency is much greater than the wave frequency. With this assumption, the 2^{nd}-order moment is:

$$\frac{3}{2}N_e\kappa_B\frac{\partial T_e}{\partial t} = \vec{J}\cdot\vec{E} - \frac{3}{2}\kappa_B T_e\frac{\partial N_e}{\partial t} - L(N_e, T_e, T_n) \tag{4-23}$$

which is the version used in Chapter 3 of this work, and in many other works [e.g., *Huxley and Ratcliffe*, 1949; *Stubbe and Kopka*, 1977; *Tomko et al.*, 1980; *Rietveld et al.*, 1989; *Rodriguez*, 1994; *Moore*, 2007; *Moore and Agrawal*, 2011; *Marshall*, 2014].

4.2 VLF Heating

To evaluate the relative importance of each term in the 1^{st}- and 2^{nd}-order moments of the Boltzmann Equation, a 3-D nonlinear FDTD model was created. This model is similar to the HF heating model presented in Chapter 3 in that they both allow for a temporally- and spatially-varying electron temperature, electron density, and electron-neutral collision frequency. The main differences between the models are that this model simulates 3-D propagation, and implements the 1^{st}- and 2^{nd}-order moments of the Boltzmann Equation including convection and conduction. The 1-D model of Chapter 3 utilized small grid cells and small time steps to simulate HF propagation. The 3-D version is limited in spatial step size and time step size for run-time considerations. We therefore limit the frequency to the VLF range. The spatial step in the 3-D model here is to 500 m, which provides 25 grid-cells per wavelength at 24 kHz. The simulation space is 150 km x 150 km x 100 km vertical. The stability factor is maintained at the same limit as a traditional 3-D FDTD free-space implementation, $1/\sqrt{3}$.

A broadside VLF source centered in the xy-plane at 30 km altitude is used in this work instead of a vertical monopole at ground level to represent a Navy VLF transmitter. The VLF source used here was chosen mainly to limit the required grid dimensions as the broadside VLF source radiates vertically. A vertical monopole radiates in more of a doughnut pattern with little power directly above the source. This would require a much larger grid in order to analyze the VLF heating effects on the ionosphere. For the purpose of analyzing the effects of the 1^{st}- and 2^{nd}-order moments from VLF heating, the broadside VLF source was deemed reasonable.

This model utilizes a more complicated 13-step update loop.

1. Update $\vec{D}_{\text{eff}}$ using $\vec{H}$: Eq. 1-1
2. Update $\vec{E}$ using $\vec{D}_{\text{eff}}$: Linear Method 2
3. Calculate $\vec{J}$ using $\vec{D}_{\text{eff}}$ and $\vec{E}$: Eq. 3-20
4. Update T_e: Eq. 4-19
5. Calculate ν_{av} using T_e: Eqs. 3-16 to 3-18
6. Calculate ν_{eff} using ν_{av}: Eq. 3-19
7. Update N_e using the chemistry model: Eqs. 3-12 to 3-15
8. Calculate the six additional terms in the 1^{st}-order moment: Eqs. 4-10 to 4-15
9. Add the six additional terms to the plasma current density
10. Recalculate $\vec{E}$ using the plasma current density
11. Recalculate T_e, ν_{av}, ν_{eff}, and N_e: Repeat Steps 4 to 7
12. Calculate new update coefficients for step 2
13. Update $\vec{H}$ using $\vec{E}$: Eq. 1-2

Steps 1 through 7 in the VLF heating model are the same as the HF heating model in Chapter 3. In Step 3, the plasma current density is calculated, but this plasma current density is the simplified version of Eq. 4-17. Steps 8 and 9 are necessary to update the plasma current density with the additional terms present in the 1^{st}-order moment, Eq. 4-9. To factor the plasma current density with all terms included into the wave propagation, the electric

field is recalculated in Step 10. The 2^{nd}-order moment (Eq. 4-19) is implemented directly when updating the electron temperature and no additional steps are required to include the additional terms in this moment of the Boltzmann Equation.

4.2.1 First-Order Moment

The 1^{st}-order moment of the Boltzmann Equation was presented in Eq. 4-9. There are 7 terms (Eqs. 4-10 to 4-16) that were assumed to be negligible in the form of the 1^{st}-order moment presented in Eq. 4-17 that was used in Chapters 2 and 3. In the absence of an external field, the plasma current density is zero. To numerically simulate this, the vertical, ambient components of Term 2 (Eq. 4-11) and Term 3 (Eq. 4-12) are set equal and opposite to the vertical component of Term 7 (Eq. 4-16):

$$q_e N_{e,0} g_z \hat{\mathrm{z}} = +\frac{q_e N_e \kappa_B}{m_e}\frac{\partial T_{e,0}}{\partial z}\hat{\mathrm{z}} + \frac{q_e T_e \kappa_B}{m_e}\frac{\partial N_{e,0}}{\partial z}\hat{\mathrm{z}} \equiv \vec{V} \tag{4-24}$$

where g_z is the vertical acceleration due to gravity, $T_{e,0}$ is the ambient electron temperature, $N_{e,0}$ is the ambient electron density, and $\vec{V}$ is defined as the ambient balance term. Physically this represents that the force of gravity is balanced out by the internal pressure of the plasma due to the vertical ambient temperature and ambient electron density gradients. The 1^{st}-order moment including the ambient balance term is:

$$\begin{aligned}\frac{\partial}{\partial t}\vec{J} = \frac{q_e^2 N_e}{m}\vec{E} + \frac{q_e \mu_0}{m_e}\vec{J}\times\vec{H} - \nu\vec{J} - \frac{q_e N_e \kappa_B}{m_e}\nabla T_e - \frac{q_e \kappa_B T_e}{m}\nabla N_e \\ -\frac{\vec{J}}{q_e N_e}\left(\nabla\cdot\vec{J}\right) - \frac{1}{q_e N_e}\left(\vec{J}\cdot\nabla\right)\vec{J} + \frac{\vec{J}}{q_e N_e^2}\left(\vec{J}\cdot\nabla N_e\right) + \vec{V}.\end{aligned} \tag{4-25}$$

In the simulations shown here, Terms 1 to 6 are calculated individually and added to the total plasma current density every iteration. This allows us to save each term separately to compare the relative magnitude of each term.

The impact on the plasma current density for Terms 1 through 6 is shown in Figure 4-1 for the $\hat{\mathrm{x}}$-component, and Figure 4-3 for the $\hat{\mathrm{z}}$-component. For these figures, the VLF heating simulation utilized the 1^{st}- and 2^{nd}-order moments, as shown in Eqs. 4-9 and 4-19. The plots

labeled 'Difference' in Figures 4-1 and 4-3 calculate the difference in the plasma current density between simulations using the 1^{st}-order moment, Eq. 4-9, and the simplified 1^{st}-order moment, Eq. 4-17. All of the figures were created from the same iteration of the FDTD simulation, capturing these components and additional terms at one instant in time.

Figure 4-1 shows the $\hat{\mathrm{x}}$-components of the plasma current density, and the top left panel shows the J_x component of the plasma current density calculated using Eq. 4-9. The strongest region of the plasma current density is directly above the source in the 80 km to 85 km region with a peak magnitude around 4×10^{-7} $\mathrm{A/m^3}$. In this plot and the other panels, there is a plasma current density present below 75 km, but it is orders of magnitude smaller and unable to be resolved well in the color scheme shown. The absolute value of the plasma current density is plotted in logarithmic scale in Figure 4-2. The left panel shows J_x and the right panel shows J_z. Below 75 km, the plasma current density decreases in magnitude rapidly. The plasma current density at 60 km altitude is 5 orders of magnitude smaller than at 78 km. It is difficult to resolve this range in the linear color scheme shown in Figures 4-1 and 4-3 so the color scale is set to best show the plasma current density above 75 km altitude.

The top right panel of Figure 4-1 shows the difference in J_x between two simulations, one utilizing Eq. 4-9 and the other using the simplified version, Eq. 4-17. Both simulations utilize the 2^{nd}-order moment, Eq. 4-19. This difference shows how the additional terms in Eq. 4-9 accumulate and affect the plasma current density. It can be seen that the difference between the simulations is two orders of magnitude less than the peak plasma current density shown in the top left panel.

The Term 1 plot has the largest peak magnitude of any of the additional terms with a peak of 1.5×10^{-11} $\mathrm{A/m^3}$ at around 80 km altitude. This term is a product of the plasma current density and wave magnetic field, two field values expected to be oscillating at the source frequency. It appears that the spatial frequency of Term 1 is twice that of the plasma current density shown in the top left plot. This means that Term 1 is predominantly varying spatially at twice the source frequency, 48 kHz. This term is opposite in sign, or odd, across

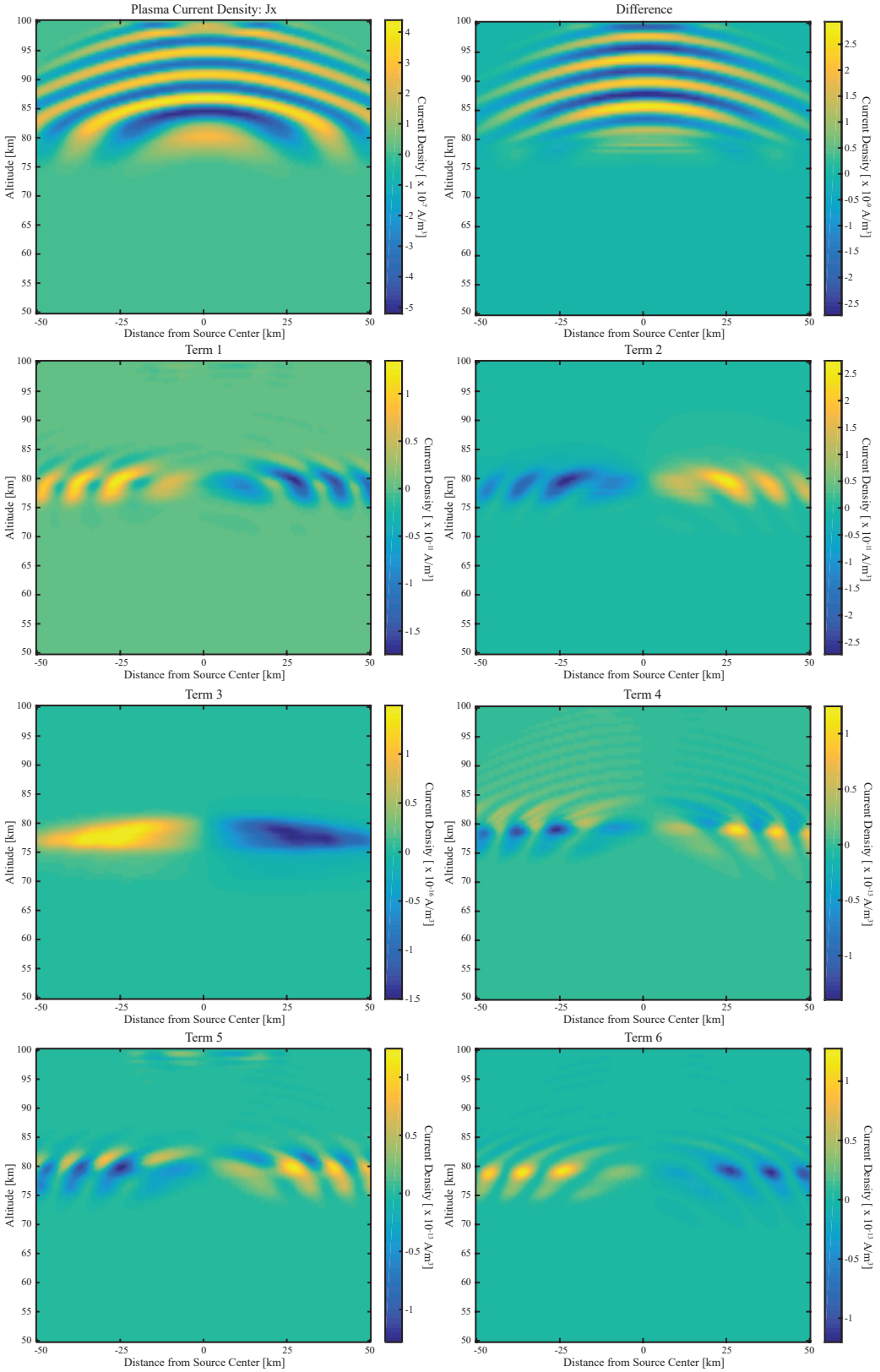

Figure 4-1. $\hat{\mathrm{x}}$-components of the additional terms in Eq. 4-9 for 24 kHz VLF heating simulation using Eq. 4-19.

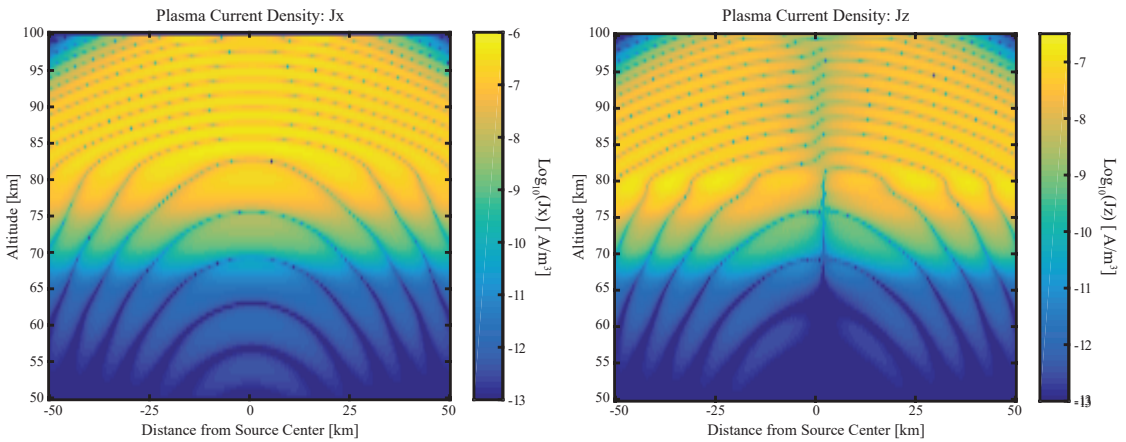

Figure 4-2. Absolute value of the plasma current density using Eq. 4-9 in logarithmic scale (left) J_x (right) J_z .

the source center. The explicit evaluation of Term 1 is $\hat{\mathrm{x}}\frac{q_e\mu_0}{m_e}\left(J_yH_z - J_zH_y\right)$ where J_y and H_y are even across the source center and J_z and H_z are odd across the source center. This results in even field values multiplied by odd field values causing Term 1 to be odd, as well.

Terms 2 and 3 are similar to Term 1 in that the region of strongest intensity is between 75 km to 85 km with a much weaker strength outside of this region. Term 2 has a peak magnitude of $2.5 \times 10^{-12}\ \mathrm{A/m^3}$ and Term 3 is significantly weaker with a peak magnitude of $1.5 \times 10^{-16}\ \mathrm{A/m^3}$. The electron temperature heats and cools on the order of the VLF wavelength causing large temperature gradients, as seen from the strength of Term 2. Conversely, the electron density changes much more slowly so the electron density gradient in Term 3 is much smaller. Term 2 also appears to be varying spatially at twice the source frequency whereas Term 3 appears to be DC in nature. Similar to Term 1, Terms 2 and 3 appear odd across the source center. In this simulation, electron temperature heating is strongest directly above the source and decreases radially away. The electron density change is also strongest directly above the source and decreases in value radially outward. Therefore, both the electron temperature and electron density are even functions across the source center. Terms 2 and 3 take the gradient of these plasma parameters. The gradient of an even function is an odd function resulting in Terms 2 and 3 being odd across the source center.

Terms 4, 5, and 6 all have peak magnitudes of around $1 \times 10^{-13}\ \mathrm{A/m^3}$ which is 6 orders of magnitude less than the peak plasma current density and 2 orders of magnitude less than the peak strength of Term 1. Similar to the previous terms, Terms 4, 5, and 6 are strongest in the region between 75 km to 85 km. Also, Terms 4, 5, and 6 all involve a product of $\vec{J}$ mixing with another $\vec{J}$ which causes them all to appear to be spatially varying at twice the source frequency. Like the previous three terms, Terms 4, 5, and 6 appear odd across the source center. This is because the plasma current density is even and the divergence of the plasma current density results in these terms being odd.

The $\hat{\mathrm{y}}$-components of the plasma current density produce similar results to the $\hat{\mathrm{x}}$-components so we progress to the $\hat{\mathrm{z}}$-components now.

Figure 4-3 shows the $\hat{\mathrm{z}}$-components of the plasma current density and the top left panel shows the J_z component of the plasma current density calculated using Eq. 4-9. Unlike the $\hat{\mathrm{x}}$- and $\hat{\mathrm{y}}$-components, the strongest region of J_z does not occur directly over the source. Instead the strongest region is offset 30 km horizontally from the source center and is located at an altitude of 80 km. J_z has a peak magnitude of $1.5 \times 10^{-7}\ \mathrm{A/m^3}$ which is on the same order of magnitude as J_x. J_z is odd across the source center due to the vertical magnetic field.

The top right panel of Figure 4-3 shows the difference in J_z between two simulations, one utilizing Eq. 4-9 and the other using the simplified version, Eq. 4-17. The peak difference between these two simulations is $6 \times 10^{-10}\ \mathrm{A/m^3}$ which is about three orders of magnitude less than the peak plasma current density seen in the top left panel. The difference is seen to be odd across the source center again due to the vertical magnetic field.

Term 1 was the strongest additional term for the $\hat{\mathrm{x}}$-component of the plasma current density and for the $\hat{\mathrm{z}}$-component, it is nearly the strongest with a peak field strength of $1.2 \times 10^{-10}\ \mathrm{A/m^3}$. Term 1 varies spatially at twice the source frequency and is even across the source center, unlike Term 1 in the $\hat{\mathrm{x}}$-component. The explicit evaluation of Term 1 is $\hat{\mathrm{z}}\frac{q_e \mu_0}{m_e}\left(J_x H_y - J_y H_x\right)$ where J_x, J_y, H_x, and H_y are all even across the source center resulting in Term 1 to be even as well.

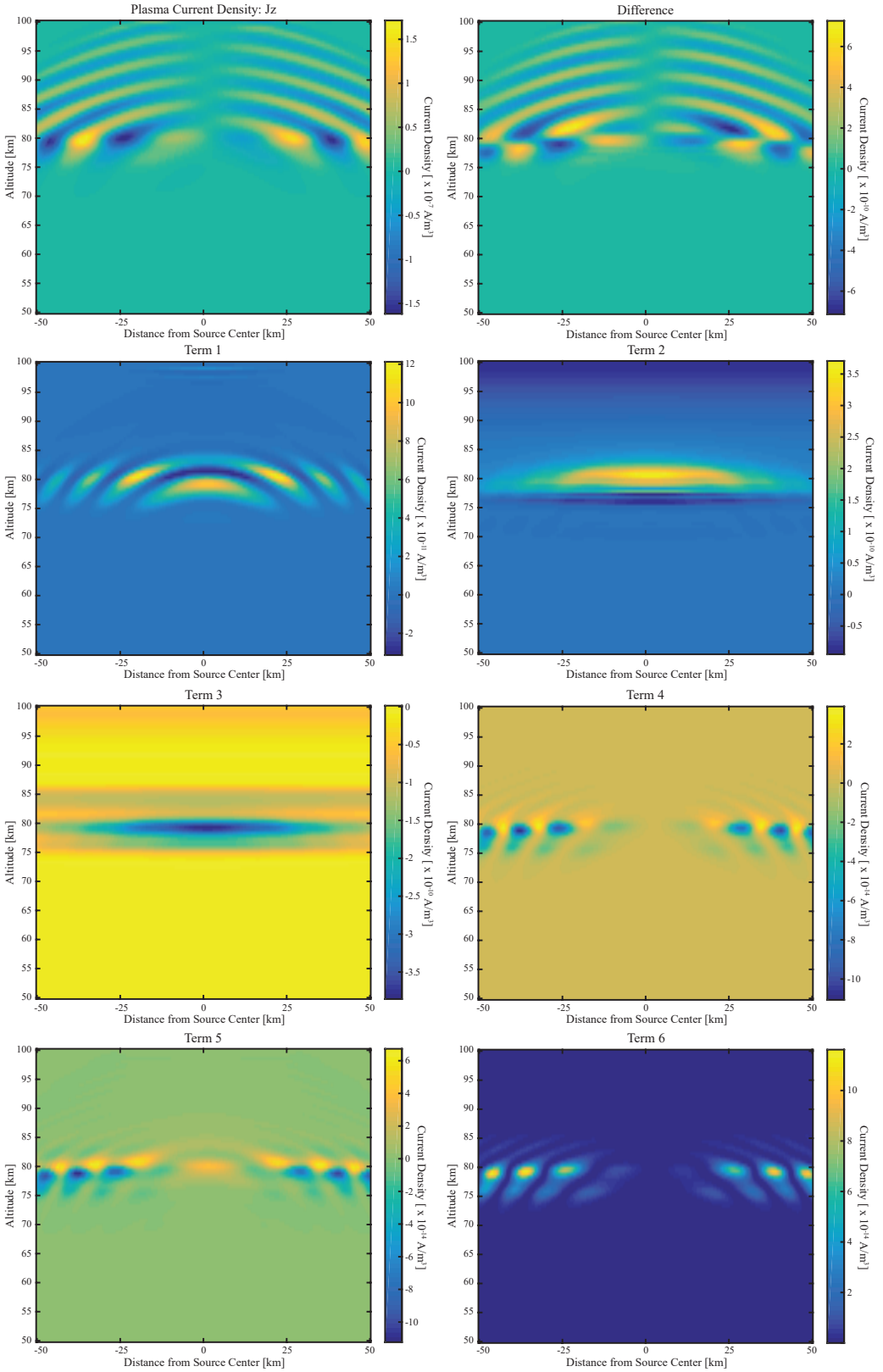

Figure 4-3. $\hat{z}$-components of the additional terms in Eq. 4-9 for 24 kHz VLF heating simulation using Eq. 4-19.

Term 2 is slightly more significant with a peak field strength of 3.5×10^{-10} A/m^3 and appears to be DC in nature due to the large peak in electron temperature at 80 km altitude. There are striations in Term 2 around 76 km which are additional pressure gradients in the plasma current density being formed.

Term 3 is significant for the J_z component of the plasma current density with a peak field strength of -3.5×10^{-10} A/m^3. This is the same field strength but opposite in sign as Term 2. These two terms will not completely cancel each other out though. Term 2 peaks just above 80 km whereas Term 3 peaks just below 80 km. This may be the reason for the inversion in field strength seen in the 'Difference' panel around 80 km in altitude.

Terms 4, 5, and 6 have similar peak field strengths of around 1×10^{-13} A/m^3. These terms again vary spatially at twice the source frequency and have the strongest field strength between 75 km to 85 km. Unlike the $\hat{\mathrm{x}}$-components, the $\hat{\mathrm{z}}$-components of Terms 4, 5, and 6 are even across the source center. This is because J_z is odd across the source center and the divergence of an odd function is even.

The impact over time on the plasma current density of the six additional terms in Eq. 4-9 can be shown by taking the magnitude of plasma current density oscillations. During a VLF heating simulation, the plasma current density and the six additional terms are recorded at every grid cell every iteration. After the simulation, the FFT of the recorded field values is taken at every grid cell and the magnitude at a particular frequency is plotted.

Shown in the top left panel of Figure 4-4 is the magnitude of the $\hat{\mathrm{x}}$-component of the plasma current density at 24 kHz. The strongest region of J_x oscillating at 24 kHz is between 80 km and 90 km altitude with a peak magnitude of -151 dB. The top right panel shows the $\hat{\mathrm{z}}$-component of the plasma current density at 24 kHz. Oscillations of J_z are symmetric about the source center and the strongest region of 24 kHz oscillation is offset 25 km horizontally from the source center with a peak magnitude of -162 dB.

In Figure 4-4, the middle panels show the 24 kHz magnitude and the bottom panels show the 48 kHz magnitude of the sum of the six additional terms in the 1^{st}-order moment of the

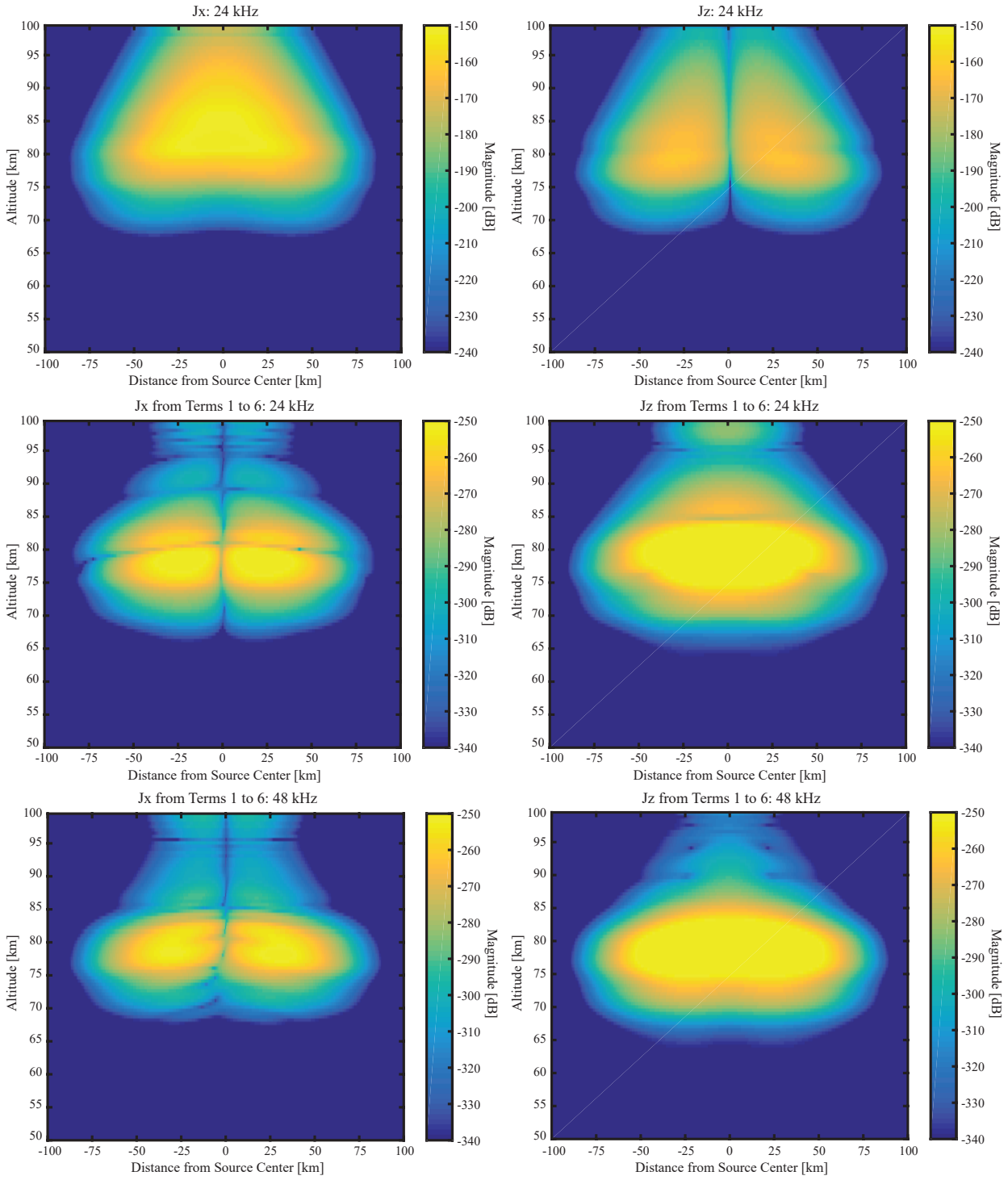

Figure 4-4. Magnitude of: (top left) $\hat{\mathrm{x}}$-component of the plasma current density at 24 kHz, (top right) $\hat{\mathrm{z}}$-component of the plasma current density at 24 kHz, (middle left) $\hat{\mathrm{x}}$-component of Terms 1 to 6 of the plasma current density at 24 kHz, (middle right) $\hat{\mathrm{z}}$-component of Terms 1 to 6 of the plasma current density at 24 kHz, (bottom left) $\hat{\mathrm{x}}$-component of Terms 1 to 6 of the plasma current density at 48 kHz, (bottom right) $\hat{\mathrm{z}}$-component of Terms 1 to 6 of the plasma current density at 48 kHz

Boltzmann Equation with the $\hat{\mathrm{x}}$-components on the left and the $\hat{\mathrm{z}}$-components on the right. It is noted that the scales for these four panels are the same and are 100 dB less than that of the top two panels. The additional terms appear to have the largest impact in the region between 75 km to 80 km. The $\hat{\mathrm{x}}$-components of the additional terms have a null above the source center unlike the total plasma current density shown in the top left panel. Also, the $\hat{\mathrm{z}}$-components of the additional terms do not have a null above the source in contrast to J_z shown in the top right panel. Terms 1 to 6 contribute to the overall plasma current density, but the contributions to the magnitude shown here at 24 kHz are at least 70 dB less than the total plasma current density oscillations at 24 kHz shown in the top two panels.

4.2.2 Second-Order Moment

Three versions of the 2^{nd}-order moment of the Boltzmann Equation have been provided. The first is Eq. 4-19 which is the 2^{nd}-order moment derived utilizing the convective derivative. The second version assumes that conduction and the pressure gradient terms are negligible and was given in Eq. 4-21. The third version makes the same assumptions as the second version, but also assumes that $\nu \gg \omega$ to change the Joule heating term and was given in Eq. 4-23. These three equations for the electron temperature update were implemented in three VLF FDTD heating models. The only difference between the models was the update equation for the electron temperature. All models implemented the 1^{st}-order moment of the Boltzmann Equation, Eq. 4-9.

The electron temperature was recorded when the ionospheric heating reached steady-state and is shown in Figure 4-5. Panels **a**, **b**, and **c** show the electron temperature for the three models using Eq. 4-19, Eq. 4-21, and Eq. 4-23, respectively, at the same iteration. Shown is a 2-D slice of the 3-D grid taken at the midpoint of the $\hat{\mathrm{x}}$-axis, with 50 km in the $\hat{\mathrm{y}}$-direction on either side of the source, and from 50 km to 100 km in altitude. The location of the peak heated region around 77 km is the same in the three simulations. Comparing panels **a**, **b**, and **c**, it is clear that the heated region is larger in simulations utilizing Eq. 4-23, panel **c**. In all three simulations, the electron temperature quickly returns toward ambient past the heated

region. Also, the heating wave can be seen in the electron temperature below 70 km altitude. This is because the electron temperature heats and cools in the span of the VLF wavelength.

Panel **d** shows the difference in electron temperature between the simulation using Eq. 4-21 (panel **b**) and that using Eq. 4-19 (panel **a**). It is noted that the color scale for this plot is in milliKelvin, whereas all of the other plots shown are in Kelvin. It is seen that the maximum difference in electron temperature between these two simulations is only 8 mK, whereas the peak electron temperature in these simulations is around 950 K. In effect, these two simulations produce nearly identical heated electron temperatures. It is therefore concluded that the additional terms in Eq. 4-19 are indeed negligible for CW VLF heating of the D-region ionosphere. An explicit calculation of each term is not needed, because when utilizing all terms, the effect on electron temperature is negligible. Nevertheless, it may still be the case that these terms affect the way multiple beams interact in the ionosphere in important ways.

Panel **e** shows the difference in electron temperature using Eq. 4-23 (panel **c**) and using Eq. 4-21 (panel **b**). The only difference in these equations is the Joule heating term. It is seen that the electron temperature is substantially different in these two simulations. There is a peak difference of nearly 238 K. Panel **f** shows the percent difference of the heated electron temperature calculated as $\frac{\text{Eq.}4-23-\text{Eq.}4-21}{\text{Eq.}4-21} \times 100$. The peak percent difference in electron temperature is 43.5% at 80 km altitude. This represents a significant difference in electron temperature between the simulations caused by the different Joule heating terms.

The electron temperature is important in these simulations because it is used to directly calculate the electron collision frequency. The ambient collision frequency along with the increased collision frequency from VLF heating of the ionosphere for simulations using Eq. 4-21 and Eq. 4-23 are shown on the left of Figure 4-6. Because the heated electron temperature was greatest using Eq. 4-23, simulations using Eq. 4-23 have a larger increase in collision frequency over ambient than those using Eq. 4-21. For both simulations, the largest increase in collision frequency occurs around 78 km, which corresponds with the peak seen in electron

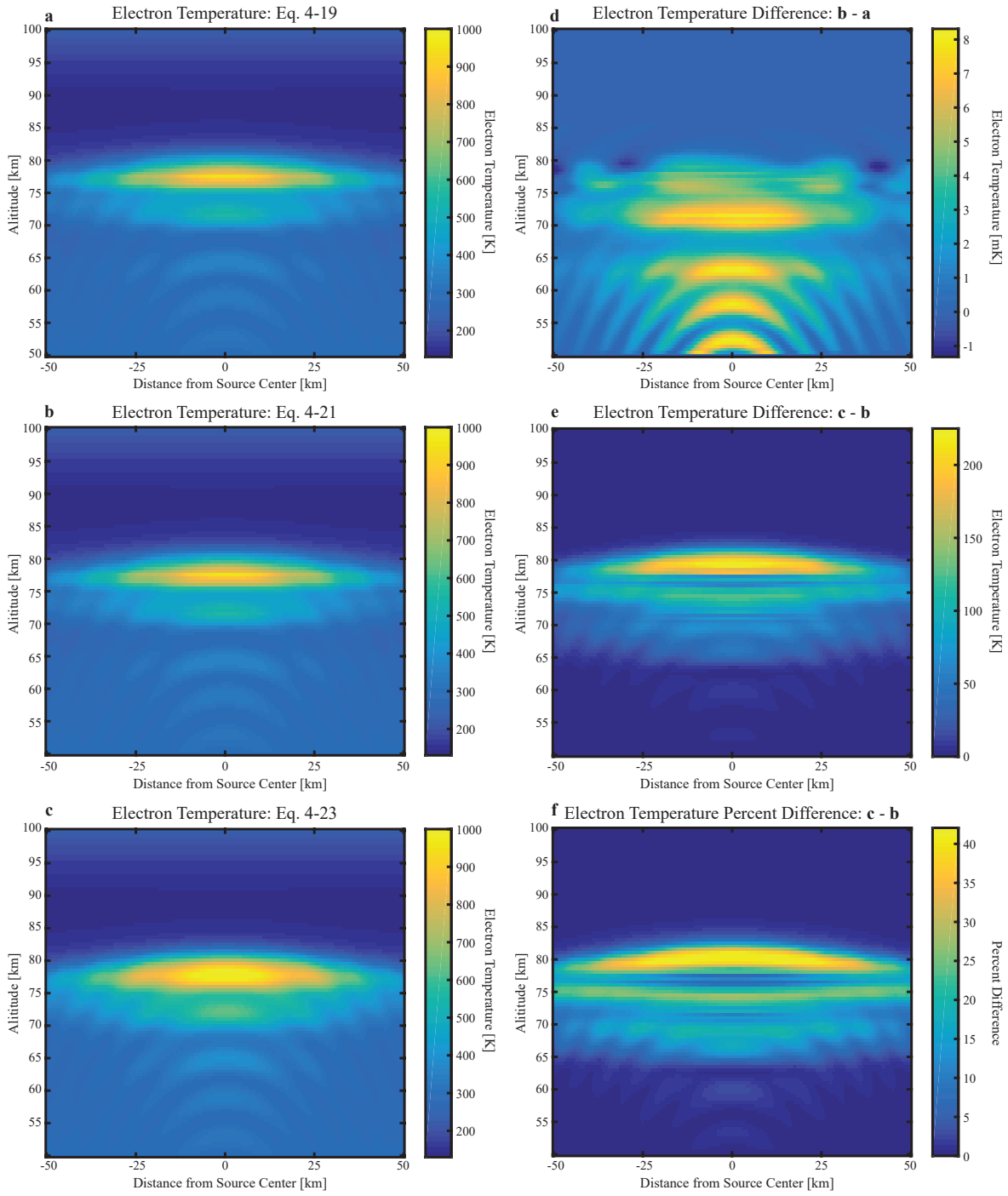

Figure 4-5. Electron temperature from VLF heating (24 kHz) simulations using the three forms of the 2^{nd}-order moment of the Boltzmann Equation (**a**) electron temperature using the 2^{nd}-order moment, Eq. 4-19, (**b**) electron temperature using Eq. 4-21, (**c**) electron temperature using Eq. 4-23, (**d**) difference in electron temperature between simulations using Eq. 4-19 and Eq. 4-21, (**e**) difference in electron temperature between simulations using Eq. 4-21 and Eq. 4-23, (**f**) percent difference of electron temperature between simulations using Eq. 4-21 and Eq. 4-23.

temperature. Also, there is negligible change in collision frequency from ambient above 85 km which again corresponds to the minimal electron temperature heating present there from the 24 kHz source.

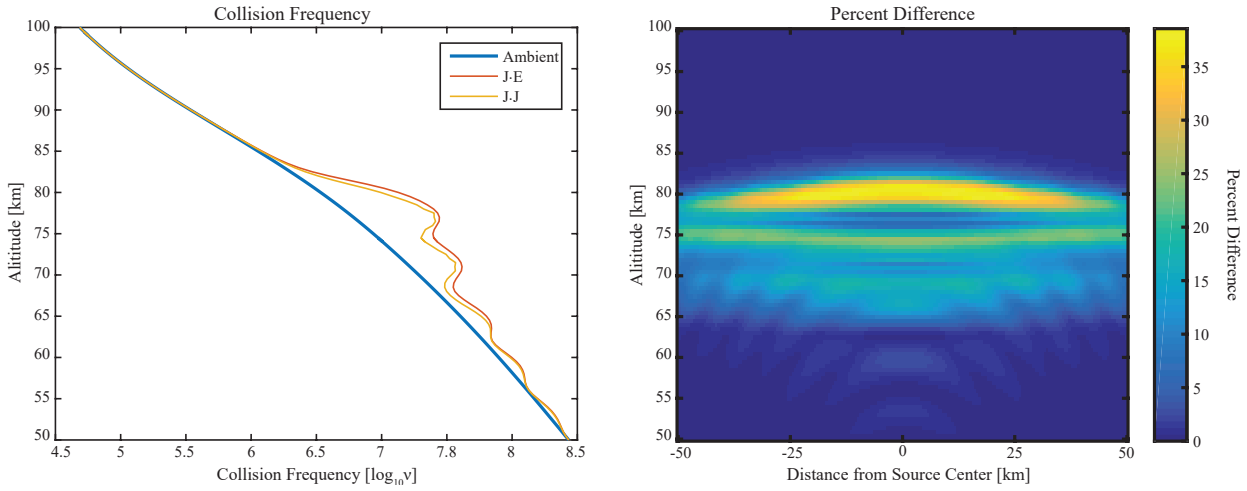

Figure 4-6. (left) 1-D vertical slice through the grid center showing the ambient collision frequency with the increased collision frequency from simulations using Eq. 4-21 labeled JJ and Eq. 4-23 labeled JE, (right) 2-D slice of the collision frequency percent difference between simulations using Eq. 4-21 and Eq. 4-23.

To better understand the differences in increased collision frequency between simulations using Eq. 4-21 and Eq. 4-23, the percent difference in collision frequency is shown in 2-D on the right of Figure 4-6. The peak percent difference in collision frequency is at 80.5 km with a 38.5% increase. Between 65 km and 85 km there is a substantial percent increase in collision frequency ranging from 5% to the peak at 38.5%, with an average of approximately 15% to 20%. Outside of this region, the percent change in collision frequency is less than 5%.

For the simulations shown here, there is a minimal difference between the simulated electron temperature and collision frequency between the models using Eq. 4-19 and Eq. 4-21. It is concluded that for CW VLF heating, the spatial gradient and divergence terms including the conduction terms in the 2^{nd}-order moment are negligible for VLF heating of the D-region ionosphere. There was a large and significant difference in electron temperature and collision frequency when comparing the simulations using Eq. 4-21 and Eq. 4-23. The only difference

between these equations is the Joule heating term, Eq. 4-22, which means that these two terms are not equivalent at VLF frequencies.

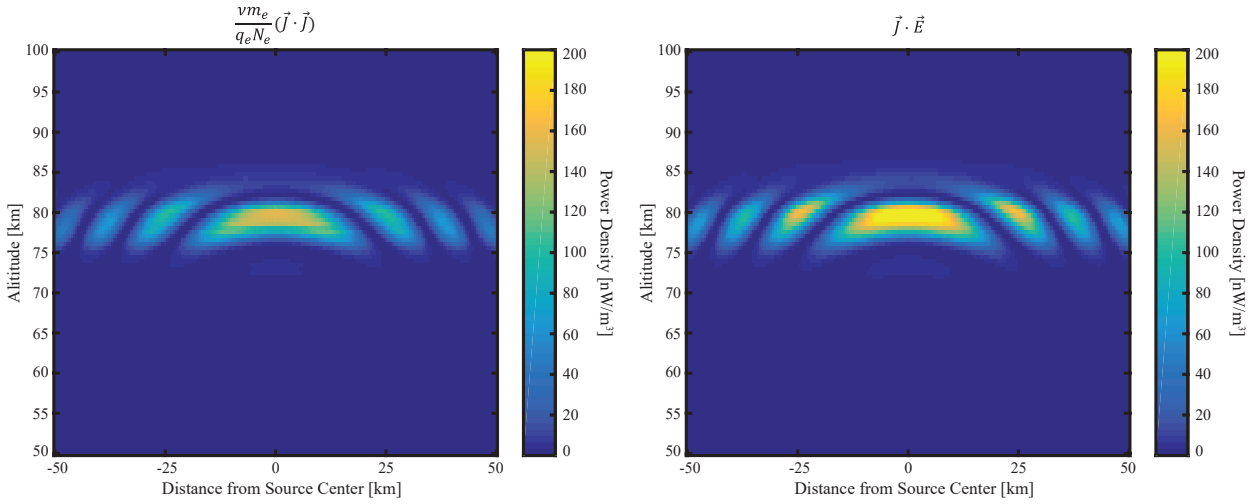

Figure 4-7. Joule heating terms of Eq. 4-22 calculated for the above VLF heating simulations.

The Joule heating term calculated at the same iteration used for the above plots for the simulations using Eq. 4-21 and Eq. 4-23 are shown in Figure 4-7. The areas of maximum power absorption are the same for both simulations. It is clear that the $\vec{J}\cdot\vec{E}$ Joule heating term calculates a more absorption than the $\frac{1}{\sigma_{||}}\vec{J}\cdot\vec{J}$ Joule heating term for CW VLF heating. In the simulations shown here, $\vec{J}\cdot\vec{E}$ caused an overestimation of the electron temperature and absorption in the D-region ionosphere, and would correspond to an overestimation of signal penetration into the ionosphere.

4.2.3 Second-Order Moment's Dependence on First-Order Moment

The additional terms present in the 1^{st}-order moment of the Boltzmann equation were shown in Section 4.2.1 to potentiality be important for VLF heating of the D-region ionosphere. The difference at one instant in time between simulations utilizing the 1^{st}-order moment 4-9 and the simplified version, Eq. 4-17, was around two orders of magnitude lower than the peak plasma current density present. This is a 1% difference which is also a 40 dB difference. This difference is large enough that any additional frequencies generated due to

the additional pressure terms and interaction with the waves magnetic field may be able to be detected with present VLF receivers.

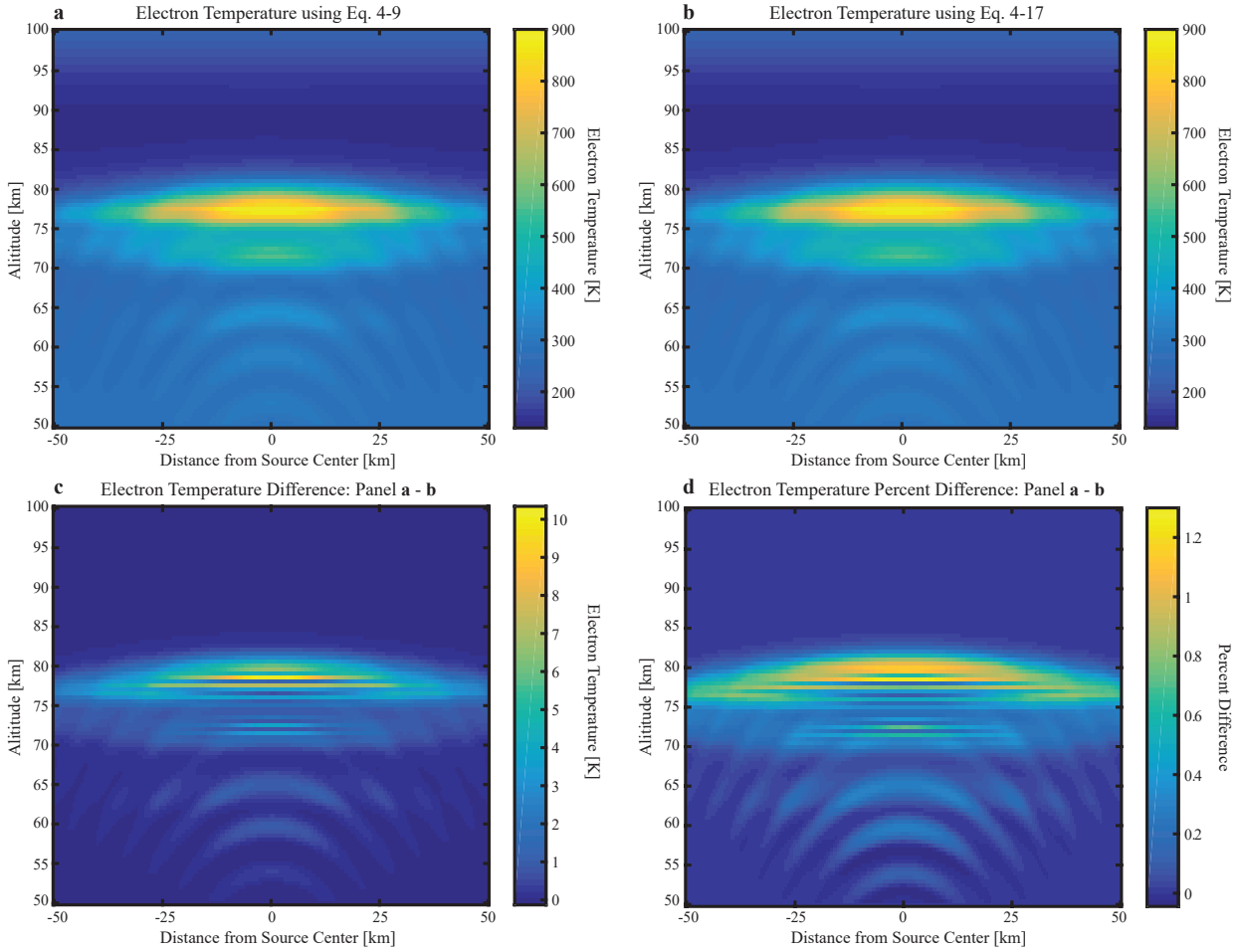

Figure 4-8. (**a**) Electron temperature from a simulation using the 1^{st}-order moment, Eq. 4-9, (**b**) electron temperature from a simulation using the simplified 1^{st}-order moment, Eq. 4-17, (**c**) difference in electron temperature between simulations shown in panels **a** and **b**, (**d**) percent difference of electron temperature between simulations shown in panels **a** and **b**.

Conversely, the additional terms present in the 2^{nd}-order moment of the Boltzmann Equation, Eq. 4-19, were found to be negligible. The difference in electron temperature between simulations utilizing the 2^{nd}-order moment of Eq. 4-19 and the simplified version, Eq. 4-21, was only 8 mK. This is about a $1 \times 10^{-3}\%$ difference in electron temperature which is also a 100 dB difference. This small difference is most likely indistinguishable in VLF heating experiments.

Two VLF heating simulations were run in order to determine if the version of the 1^{st}-order moment impacted significantly the electron temperature. The electron temperature for the simulation using the 1^{st}-order moment, Eq. 4-9, is shown in Figure 4-8**a**, and the electron temperature for the simulation using the simplified 1^{st}-order moment, Eq. 4-17, is shown in Figure 4-8**b**. Both simulations used the 2^{nd}-order moment, Eq. 4-19. These two plots appear nearly identical to each other.

Differences are more clear when subtracting the two electron temperatures from each other as seen in Figure 4-8**c**. A peak electron temperature difference of 10 K is present around 78 km altitude. Also evident are the vertical striations between 70 km and 80 km. These are additional pressure gradients being produced in the 1^{st}-order moment. Figure 4-8**d** shows the percent difference between the two simulations with a maximum percent difference of 1.2% around 80 km. This difference can create additional frequencies which may be significant enough to be detected by a VLF receiver during a VLF heating experiment.

4.2.4 Discussion

There are seven additional terms (Eqs. 4-10 to 4-16) present in the 1^{st}-order moment of the Boltzmann Equation (Eq. 4-9) which are oftentimes assumed to be negligible. Terms 1 to 6 are time-varying and Term 7 was set equal and opposite to the ambient value of Term 2 and Term 3. For VLF heating of the D-region ionosphere, Figures 4-1 and 4-3 showed that the difference in plasma current density between simulations that utilize the 1^{st}-order moment (Eq. 4-9) and the simplified version (Eq. 4-17) is 2 orders of magnitude less than the peak plasma current density. It was also shown in these figures that some of the six additional terms oscillate dominantly at twice the source frequency and can create pressure waves. These additional plasma current density oscillatory frequencies and pressure waves are only present when utilizing the Eq. 4-9 version of the 1^{st}-order moment.

Figures 4-1 and 4-3 are only able to show the impact of the six additional terms on the plasma current density at one snapshot in time. The impact over time on the plasma current density from VLF heating was shown in Figure 4-4. The strength of the contribution of 24

kHz oscillations from the six additional terms together was at least 70 dB lower than the total plasma current density magnitude at 24 kHz. The 48 kHz contribution to the plasma current density from the six additional terms was determined alone. It was not strong enough to be distinguishable above the numerical noise floor in the J_x plasma current density.

The 1^{st}-order moments impact on the electron temperature was shown in Figure 4-8. There was a peak 1.2% difference in electron temperature between simulations using the 1^{st}-order moment, Eq. 4-9, and using the simplified 1^{st}-order moment, Eq. 4-17. There were additional electron temperature striations present which arise due to the pressure gradients in the 1^{st}-order moment.

There is an impact on the plasma current density when utilizing the 1^{st}-order moment of the Boltzmann Equation. This impact is noticeable when comparing the differences in simulation results of the plasma current density and electron temperature between simulations using two versions of the moment. In the results presented here, the added frequencies the plasma current density oscillate at which are generated by the 6 additional terms were not in general above the numerical noise floor. If the numerical noise floor is lowered in future simulations, then these additional oscillations of the plasma current density may be detectable. Overall, the 1^{st}-order moment of the Boltzmann Equation is recommended to be utilized in future simulation. This is to accurately simulate all of the radio wave interactions with the ionosphere such as creation of additional oscillatory frequencies of the plasma current density, striations in the electron temperature, and the impact on the peak electron temperature.

The additional terms in the 2^{nd}-order moment of the Boltzmann Equation (Eq. 4-19) were found to be insignificant for CW VLF heating of the D-region ionosphere. The difference in electron temperature between simulations utilizing the 2^{nd}-order moment including convection and conduction and the simplified version (Eq. 4-21) was found to be less than 8 mK whereas the peak electron temperature was 1000 K.

The largest impact on electron temperature was from the version of the Joule heating term (Eq. 4-22) that was used. Figure 4-5**e** showed that the electron temperature heated

region was larger and hotter in simulations using the $\vec{J} \cdot \vec{E}$ Joule heating term (Eq. 4-23) versus simulations using the $\frac{\nu m_e}{q_e N_e}\left(\vec{J} \cdot \vec{J}\right)$ Joule heating term (Eq. 4-21). The electron temperature was found to be up to 40% hotter as shown in Figure 4-5**f** which caused up to a 38.5% difference in collision frequency between the two simulations as seen on the left in Figure 4-6.

For the VLF heating simulations of the D-region ionosphere shown here, the 2^{nd}-order moment of the Boltzmann Equation derived including convection and conduction (Eq. 4-19) does not need to be implemented. The form of the 2^{nd}-order moment that is recommended to be implemented is Eq. 4-21. This is because the Joule heating term in this equation is the form derived in the 2^{nd}-order moment and does not make any more assumptions like the Joule heating term in Eq. 4-23 makes. For other VLF heating experiments such as beat-wave heating or thermal cubic nonlinearity, the additional terms in Eq. 4-19 may become important.

4.3 HF Heating

The HF cross-modulation simulations shown in Ch. 3 were run using the simplified versions of the 1^{st}- and 2^{nd}-order moments of the Boltzmann Equation, Eq. 4-17 and Eq. 4-23. Ideally, the HF cross-modulation experiments would be simulated utilizing the 1^{st}- and 2^{nd}-order moments derived including the convective derivative. This is not done because the HF heating model is currently 1-D and the pressure gradient terms cannot be evaluated properly.

The Joule heating term, Eq. 4-22, in the 2^{nd}-order moment of the Boltzmann Equation was shown to have the most significant impact on electron temperature in the VLF heating simulations shown above. The importance of the Joule heating term will be evaluated at HF by re-simulating the 2.5 kHz sine wave modulation HF cross-modulation experiment utilizing Eq. 4-21 and comparing the results to those previously obtained using Eq. 4-23.

The top left panel of Figure 4-9 shows the difference in magnitude of the probe pulse at the top of the ionosphere between the two simulations calculated as the simulation using Eq. 4-21 minus the simulation using Eq. 4-23. The positive difference means that the simulation

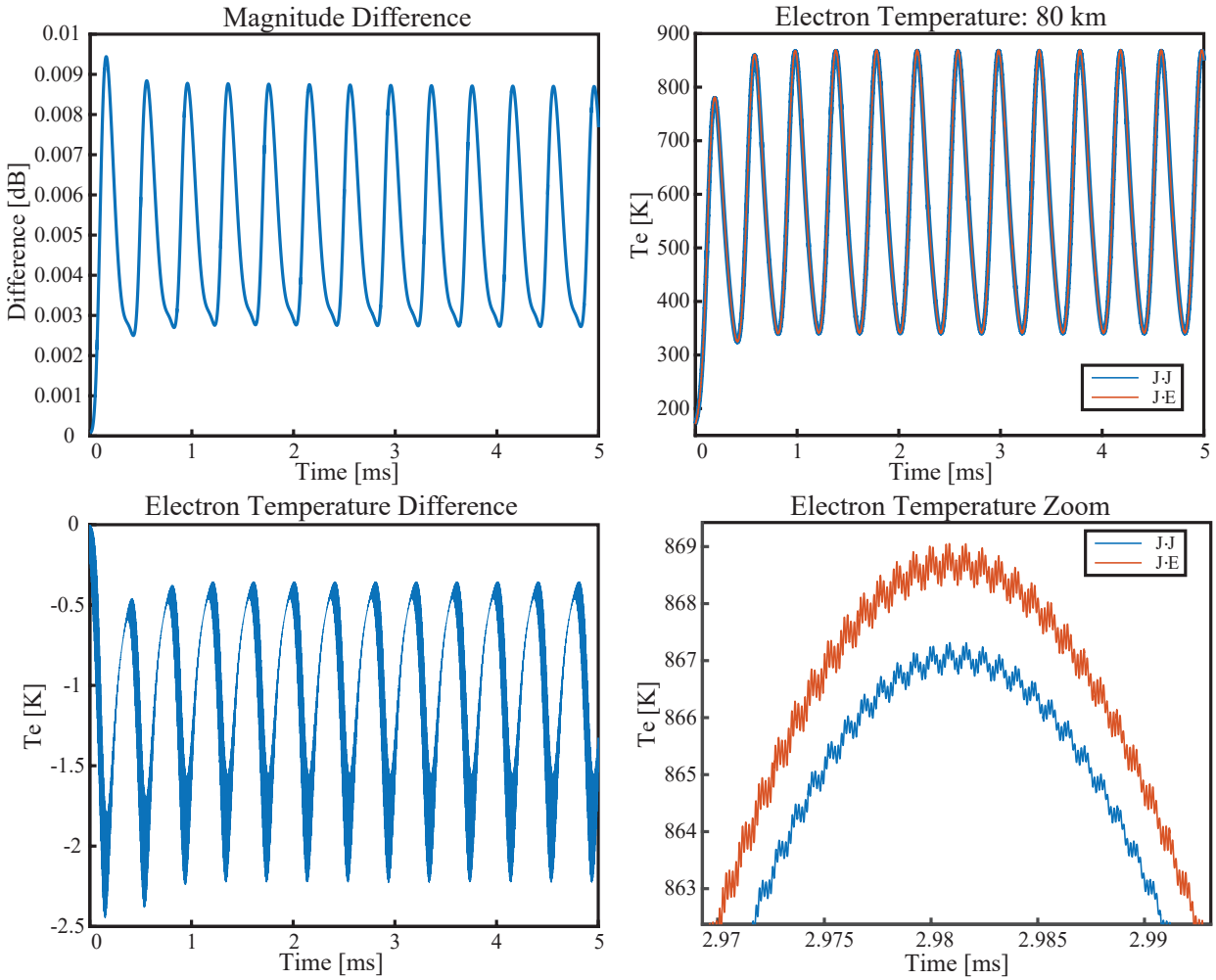

Figure 4-9. HF simulations of 2.5 kHz sine wave cross-modulation using the two Joule heating terms shown in Eq. 4-22 (top left) Difference in the magnitude of the probe pulse between the two simulations, (top right) electron temperature recorded at 80 km altitude, (bottom left) difference in electron temperature between the two simulations, (bottom right) enlargement of a peak in the electron temperature shown in the top right plot.

using Eq. 4-23 models a larger attenuation of the probe pulse at the top of the ionosphere. More attenuation is the result of a hotter electron temperature and therefore higher collision frequency.

The electron temperature at 80 km over the 5 ms simulation is shown in the top right panel of Figure 4-9. There is no clear difference in the electron temperature in this plot. The VLF heating simulations at 24 kHz showed a large and significant difference in electron

temperature between the two Joule heating terms. The difference in electron temperature between the two simulations is shown in the bottom left panel of 4-9. The maximum difference between simulations is less than 2.5 K and the peak electron temperature at 80 km is around 870 K. The electron temperature difference is less than 1% of the peak electron temperature.

An enlargement of the electron temperature around 2.98 ms is shown in the bottom right panel of Figure 4-9. The HF oscillations of the electron temperature are clearly visible as the entire temperature profile oscillates predominantly at 2.5 kHz. As was seen in the bottom left panel, the electron temperature difference between the two simulations is around 2.5 K.

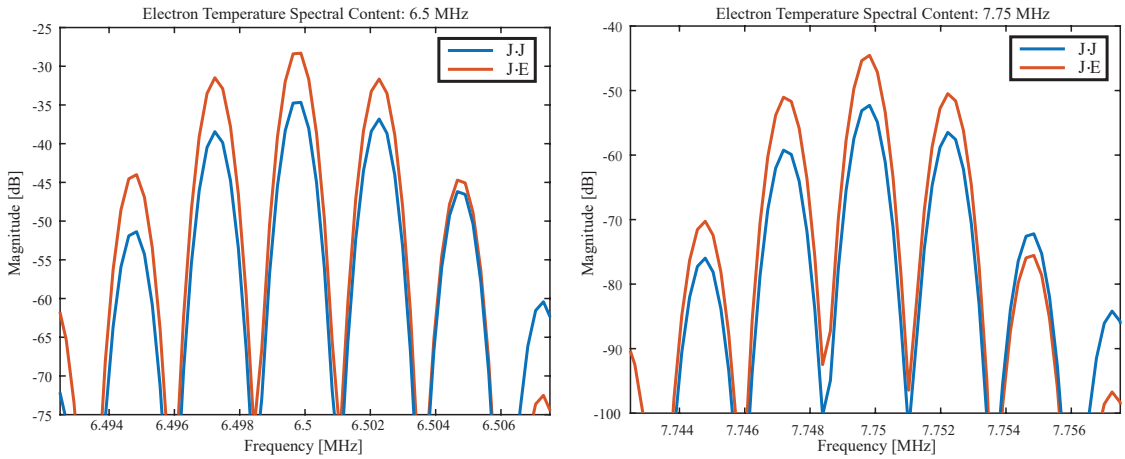

Figure 4-10. Electron temperature spectrum at 80 km altitude for 2.5 kHz cross-modulation experiment for two simulations using the two Joule heating terms shown in Eq. 4-22 (left) centered around 6.5 MHz, (right) centered around 7.75 MHz.

The HF oscillations in the simulation using Eq. 4-23, $\vec{J} \cdot \vec{E}$ Joule heating term, appear to be larger than those in the simulation using Eq. 4-21, $\frac{\nu m_e}{q_e N_e}\left(\vec{J} \cdot \vec{J}\right)$ Joule heating term. The magnitude of electron temperature HF oscillations are shown on the left of Figure 4-10 centered around 6.5 MHz and on the right centered around 7.75 MHz. The 6.65 MHz electron temperature oscillation is 6 dB stronger in the simulation using $\vec{J} \cdot \vec{E}$ than in the simulation using $\frac{\nu m_e}{q_e N_e}\left(\vec{J} \cdot \vec{J}\right)$. At 7.75 MHz, the electron temperature oscillations are 7.5 dB stronger in the simulation using $\vec{J} \cdot \vec{E}$.

The attenuation on the probe pulse at the top of the ionosphere for these cross-modulation experiments was between 2 dB and 4 dB. The maximum difference in attenuation between the

simulations here (top left panel of Figure 4-9) is less than 1% of this. The impact of the ambient neutral profiles and ambient electron density profiles were shown in Chapter 3 to have a much more significant impact than the Joule heating terms here. Therefore, at HF frequencies, the Joule heating terms and specifically Eqs. 4-21 and 4-23 are found to produce very similar electron temperatures and nearly identical cross-modulation simulation results.

The nonlinear D-region heating FDTD model developed in this chapter implemented the 1^{st}- and 2^{nd}-order moments of the Boltzmann equation derived accounting for the convective derivative to simulate CW VLF heating. The version of the Joule heating term impacted the electron temperature significantly for CW VLF heating, but was not significant for HF cross-modulation experiments. The effect on skywave propagation from electron heating is investigated in Chapter 5.

CHAPTER 5
ANALYSIS OF LIGHTNING SKYWAVES

In this chapter, two-dimensional, cylindrically symmetric, nonlinear FDTD models are utilized to investigate skywave penetration into the ionosphere. The impact of plasma nonlinearities on skywave propagation is analyzed through the effective skywave reflection height because it is a relatively simple measurement to make in the field. Section 5.1 presents results showing the individual effect of electron density changes and electron heating on the effective skywave reflection height using a nonlinear lightning FDTD model discretized without applying the Möbius transformation. The results are used to analyze the effects of the wave on the plasma medium. Section 5.2 presents the nonlinear lightning FDTD model discretized applying the Möbius transformation and is used to examine the effective skywave reflection height in Section 5.3 for a variety of test cases and as a function of frequency in Section 5.4.

5.1 Non-Möbius Lightning FDTD Model

The lightning discharge impacts the ionosphere in a number of ways. Lightning emits a propagating electromagnetic pulse (EMP) that directly heats the ionosphere (Joule heating); it also causes the establishment of a quasi-electrostatic field [*Pasko*, 1998] that heats the ionosphere and additionally has the potential to produce electric breakdown of the ionosphere. Both of these strong fields interact with the D-region ionosphere causing significant electron heating.

A nonlinear lightning FDTD model discretized without applying the Möbius transformation is utilized here to study the effects of electron density changes and electron heating on skywave propagation. This model is not utilized to make absolute predictions about the change in skywave penetration in a linear model versus nonlinear model. Rather, only the relative importance of electron heating and electron density changes are analyzed through differences between the three versions described below. *Kotovsky and Moore* [2017] noted that "the differencing technique implemented here is sufficient for simulations of ionospheric disturbances at distances within a few hundred kilometers of the lightning channel, these

simplifications would not likely be sufficient for precise calculations of lightning radiation fields." The differencing technique implemented for the electrodynamic model is non-Möbius and 1^{st}-order accurate so it is unclear whether oblique reflections are calculated accurately. A 2^{nd}-order accurate Möbius transformation implementation will be presented later in this chapter to analyze the skywaves specifically.

The non-Möbius transformation model was described in detail by *Kotovsky* [2016] and *Kotovsky and Moore* [2017] and was previously used to model Long Recovery Early Events (LOREs) in the nighttime ionosphere. A useful feature of this model is the capability to isolate how changes in electron temperature and the chemical makeup (i.e., electron density) of the ionosphere affect skywave propagation. In order to do this, three versions of the lightning FDTD model are created. The first version is nonlinear and includes changes in electron temperature labeled (T_e) in plots, and changes in chemical makeup labeled (N_e) in plots. The second version is nonlinear and includes changes in electron temperature, but the chemical makeup remains at the ambient values. By comparing the outputs from these two versions, it is possible to determine the impact that changes in electron density have on skywave propagation. The third version is linear and maintains the ambient electron temperature and chemical makeup of the ionosphere. Comparing the results of the second version, nonlinear (T_e), and the third version, linear, allows a determination of the effect of electron temperature changes on skywave propagation.

The simulation space used for this model was 2-D cylindrically symmetric, 100 km vertically, and 400 km radially. The grid step size was 200 m vertically and 1000 m radially with a time step of 3 ns. The lightning return stroke channel used in this model was a lossless transmission line from ground level up to 10 km with a return stroke speed of $2/3$ the speed of light. The Heidler function [*Heidler et al.*, 1999] was used to define the channel base current with $\tau_1 = 50$ μs and $\tau_2 = 250$ μs.

A 200 kA return stroke peak current was simulated and the vertical electric field on the ground 250 km away from the lightning channel is shown in Figure 5-1 for all three versions

of the model. The electric field has been normalized by the peak groundwave electric field. As a result, the groundwaves for the three models are identical and peak at the same time because they propagate through bounded free space and do not significantly interact with the ionosphere. A high peak current of 200 kA was utilized in order to most exaggerate any effects that changes in chemistry would have on the effective reflection height.

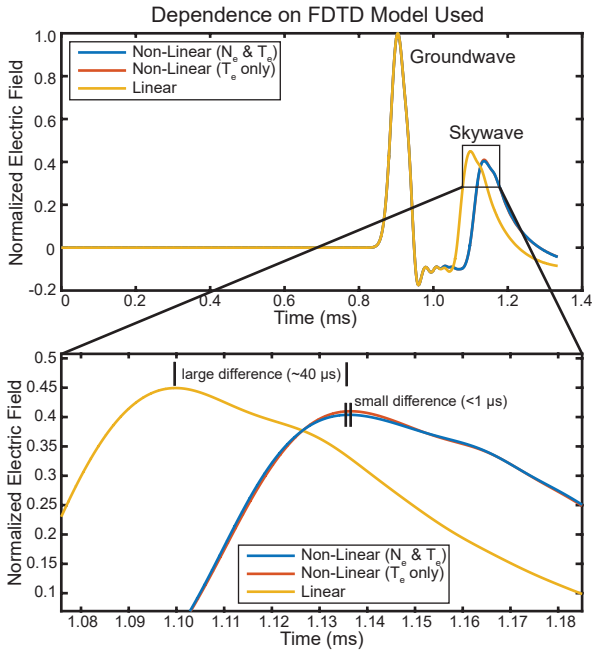

Figure 5-1. (top) Vertical electric field showing the groundwave and one-hop skywaves recorded 250 km away from the lightning channel for the nonlinear (N_e and T_e), nonlinear (T_e only), and linear versions, (bottom) enlarged version of the vertical electric field.

While the normalized groundwaves are the same, the skywaves are not. For the one-hop skywaves, there is a clear distinction in timing of the waveform between the linear model and the two nonlinear models. The bottom panel of Figure 5-1 shows an enlargement of a portion of the top panel of Figure 5-1 around the peak region of the three skywaves. The peak skywave electric field in the linear model arrives approximately 40 μs before both skywave peaks of the nonlinear models. The difference between peak skywave electric fields for the nonlinear models is minor and is less than 1 μs. When using the peak-to-peak method to determine effective skywave reflection height and since all three groundwaves peak together,

any delay of peak skywave electric field indicates a higher effective skywave reflection height. The effective skywave reflection heights are determined to be 90.5 km for the linear model, 99.5 km for the nonlinear model (N_e and T_e) and 99.6 km for the nonlinear model (T_e only). The skywaves in the nonlinear models penetrate effectively nine kilometers deeper than in the linear case according to these non-Möbius, 1^{st}-order accurate models. The 0.1 km difference of effective skywave reflection height between the two nonlinear models is minor and indicates that changes in ionization do not significantly affect skywave propagation for a first return stroke. The 9.1 km difference of effective skywave reflection height between the nonlinear (T_e only) and linear models indicates that electron heating could possibly modify skywave propagation significantly and it should be properly evaluated. We use this information in our formulation of the 2^{nd}-order accurate Möbius transformation implementation. It is concluded that the main nonlinear factor affecting EMP penetration into the ionosphere is electron heating and not changes in electron density for first return strokes. Because our interest lies in first return strokes, the impact of electron heating is investigated further in this work and changes in electron density are not.

5.2 Möbius Lightning FDTD Model

To more accurately analyze the effects of electron heating on skywave propagation, a nonlinear lightning FDTD discretized applying the Möbius transformation is presented. The basis of the lightning skywave model presented here is Linear Method 2 described in Chapter 2. In this model, the collision frequency is allowed to change temporally and spatially to account for electron heating. The electron density is held constant at the ambient value. The analysis in Section 5.1 indicates that this approximation is valid for investigating the propagation of skywave components radiated by first return strokes. To calculate electron heating, the lightning FDTD model utilizes the quasi-static heating approximation to update a temporally and spatially varying ionospheric mobility [*Kotovsky*, 2016; *Kotovsky and Moore*, 2017]. The relationship between electron mobility and collision frequency is shown in Eq. 5-1. Calculating the collision frequency in this manner assumes that the collision frequency is much greater

than the cyclotron frequency and the wave frequency. This assumption is valid here because an isotropic plasma is simulated and only frequencies below 100 kHz are investigated.

$$\nu = \frac{q_e}{m_e \mu_e} \tag{5-1}$$

Two versions of the lightning FDTD model are utilized to determine the effect of electron heating on skywave penetration. This first version is nonlinear, allowing the collision frequency and therefore conductivity of the ionosphere to change spatially and temporally. The second version is linear and holds the conductivity of the ionosphere constant. Both versions are 2-D, cylindrically symmetric and utilize a 200 m radial and 200 m vertical spatial step size with grid dimensions of 500 km radially by 104 km vertically. Used throughout this work is electron density profile I and neutral profile 4 shown in Figure 3-4.

For the mobility model described by *Kotovsky and Moore* [2017], the ionospheric conductivity at 80 km is shown in Figure 5-2 as a function of the electric field strength. It is seen that the conductivity decreases rapidly for electric field values between 0.05 V/m and 1 V/m and levels off as the electric field increases past 1 V/m. On a base level, a decrease in conductivity allows the electric field to penetrate deeper into the plasma. Because the electric field produced by a lightning return stroke is directly related to the return stroke peak current, there are diminishing returns in changes of ionospheric conductivity as the return stroke peak current increases. For relatively weak lightning discharges, as the return stroke peak current increases, it is expected that the conductivity of the ionosphere will decrease rapidly causing the effective skywave reflection height to increase rapidly. For relatively strong lightning discharges, as the return stroke peak current increases, it is expected that the conductivity of the ionosphere will decrease slowly and the effective skywave reflection height will increase to a lesser extent.

The lightning return stroke channel used in the model starts at ground level and continues up to 10 km with a return stroke speed of 2/3 the speed of light. The Heidler function [*Heidler et al.*, 1999] is used to define the channel base current in order to represent return stroke

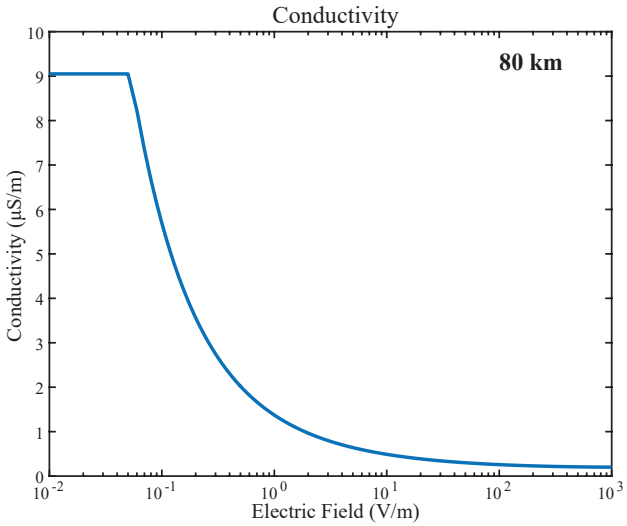

Figure 5-2. Conductivity of the ionosphere at 80 km as a function of the electric field.

current fronts and recoveries in comparison to linear rise with exponential decay models. The Heidler function parameters used were $\tau_1 = 20\,\mu s$ and $\tau_2 = 100\,\mu s$. These parameters do not directly represent the simulated return stroke risetime and recovery. The simulated return stroke risetime was $7.6\,\mu s$ when measured from 10% to 90% of peak current. The recovery time was $72.1\,\mu s$ when measured from the time of peak current to the 50% value during current decay. These values are larger than realistic lightning due the grid's inability to resolve higher frequencies present in faster risetimes. The current propagates up the return stroke channel using a lossless transmission line model: $I(z,t) = I(0, t - z/v)$. When there is no attenuation, all of the charge is deposited at the top of the lightning channel. Because of this, the quasi-static fields are larger in this model than a model utilizing a lossy transmission line model. For this implementation, there is also a negative field radiated from the top of the channel, and this second field does not appear to exist in actual ground data. Nevertheless, we inperpret our simulations with this knowledge in mind.

The radiation fields are important for skywave propagation and to verify their magnitude in this model, the electric field at 100 km is compared against an analytical formula that estimates the far-field electric field as a function of time or distance [*Uman and McLain*, 1969; *Uman et al.*, 1975]:

$$E_z(D,t) = -\frac{v}{2\pi\epsilon_0 c^2 D} i(t - D/c) \tag{5-2}$$

where $E_z(D,t)$ is the vertical electric field on the ground at a distance D and time t, v is the return stroke speed, and $i(t-D/c)$ is the current at the channel base at retarded time $t-D/c$. In this work, only the peak electric field strength will be compared to the peak return stroke current.

For a 100 kA return stroke peak current at 100 km distance with a return stroke speed of 2/3 the speed of light, this formula calculates a peak electric field of 40 V/m. With the same parameters, the lightning FDTD model simulates a peak electric field of 41.1 V/m. Therefore, the lightning channel without attenuation utilized here accurately simulates the far-field radiation pattern as expected of a lightning return stroke.

5.3 Skywave Reflection Height

5.3.1 Linear vs Nonlinear Model

A decrease in electrical conductivity from an electron temperature increase due to electric field heating, as shown in Figure 5-2, is expected to allow deeper penetration of the electric field into the ionosphere in the nonlinear model. The vertical electric field created by a 100 kA return stroke peak current lightning discharge 850 μs after the start of the lightning stroke is shown on the left of Figure 5-3 for the linear FDTD and on the right of Figure 5-3 for the nonlinear FDTD including heating. The black horizontal bar at 80 km altitude denotes the extent of the electric field penetration into the ionosphere in the linear model. The black vertical bar at 250 km radially denotes the groundwave wavefront in the linear model. In the nonlinear model, the groundwave wavefront denoted by the vertical bar is not affected significantly, which is to be expected. It is clear that the electric field in the nonlinear model extends visibly above the horizontal bar and reaches over 85 km altitude directly above the lightning channel, a further 6 km than the linear model. The increased penetration occurs for both the quasi-electrostatic (QE) field [*Pasko*, 1998] (and possibly induction fields) directly above the lightning channel and for the skywave wavefront at 250 km radially.

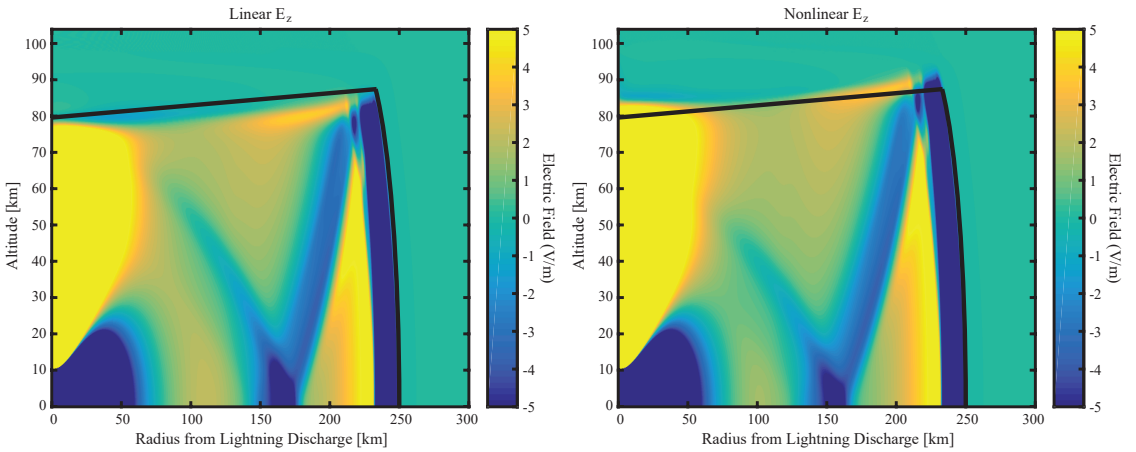

Figure 5-3. 100 kA return stroke peak current lightning discharge simulated and the vertical electric field is recorded at 850 μs. Horizontal and vertical black bars denote the wavefront in the linear model. (left) vertical electric field in the linear model, (right) vertical electric field in the nonlinear.

The increased penetration of the electric field into the ionosphere is expected to be seen on the ground as a delay in the time-domain skywave waveform in the nonlinear model versus linear model. The vertical electric field as a function of time measured at ground level 250 km away from the lightning channel for a 100 kA return stroke peak current is shown on the left of Figure 5-4 for the linear and nonlinear versions.

It can be seen that the groundwaves for the two models are exactly the same. The rise, peak and fall of the groundwaves all align perfectly. Even the first negative peak and subsequent ripple align until the skywave of the linear model arrives. This behavior is as expected because the groundwave does not significantly interact with the ionosphere and it propagates essentially through bounded free-space, which in this model is the region from ground level up to 60 km.

For the one-hop skywaves shown here, there is a clear distinction in timing of the waveform between the linear model and the nonlinear model. The right panel of Figure 5-4 shows an enlargement of the left panel around the skywave peak. The peak skywave electric field in the linear model arrives approximately 21.6 μs before the skywave peak of the nonlinear model. When using the peak-to-peak method to determine effective skywave reflection height,

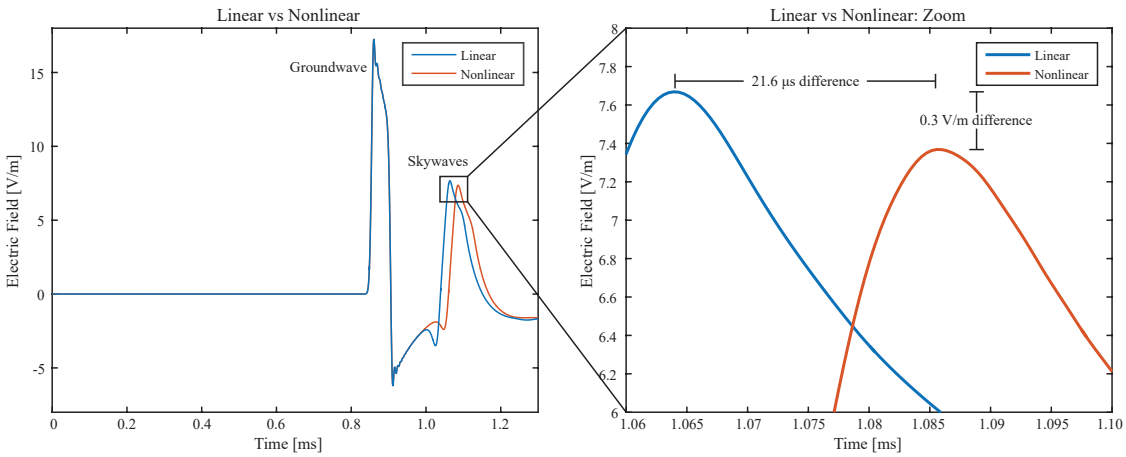

Figure 5-4. (left) Vertical electric field showing the groundwave and one-hop skywaves recorded 250 km away from the lightning channel for the nonlinear and linear versions, (left) enlarged version of the vertical electric field around the skywave peak.

and because the groundwaves peak together, any delay of peak skywave electric field indicates a higher effective skywave reflection height. The effective skywave reflection heights are determined to be 92.4 km for the linear model and 97.8 km for the nonlinear model. The skywave in the nonlinear model penetrates effectively 5.4 km deeper than for the linear case. This is similar to the increased penetration seen in Figure 5-3. The peak electric field of the skywave in the nonlinear model is found to be 0.3 V/m weaker than in the linear model. The weaker electric field is caused by the increased absorption in the ionosphere due to the increased collision frequency.

5.3.2 Dependence on Return Stroke Peak Current

A 100 kA return stroke peak current was shown to penetrate effectively 5.4 km deeper into the ionosphere in the nonlinear model as compared to the linear model. In Section 5.2 it was hypothesized that effective skywave reflection heights would increase substantially as return stroke peak current increased for weak return strokes ($<$50 kA) and would level off for relatively strong return strokes ($>$50 kA). The left panel of Figure 5-5 shows the normalized vertical electric field at ground level as a function of time measured 250 km away from the lightning channel for eight different peak currents and the linear model. The electric field was normalized by the peak groundwave electric field in each simulation. It is noted that when

the electric field is normalized this way, linear simulations produce exactly the same electric field waveform regardless of the peak return stroke current. As is expected, the normalized groundwave is the same in all nine simulations. Therefore, any delay in skywave peak directly correlates to an increased effective skywave reflection height.

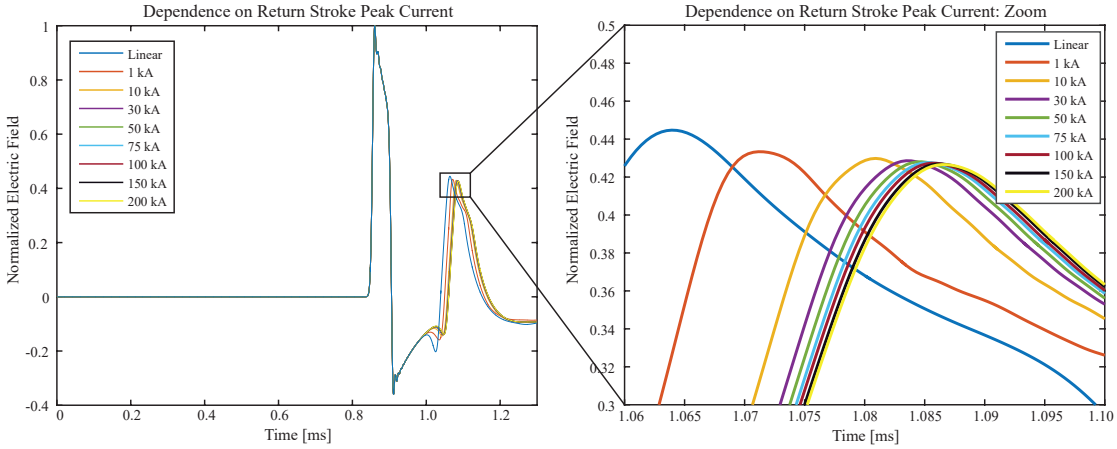

Figure 5-5. (left) Vertical electric field for return stroke peak currents of 1 kA, 10 kA, 30 kA, 50 kA, 75 kA, 100 kA, 150 kA, 200 kA and the linear model recorded at 250 km from the lightning stroke, (right) enlargement around the skywave peak.

The right panel of Figure 5-5 is a zoomed in version of the recorded electric field, focusing on the skywave peaks. For the linear model, the effective skywave reflection height is not a function of the peak return stroke current. In the simulation shown here, the linear model has an effective skywave reflection height of 92.4 km. For the nonlinear models, the effective skywave reflection height is very much a function of return stroke peak current. The eight return stroke peak currents modeled are 1 kA, 10 kA, 30 kA, 50 kA, 75 kA, 100 kA, 150 kA, and 200 kA with effective skywave reflection heights of 94.2 km, 96.6 km, 97.3 km 97.6 km, 97.7 km, 97.8 km, 98 km, and 98.1 km, respectively.

As hypothesized, as the return stroke peak current increases, the relative increase in effective skywave reflection height decreases. Between linear and 1 kA, 1kA and 10 kA, 10 kA and 30 kA, 30 kA and 50 kA, 50 kA and 75 kA, 75 kA and 100 kA, 100 kA and 150 kA, and 150 kA and 200 kA, the increases in effective skywave reflection heights are 1.8 km, 2.4 km, 0.7 km, 0.3 km, 0.1 km, 0.1 km, 0.2 km, and 0.1 km, respectively. The difference in effective

skywave reflection height between the linear model and nonlinear model is shown in Figure 5-6. The shape of increased skywave penetration closely represents that of the change in conductivity as a function of electric field shown in Figure 5-2. Note that the y-axis is inverted in Figure 5-2 in order to highlight this effect. There is a large increase in skywave penetration at low return stroke peak currents and the rate of penetration increase levels off at higher return stroke peak currents.

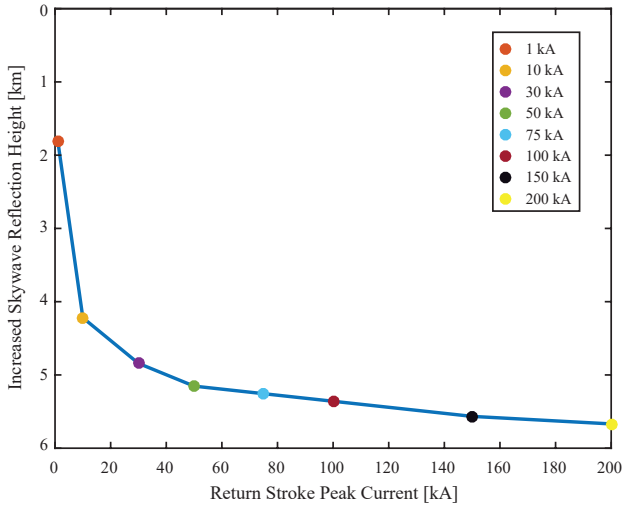

Figure 5-6. Relative increase of effective skywave reflection height in the nonlinear model versus linear model at 250 km from the lightning channel as a function of return stroke peak current.

The normalized electric field skywave peak shown on the right of 5-5 decreases monotonically as the return stroke peak current increases. There is a large decrease in the normalized electric field skywave peak between linear and 1 kA and a decrease continues consistently up to 200 kA. As the conductivity of the ionosphere decreases, the collision frequency increases. Therefore, as the return stroke peak current increases, it causes the heated ionospheric conductivity to decrease and collision frequency to increase. The increased collision frequency results in increased absorption of the skywave waveform for higher return stroke peak currents.

5.3.3 Dependence on Ambient Profile

Electron density profile I shown in Figure 3-4 has been used throughout this work. There are two more electron density profiles (II and III) which are both more dense than profile I. The denser profiles are expected to increase the conductivity of the ionosphere and therefore lower the effective skywave reflection height.

Figure 5-7 shows the effect on effective skywave reflection height due to the ambient electron density profile. The vertical electric field is recorded at 250 km with a 100 kA return stroke peak current. For profile I, the linear and nonlinear models have effective skywave reflection heights of 92.4 km and 97.8 km respectively with a difference of 5.4 km. For profile II, the linear and nonlinear models have effective skywave reflection heights of 88.9 km and 97.0 km respectively with a difference of 8.1 km. For profile III, the linear and nonlinear models have effective skywave reflection heights of 85.1 km and 90.6 km respectively with a difference of 5.5 km.

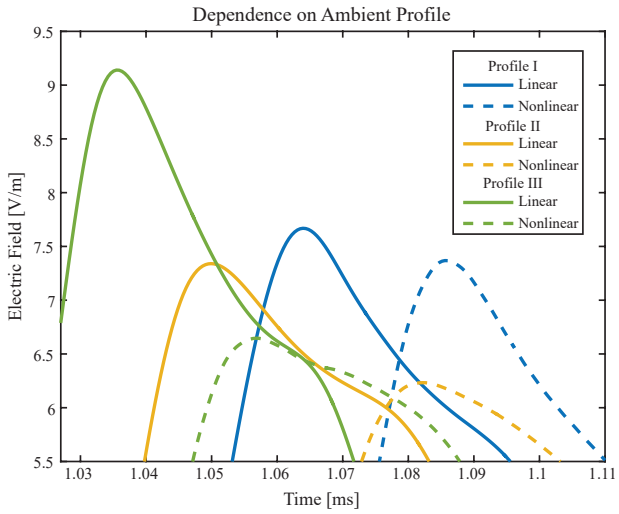

Figure 5-7. For two ambient profiles, vertical electric field of the skywave for the linear version and nonlinear (T_e and N_e) version.

As the electron density profile becomes more dense, the effective skywave reflection height for the linear and nonlinear models decreases. There is a 7.3 km decrease in effective skywave reflection height between the linear models utilizing profile I and profile III. The increased penetration in the nonlinear models for ambient electron density profiles I and III are similar at

5.4 km and 5.5 km respectively. Interestingly, the increased penetration in the nonlinear model for ambient profile II is significantly larger at 8.1 km. It is seen that the skywave penetrates deeper into the ionosphere across a range of electron density profiles in the nonlinear model versus linear model.

5.3.4 Dependence on Calculation Method

The relative timing between the peak of the groundwave to the peak of the skywave known as the peak-to-peak method has been used throughout this work to determine effective skywave reflection heights. Two other popular methods are the relative timing between the start of the groundwave defined here as 5% of the groundwave peak and the slow/fast breakpoints. The slow/fast breakpoints were originally defined in *McDonald et al.* [1979] and were first used to calculate ionospheric reflection heights by *Schonland et al.* [1940] and *Kinzer* [1974] for each breakpoint, respectively, and more recently used by *Carvalho et al.* [2017]. The location of the slow/fast breakpoints are labeled on the bottom left panel of Figure 5-8. Because the fast breakpoint occurs after the slow breakpoint thus increasing the relative time delay from the start of the groundwave, the fast breakpoint method will always calculate a higher effective skywave reflection height. In this work the slow breakpoint is defined as 5% of the fast breakpoint peak.

As the observation distance increases from the return stroke location, the waveforms of the groundwave and skywaves begin to overlap substantially. This effect is clearly visible in the top panels of Figure 5-8 which show the vertical electric field at 250 km and 750 km of both the groundwaves and skywaves. At 250 km the slow and fast breakpoints can be well-estimated, but at 750 km, the groundwave and skywave begin to overlap substantially. In order to properly determine effective skywave reflection height using the slow/fast breakpoints, the groundwave and skywave need to be completely separated from each other. A lightning return stroke was simulated in a larger all free-space grid in order to record the pure groundwave. The groundwave only portion of the lightning return stroke is shown in the middle panels of Figure 5-8. It is noted that the magnitude of the groundwave

Table 5-1. Method Based Reflection Height*

	250 km		
	Linear	Nonlinear	Diff
SB	78.1	83.6	5.5
FB	86.2	91.9	5.7
PtP	92.4	97.8	5.4

*All heights are in kilometers

is larger than experimentally observed groundwaves due to the use of a perfectly conducting ground instead of a realistic lossy ground [*Aoki et al.*, 2015]. The groundwave magnitude does not affect the results presented here since the relative timing of the groundwave peak and features are of interest. Now that the groundwave is fully known, it can be subtracted from the combined electric field (top panels) to leave only the skywave waveform which is shown in the bottom panels of Figure 5-8. The slow/fast breakpoints are clearly distinguishable now. Additional multi-hop skywaves can also be seen at both distances. It is noted that to compare experimental observations to simulation results at propagation distances of 750 km from the lightning channel, the curvature of the earth needs to be accounted for in the simulation and calculation of the skywave effective reflection height.

Calculating the effective skywave reflection heights at 250 km (left half of Figure 5-8) for the nonlinear model, the slow breakpoint method calculates a height of 83.6 km, the fast breakpoint method of 91.9 km and the peak-to-peak method of 97.8 km

The slow/fast breakpoint methods are now applied to the linear model. For the 250 km observation point, the slow breakpoint method calculates a height of 78.1 km, the fast breakpoint method of 86.2 km and the peak-to-peak method of 92.4 km. The skywave effective reflection heights for the linear and nonlinear models at 250 km are tabulated in Table 5-1. Included is also the difference between the two models for each calculation method.

It is clear that the method used to calculate effective skywave reflection height has a strong impact on the calculated reflection height. There is a 15 km range between the methods for the calculated skywave effective reflection height at the 250 km observation distance. The slow breakpoint method calculates the lowest skywave effective reflection height,

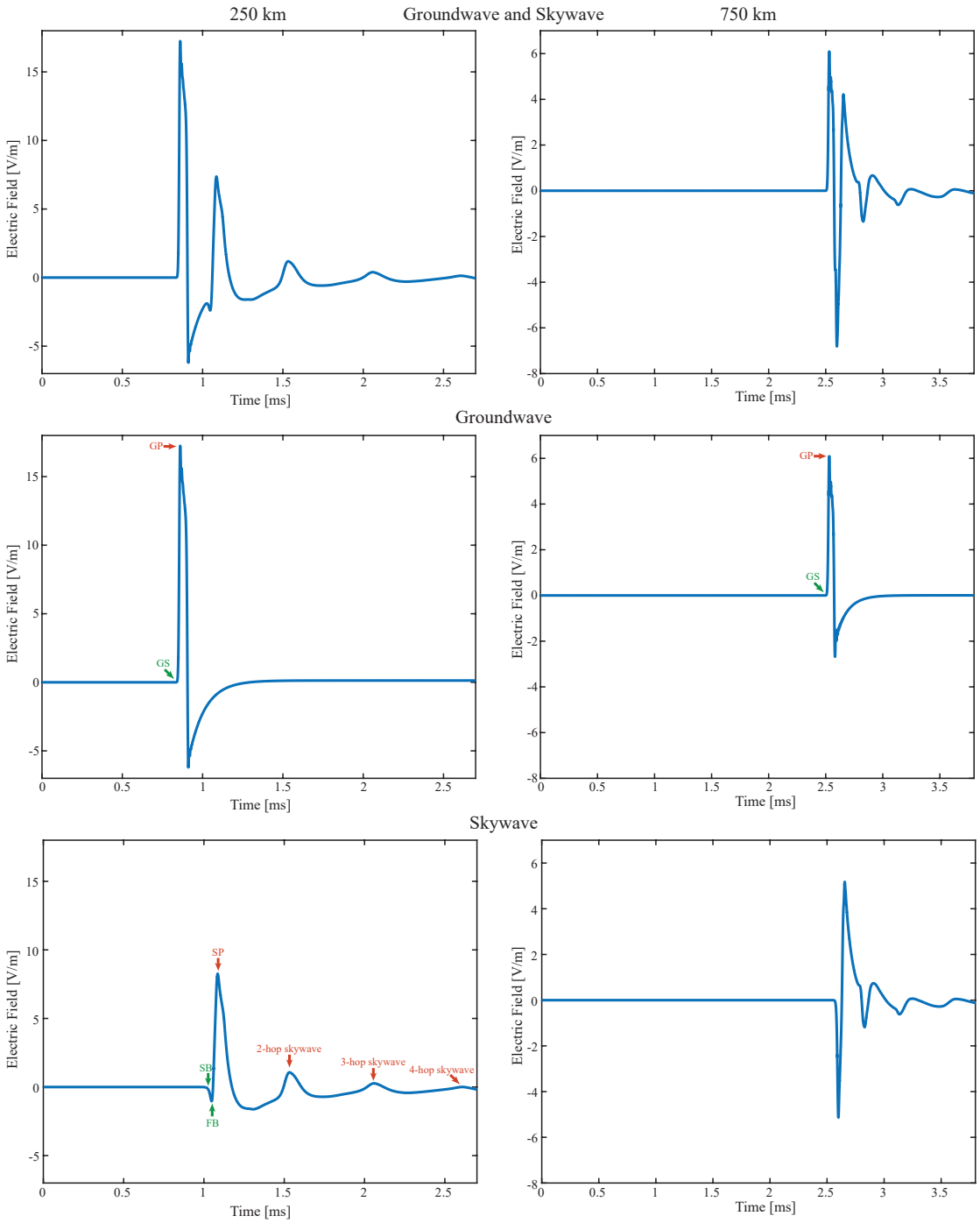

Figure 5-8. At 250 km and 750 km from the lightning return stroke for the nonlinear model, (top) the vertical electric field including the groundwave and skywave, (middle) the vertical electric field of the groundwave, and (bottom) the vertical electric field of the skywaves. GS: groundwave start, GP: groundwave peak, SB: slow breakpoint, FB: fast breakpoint, SP: skywave peak.

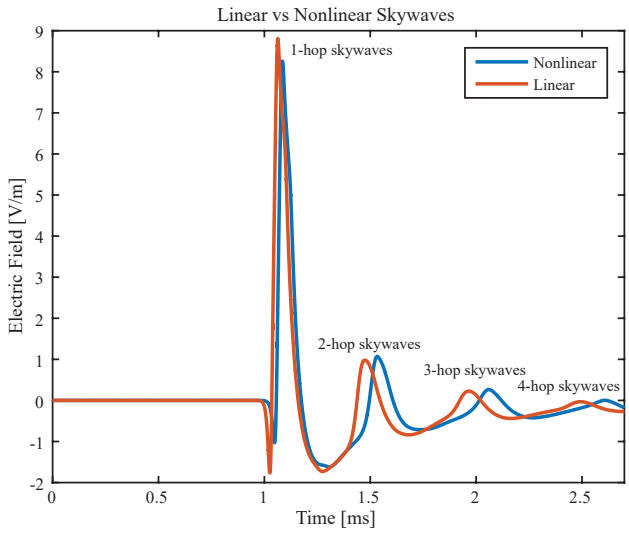

Figure 5-9. The vertical electric field of the skywaves (groundwave removed) for the linear and nonlinear models recorded at 250 km from the lightning return stroke. It can be seen that the entire nonlinear skywave waveform is delayed in time compared to that of the linear model.

the fast breakpoint is in the middle, and the peak-to-peak method calculates the highest reflection height. Regardless of the method used, it has been shown that skywaves reflect from a higher altitude in the nonlinear simulations than in the linear. For the simulation conditions shown here, the skywave from a 100 kA peak return stroke lightning flash penetrates ~5.5 km deeper into the ionosphere in the nonlinear model at 250 km. The increased penetration can further be seen in Figure 5-9 which shows the skywaves for the linear and nonlinear models at 250 km for a 100 kA return stroke peak current. There is a visible delay in the entire time-domain waveform of the skywaves for the nonlinear simulation in comparison with the linear simulation. Additionally, this time delay tends to grow with the multi-hop skywaves.

5.4 Frequency Dependent Reflection Height

A lightning skywave has most of its power in the ELF and VLF range as the higher frequencies either penetrate through the ionosphere or are highly attenuated. This can be seen in Figure 5-10 which shows the magnitude spectrum of the skywaves and groundwave recorded 250 km away from a 100 kA return stroke peak current using the nonlinear model and linear model. The groundwaves spectral content is visibly larger in magnitude than the skywaves.

Additionally, the groundwave shows strong nulls (20 dB weaker) every ~20 kHz with the first null at 20 kHz. These nulls result from the negating field previously discussed in the context of the lightning channel model. Ideally, this second field would not be included. In general, the spectral content of the groundwave decreases in magnitude as the frequency increases.

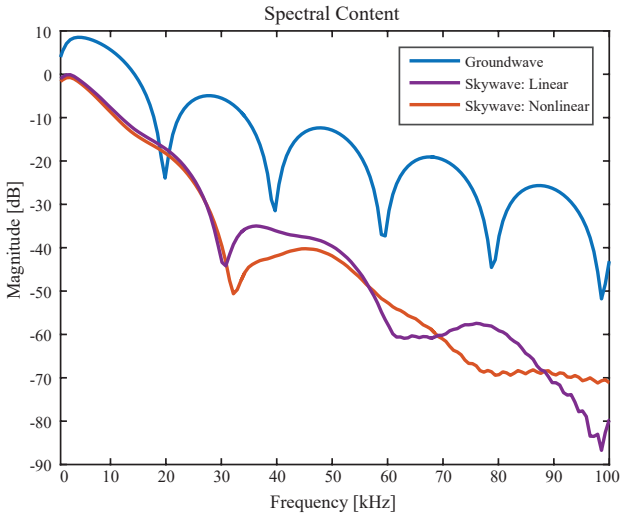

Figure 5-10. The spectra of the groundwave and 1-hop skywave recorded at 250 km for the nonlinear model and a 100 kA return stroke.

For the skywaves, the spectral content of the linear model is generally slightly larger in magnitude than the nonlinear model. The linear model has a first strong null at 30 kHz whereas the nonlinear model has a first null at 33 kHz. Similar to the ground wave, the spectral content of the skywaves decreases with increasing frequency. The magnitude of the spectral content decreases faster as the frequency increases for the skywaves than for the groundwave. Starting at ~60 kHz and higher in frequency, the skywaves spectral content appears to include numerical noise.

The ionospheric plasma is a highly dispersive medium causing all frequencies to reflect at a different altitude [*Westcott*, 1962a,b]. The calculations of skywave effective reflection height presented so far in this work have not been frequency dependent, but instead based on certain characterizations of the groundwave and skywave waveforms. By using the frequency domain it is possible to calculate the frequency based reflection height. In order to do this, the groundwave and skywave are first separated as shown in Section 5.3.4. Then the Fast

Fourier Transform (FFT) of the skywave is divided by the FFT of the groundwave. Next the negative change in phase per frequency is calculated, $-\frac{\partial \phi}{\partial f}$, which is then divided by 2π. This results in a time delay as a function of frequency. This time delay is then used in the standard triangularization method to calculate skywave reflection heights.

The skywave reflection height as a function of frequency is shown in Figure 5-11. This is for the same 100 kA peak return stroke recorded 250 km from the lightning return stroke as shown in Section 5.3.4. As has been shown to be expected, the nonlinear model calculates a higher effective skywave reflection height across the entire frequency spectrum shown (1 to 100 kHz). The difference between the nonlinear and linear reflection heights are on average between 4 and 7 km across the frequency spectrum which aligns with the difference calculated by the slow/fast breakpoints and peak-to-peak methods at this distance.

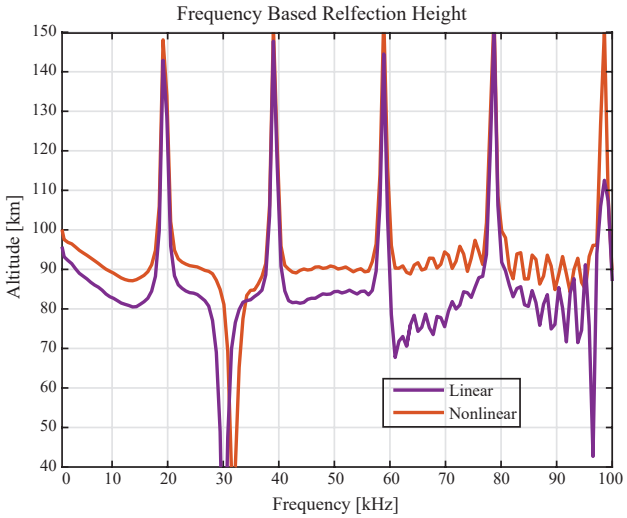

Figure 5-11. The effective skywave reflection height as a function of frequency for the linear and nonlinear models recorded at 250 km from the lightning return stroke.

There are sharp increases in the reflection height for both the linear and nonlinear models around ~19 kHz, ~39 kHz, ~59 kHz, ~79 kHz, and ~99 kHz, which correspond to the nulls seen in the groundwave spectrum shown in Figure 5-10. The frequency based reflection height is not valid at these peak locations and for ~1.5 kHz on either side. There is a sharp decrease in reflection height for the linear model at 30 kHz and nonlinear model at 33 kHz which correspond to the nulls seen in the spectra of the skywaves at each frequency, respectively. A

relatively stable reflection height is seen between 41 kHz and 58 kHz with a reflection height of ~90 km for the nonlinear model and 81.5 km to 84.5 km for the linear model. Numerical noise beyond 60 kHz causes significant oscillations in the reflection heights for both models.

It can be seen from the highly frequency dependent reflection heights that it is not possible to determine a single, distinct skywave reflection height due to the highly dispersive ionospheric plasma. Of course, accounting for the negating field in the ground wave might help address this issue. For example, between 1 and 16 kHz, both the linear and nonlinear models demonstrate a 13 km range in calculated reflection heights. Instead, the spectra of an experimentally observed lightning skywave can be compared to the spectra of a simulated skywave. By simulating lightning skywave propagation using a range of electron density altitude profiles, the electron density profile at the time of experimental observations can then be deduced by best fitting the two spectra such as in the work of *Hu and Cummer* [2006]; *Han and Cummer* [2010a,b]. Due to the increased skywave penetration into the ionosphere seen in the nonlinear models used in this chapter, it is suggested that nonlinear models including electron heating are utilized for future skywave analysis.

CHAPTER 6
SUMMARY AND SUGGESTIONS FOR FUTURE WORK

6.1 Summary of Contributions

In this dissertation, we have simulated and investigated nonlinear interactions in the D-region ionosphere produced by high-power radio waves from VLF and HF transmitters and lightning, and have compared the simulations to experimental observations.

The FDTD method was first investigated for a linear cold plasma. Five different linear cold plasma FDTD methods were presented which were discretized using the Möbius transformation. It was found that by using the Möbius transformation that all five methods maintained the same stability conditions as free space. Additionally, the Möbius transformation was found to create methods that very accurately model the cold plasma, as shown by excellent agreement with analytical solutions. All five methods had a wide range in terms of memory requirements and computational speed.

Method 2, was used as the foundation to create a 1-D nonlinear HF heating model of the D-region ionosphere. Numerical simulations were run of HF cross-modulation and excellent agreement was seen between numerical results and experimental observations. The thermal cubic nonlinearity was simulated and it was predicted that the frequency with the largest generated magnitude is around 5 kHz for the ambient profiles used. Additionally, the dominant mechanism found for the thermal cubic nonlinearity in polar regions was determined to be a mixing of the collision frequency at $|\omega_2 - \omega_1|$ with the plasma current density at ω_1 producing a radiated wave at $|\omega_2 - 2\omega_1|$, in confirmation of the work of *Moore et al.* [2013] and in contrast to the work of *Gurevich* [1978] and *Kotik and Ermakova* [1998].

The 1^{st}- and 2^{nd}-order moments of the Boltzmann Equation derived including the convective derivative were presented and analyzed in Chapter 4 at VLF frequencies. The 6 additional terms present in the 1^{st}-order moment of the Boltzmann Equation were found to potentially contribute detectably to the plasma current density at VLF frequencies. The 1^{st}-order moment was also found to have an impact on the peak electron temperature. For

the 2^{nd}-order moment, it was found that the first term, the Joule heating term, is the most important for determining the change in electron temperature in the D-region ionosphere. The additional terms in the 2^{nd}-order moment derived including the convective derivative version versus without the convective derivative were found to have a minimal impact on electron temperature at VLF frequencies. Other modulation formats and their effect on these conclusions were not explored.

The effect of nonlinear interactions on lightning skywave effective reflection height was investigated in Chapter 5. It was found that skywaves penetrate deeper into the ionosphere in the nonlinear model versus the linear model. Electron density changes were found to have a minimal impact and electron heating was shown to have a significant impact on skywave propagation. Electron heating was seen to be important for all return stroke peak currents, even those as little as 1 kA to 10 kA. At lower return stroke peak currents, the increased penetration was shown to increase rapidly. The change in increased penetration then leveled off at higher return stroke peak currents, in conjunction with the leveling off of the heated conductivity of the ionosphere. Effective skywave reflection height was analyzed as a function of frequency and it was shown that all frequencies simulated here demonstrated deeper penetration in the nonlinear model versus linear model.

6.2 Suggestions for Future Research

The numerical models presented in this dissertation are some of the newest, most advanced models presently for simulating heating of the D-region ionosphere. There are still ways that these models could be improved in order to more accurately simulate the real world and shed more light on the nonlinear processes involved. Most of the suggestions listed below are currently limited by computer computation speed and memory requirements, especially for the HF simulations.

6.2.1 Improved HF Heating Model

We first recommend an extension of the 1-D nonlinear HF heating model presented in Chapter 3 to 3-D. A second improvement on this model is the inclusion of a DC current

to represent the auroral electrojet. These improvements will provide a number of enhanced features for this model. The first is by being in 3-D, more accurate beam patterns from HF transmitters such as HAARP are able to be modeled. This will allow for FDTD simulations and further investigation of the phasing effect seen at HAARP when splitting the array in North/South versus East/West configurations. By including the auroral electrojet, ELF/VLF wave generation experiments can be directly simulated that rely on the electrojet. Furthermore, beam-painting and geometric modulation are able to be investigated in 3-D with the electrojet.

The next improvement for the HF heating model is to expand the model through the D- region up into the E-region (100 to 150 km) and parts of the F-region (150 to 1000 km) ionosphere. There are lots of E- and F-region experiments such as those by *Papadopoulos et al.* [2011a,b] which would benefit and be more understood from an improved FDTD modeling effort.

6.2.2 Improved Lightning Model

The lightning heating model of Chapter 5 provided excellent results, but could easily be improved upon. The biggest improvement would be to simulate the earth's magnetic field. In order to do this at arbitrary angles, the 2-D cylindrical model needs to be upgraded to either 3-D Cartesian or ideally 3-D spherical. A 3-D spherical model would naturally account for earth's curvature, which is important for skywaves propagating past a few hundred kilometers. Another improvement would be a reduction in grid size of this model. This would allow the rise-time and recovery of the lightning return stroke to be reduced to more realistic values. This in turn means that higher frequencies above 100 kHz would also be able to be modeled.

Another major improvement would be improved modeling of the groundwave. A first step to do this is to utilize a lightning channel model that did not have the negating field present above the the lightning channel. This would create a more realistic groundwave spectra than that shown in Figure 5-10 and would remove the sharp peaks seen in the frequency based reflection height seen in Figure 5-11. Another step to improve the groundwave is to include

a lossy ground to accurately recreate the groundwave magnitude at far distances [*Aoki et al.*, 2015].

Another potential use of this model is an investigation of the electric and magnetic field that makes it to the top of the D-region ionosphere in a linear versus nonlinear model. This will allow insight into how much wave energy is injected into the magnetosphere which is important for Lightning-Induced Electron Precipitation (LEP). Simulations can be compared with satellite measurements.

6.2.3 Moments of the Boltzmann Equation: VLF and HF

The 1^{st}- and 2^{nd}-order moments of the Boltzmann Equation derived including the convective derivative were analyzed in 3-D for a broadside VLF source at 30 km altitude. To represent a Navy VLF transmitter, a vertical monopole transmitter should be simulated. This source will require a larger grid size due to the radiation pattern. Also, CW VLF heating was simulated. Additional effects may be observed and certain terms may become more important for other VLF modulation schemes and VLF heating experiments.

Furthermore, different terms in the moments of the Boltzmann Equation may become more or less important at HF frequencies and an investigation into this is needed. It is expected that the moments of the Boltzmann Equation derived including the convective derivative at HF will be important for HF heating experiments and especially in forming self-focusing pressure bubbles. A 3-D HF heating model is needed to investigate these effects.

APPENDIX
LINEAR METHOD UPDATE COEFFICIENTS

The update coefficient matrices for Linear Method 2 are:

$$A = \begin{bmatrix} \frac{\epsilon_o}{\Delta t^2} + \frac{\epsilon_o \nu}{2\Delta t} + \frac{q_e^2 N_e}{4\Delta t^0 m_e} & -\frac{\epsilon_o q_e}{m_e}\frac{\vec{B}_{oz}}{2\Delta t} & \frac{\epsilon_o q_e}{m_e}\frac{\vec{B}_{oy}}{2\Delta t} \\ \frac{\epsilon_o q_e}{m_e}\frac{\vec{B}_{oz}}{2\Delta t} & \frac{\epsilon_o}{\Delta t^2} + \frac{\epsilon_o \nu}{2\Delta t} + \frac{q_e^2 N_e}{4\Delta t^0 m_e} & -\frac{\epsilon_o q_e}{m_e}\frac{\vec{B}_{ox}}{2\Delta t} \\ \frac{\epsilon_o q_e}{m_e}\frac{\vec{B}_{oy}}{2\Delta t} & \frac{\epsilon_o q_e}{m_e}\frac{\vec{B}_{ox}}{2\Delta t} & \frac{\epsilon_o}{\Delta t^2} + \frac{\epsilon_o \nu}{2\Delta t} + \frac{q_e^2 N_e}{4\Delta t^0 m_e} \end{bmatrix} \tag{A-1}$$

$$B = \begin{bmatrix} \frac{2\epsilon_o}{\Delta t^2} - \frac{2q_e^2 N_e}{4\Delta t^0 m_e} & 0 & 0 \\ 0 & \frac{2\epsilon_o}{\Delta t^2} - \frac{2q_e^2 N_e}{4\Delta t^0 m_e} & 0 \\ 0 & 0 & \frac{2\epsilon_o}{\Delta t^2} - \frac{2q_e^2 N_e}{4\Delta t^0 m_e} \end{bmatrix} \tag{A-2}$$

$$C = \begin{bmatrix} -\frac{\epsilon_o}{\Delta t^2} + \frac{\epsilon_o \nu}{2\Delta t} - \frac{q_e^2 N_e}{4\Delta t^0 m_e} & -\frac{\epsilon_o q_e}{m_e}\frac{\vec{B}_{oz}}{2\Delta t} & \frac{\epsilon_o q_e}{m_e}\frac{\vec{B}_{oy}}{2\Delta t} \\ -\frac{\epsilon_o q_e}{m_e}\frac{\vec{B}_{oz}}{2\Delta t} & \frac{\epsilon_o}{\Delta t^2} + \frac{\epsilon_o \nu}{2\Delta t} - \frac{q_e^2 N_e}{4\Delta t^0 m_e} & -\frac{\epsilon_o q_e}{m_e}\frac{\vec{B}_{ox}}{2\Delta t} \\ \frac{\epsilon_o q_e}{m_e}\frac{\vec{B}_{oy}}{2\Delta t} & \frac{\epsilon_o q_e}{m_e}\frac{\vec{B}_{ox}}{2\Delta t} & -\frac{\epsilon_o}{\Delta t^2} + \frac{\epsilon_o \nu}{2\Delta t} - \frac{q_e^2 N_e}{4\Delta t^0 m_e} \end{bmatrix} \tag{A-3}$$

$$F = \begin{bmatrix} \frac{1}{\Delta t^2} + \frac{\nu}{2\Delta t} & -\frac{q_e}{m_e}\frac{\vec{B}_{oz}}{2\Delta t} & \frac{q_e}{m_e}\frac{\vec{B}_{oy}}{2\Delta t} \\ \frac{q_e}{m_e}\frac{\vec{B}_{oz}}{2\Delta t} & \frac{1}{\Delta t^2} + \frac{\nu}{2\Delta t} & -\frac{q_e}{m_e}\frac{\vec{B}_{ox}}{2\Delta t} \\ -\frac{q_e}{m_e}\frac{\vec{B}_{oy}}{2\Delta t} & \frac{q_e}{m_e}\frac{\vec{B}_{ox}}{2\Delta t} & \frac{1}{\Delta t^2} + \frac{\nu}{2\Delta t} \end{bmatrix} \tag{A-4}$$

$$G = \begin{bmatrix} -\frac{2}{\Delta t^2} & 0 & 0 \\ 0 & -\frac{2}{\Delta t^2} & 0 \\ 0 & 0 & -\frac{2}{\Delta t^2} \end{bmatrix} \tag{A-5}$$

$$H = \begin{bmatrix} \frac{1}{\Delta t^2} - \frac{\nu}{2\Delta t} & \frac{q_e}{m_e}\frac{\vec{B}_{oz}}{2\Delta t} & -\frac{q_e}{m_e}\frac{\vec{B}_{oy}}{2\Delta t} \\ -\frac{q_e}{m_e}\frac{\vec{B}_{oz}}{2\Delta t} & \frac{1}{\Delta t^2} - \frac{\nu}{2\Delta t} & \frac{q_e}{m_e}\frac{\vec{B}_{ox}}{2\Delta t} \\ \frac{q_e}{m_e}\frac{\vec{B}_{oy}}{2\Delta t} & -\frac{q_e}{m_e}\frac{\vec{B}_{ox}}{2\Delta t} & \frac{1}{\Delta t^2} - \frac{\nu}{2\Delta t} \end{bmatrix} \tag{A-6}$$

The update coefficient scalars and matrices for Linear Method 3 are:

$$q = \frac{1}{\epsilon_o}\left(\frac{1}{\Delta t^4} + \frac{3\nu}{2\Delta t^3} + \frac{3\nu + \omega_c^2}{4\Delta t^2}\frac{\nu^3 + \nu\omega_c^2}{8\Delta t}\right) \tag{A-7}$$

$$r = -\frac{1}{\epsilon_o}\left(\frac{4}{\Delta t^4} + \frac{3\nu}{\Delta t^3} - \frac{\nu^3 + \nu\omega_c^2}{4\Delta t^1}\right) \tag{A-8}$$

$$s = \frac{1}{\epsilon_o}\left(\frac{6}{\Delta t^4} - \frac{3\nu^2 + \omega_c^2}{2\Delta t^2}\right) \tag{A-9}$$

$$t = -\frac{1}{\epsilon_o}\left(\frac{4}{\Delta t^4} - \frac{3\nu}{\Delta t^3} + \frac{\nu^3 + \nu\omega_c^2}{4\Delta t^1}\right) \tag{A-10}$$

$$u = \frac{1}{\epsilon_o}\left(\frac{1}{\Delta t^4} - \frac{3\nu}{2\Delta t^3} + \frac{3\nu^2 + \omega_c^2}{4\Delta t^2} - \frac{\nu^3 + \nu\omega_c^2}{8\Delta t^1}\right) \tag{A-11}$$

$$K = \begin{bmatrix} \frac{1}{\Delta t^4}+\frac{3\nu}{2\Delta t^3}+\frac{3\nu^2+\omega_c^2+\omega_p^2}{4\Delta t^2}+\frac{\nu^3+\nu\omega_c^2+2\nu\omega_p^2}{8\Delta t^1}+\frac{\nu^2\omega_p^2+\omega_{cx}^2\omega_p^2}{16} & \frac{(\omega_{cx}\omega_{cy}-\nu\omega_{cz})\omega_p^2}{16}-\frac{\omega_{cz}\omega_p^2}{8\Delta t} & \frac{(\omega_{cx}\omega_{cz}+\nu\omega_{cy})\omega_p^2}{16}+\frac{\omega_{cy}\omega_p^2}{8\Delta t} \\ \frac{(\omega_{cx}\omega_{cy}+\nu\omega_{cz})\omega_p^2}{16}+\frac{\omega_{cz}\omega_p^2}{8\Delta t} & \frac{1}{\Delta t^4}+\frac{3\nu}{2\Delta t^3}+\frac{3\nu^2+\omega_c^2+\omega_p^2}{4\Delta t^2}+\frac{\nu^3+\nu\omega_c^2+2\nu\omega_p^2}{8\Delta t^1}+\frac{\nu^2\omega_p^2+\omega_{cy}^2\omega_p^2}{16} & \frac{(\omega_{cy}\omega_{cz}-\nu\omega_{cx})\omega_p^2}{16}+\frac{\omega_{cx}\omega_p^2}{8\Delta t} \\ \frac{(\omega_{cx}\omega_{cz}-\nu\omega_{cy})\omega_p^2}{16}-\frac{\omega_{cy}\omega_p^2}{8\Delta t} & \frac{(\omega_{cy}\omega_{cz}+\nu\omega_{cx})\omega_p^2}{16}+\frac{\omega_{cx}\omega_p^2}{8\Delta t} & \frac{1}{\Delta t^4}+\frac{3\nu}{2\Delta t^3}+\frac{3\nu^2+\omega_c^2+\omega_p^2}{4\Delta t^2}+\frac{\nu^3+\nu\omega_c^2+2\nu\omega_p^2}{8\Delta t^1}+\frac{\nu^2\omega_p^2+\omega_{cz}^2\omega_p^2}{16} \end{bmatrix} \tag{A-12}$$

$$L = \begin{bmatrix} \frac{4}{\Delta t^4}+\frac{3\nu}{\Delta t^3}-\frac{\nu^3+\nu\omega_c^2+2\nu\omega_p^2}{4\Delta t}-\frac{\omega_{cx}^2\omega_p^2+\nu^2\omega_p^2}{4} & \frac{\omega_{cz}\omega_p^2}{4\Delta t}+\frac{\nu\omega_{cz}\omega_p^2-\omega_{cx}\omega_{cy}\omega_p^2}{4} & -\frac{\omega_{cy}\omega_p^2}{4\Delta t}-\frac{\nu\omega_{cy}\omega_p^2+\omega_{cx}\omega_{cz}\omega_p^2}{4} \\ -\frac{\omega_{cz}\omega_p^2}{4\Delta t}-\frac{\nu\omega_{cz}\omega_p^2+\omega_{cx}\omega_{cy}\omega_p^2}{4} & \frac{4}{\Delta t^4}+\frac{3\nu}{\Delta t^3}-\frac{\nu^3+\nu\omega_c^2+2\nu\omega_p^2}{4\Delta t}-\frac{\omega_{cy}^2\omega_p^2+\nu^2\omega_p^2}{4} & \frac{\omega_{cx}\omega_p^2}{4\Delta t}+\frac{\nu\omega_{cx}\omega_p^2-\omega_{cy}\omega_{cz}\omega_p^2}{4} \\ \frac{\omega_{cy}\omega_p^2}{4\Delta t}+\frac{\nu\omega_{cy}\omega_p^2-\omega_{cx}\omega_{cz}\omega_p^2}{4} & -\frac{\omega_{cx}\omega_p^2}{4\Delta t}+\frac{\nu\omega_{cx}\omega_p^2-\omega_{cy}\omega_{cz}\omega_p^2}{4} & \frac{4}{\Delta t^4}+\frac{3\nu}{\Delta t^3}-\frac{\nu^3+\nu\omega_c^2+2\nu\omega_p^2}{4\Delta t}-\frac{\omega_{cz}^2\omega_p^2+\nu^2\omega_p^2}{4} \end{bmatrix} \tag{A-13}$$

$$M = \begin{bmatrix} -\frac{6}{\Delta t^4}+\frac{3\nu^2+\omega_c^2+\omega_p^2}{2\Delta t^2}-\frac{3\omega_{cx}^2\omega_p^2+3\nu^2\omega_p^2}{8} & \frac{3\nu\omega_{cz}\omega_p^2-3\omega_{cx}\omega_{cy}\omega_p^2}{8} & \frac{3\nu\omega_{cy}\omega_p^2-3\omega_{cx}\omega_{cz}\omega_p^2}{8} \\ -\frac{3\nu\omega_{cz}\omega_p^2+3\omega_{cx}\omega_{cy}\omega_p^2}{8} & -\frac{6}{\Delta t^4}+\frac{3\nu^2+\omega_c^2+\omega_p^2}{2\Delta t^2}-\frac{3\omega_{cy}^2\omega_p^2+3\nu^2\omega_p^2}{8} & \frac{3\nu\omega_{cx}\omega_p^2-3\omega_{cy}\omega_{cz}\omega_p^2}{8} \\ \frac{3\nu\omega_{cy}\omega_p^2-3\omega_{cx}\omega_{cz}\omega_p^2}{8} & \frac{3\nu\omega_{cx}\omega_p^2-3\omega_{cy}\omega_{cz}\omega_p^2}{8} & -\frac{6}{\Delta t^4}+\frac{3\nu^2+\omega_c^2+\omega_p^2}{2\Delta t^2}-\frac{3\omega_{cz}^2\omega_p^2+3\nu^2\omega_p^2}{8} \end{bmatrix} \tag{A-14}$$

$$N = \begin{bmatrix} \frac{4}{\Delta t^4}-\frac{3\nu}{\Delta t^3}+\frac{\nu^3+\nu\omega_c^2+2\nu\omega_p^2}{4\Delta t}+\nu^2\omega_p^2-\omega_{cx}^2\omega_p^24 & -\frac{\omega_{cz}\omega_p^2}{4\Delta t}+\frac{\nu\omega_{cz}\omega_p^2-\omega_{cx}\omega_{cy}\omega_p^2}{4} & \frac{\omega_{cy}\omega_p^2}{4\Delta t}-\frac{\nu\omega_{cy}\omega_p^2+\omega_{cx}\omega_{cz}\omega_p^2}{4} \\ \frac{\omega_{cz}\omega_p^2}{4\Delta t}-\frac{\nu\omega_{cz}\omega_p^2+\omega_{cx}\omega_{cy}\omega_p^2}{4} & \frac{4}{\Delta t^4}-\frac{3\nu}{\Delta t^3}+\frac{\nu^3+\nu\omega_c^2+2\nu\omega_p^2}{4\Delta t}+\nu^2\omega_p^2-\omega_{cy}^2\omega_p^24 & -\frac{\omega_{cx}\omega_p^2}{4\Delta t}+\frac{\nu\omega_{cx}\omega_p^2-\omega_{cy}\omega_{cz}\omega_p^2}{4} \\ -\frac{\omega_{cy}\omega_p^2}{4\Delta t}+\frac{\nu\omega_{cy}\omega_p^2-\omega_{cx}\omega_{cz}\omega_p^2}{4} & \frac{\omega_{cx}\omega_p^2}{4\Delta t}-\frac{\nu\omega_{cx}\omega_p^2+\omega_{cy}\omega_{cz}\omega_p^2}{4} & \frac{4}{\Delta t^4}-\frac{3\nu}{\Delta t^3}+\frac{\nu^3+\nu\omega_c^2+2\nu\omega_p^2}{4\Delta t}+\nu^2\omega_p^2-\omega_{cz}^2\omega_p^24 \end{bmatrix} \tag{A-15}$$

$$P = \begin{bmatrix} -\frac{1}{\Delta t^4}+\frac{3\nu}{2\Delta t^3}-\frac{3\nu^2+\omega_c^2+\omega_p^2}{4\Delta t^2}+\frac{\nu^3+\nu\omega_c^2+2\nu\omega_p^2}{8\Delta t}-\frac{\nu^2\omega_p^2+\omega_{cx}^2\omega_p^2}{16} & -\frac{\omega_{cz}\omega_p^2}{8\Delta t}+\frac{\nu\omega_{cz}\omega_p^2-\omega_{cx}\omega_{cy}\omega_p^2}{16} & \frac{\omega_{cy}\omega_p^2}{8\Delta t}-\frac{\nu\omega_{cy}\omega_p^2+\omega_{cx}\omega_{cz}\omega_p^2}{16} \\ \frac{\omega_{cz}\omega_p^2}{8\Delta t}-\frac{\nu\omega_{cz}\omega_p^2+\omega_{cx}\omega_{cy}\omega_p^2}{16} & -\frac{1}{\Delta t^4}+\frac{3\nu}{2\Delta t^3}-\frac{3\nu^2+\omega_c^2+\omega_p^2}{4\Delta t^2}+\frac{\nu^3+\nu\omega_c^2+2\nu\omega_p^2}{8\Delta t}-\frac{\nu^2\omega_p^2+\omega_{cy}^2\omega_p^2}{16} & -\frac{\omega_{cx}\omega_p^2}{8\Delta t}+\frac{\nu\omega_{cx}\omega_p^2-\omega_{cy}\omega_{cz}\omega_p^2}{16} \\ -\frac{\omega_{cy}\omega_p^2}{8\Delta t}+\frac{\nu\omega_{cy}\omega_p^2-\omega_{cx}\omega_{cz}\omega_p^2}{16} & \frac{\omega_{cx}\omega_p^2}{8\Delta t}-\frac{\nu\omega_{cx}\omega_p^2+\omega_{cy}\omega_{cz}\omega_p^2}{16} & -\frac{1}{\Delta t^4}+\frac{3\nu}{2\Delta t^3}-\frac{3\nu^2+\omega_c^2+\omega_p^2}{4\Delta t^2}+\frac{\nu^3+\nu\omega_c^2+2\nu\omega_p^2}{8\Delta t}-\frac{\nu^2\omega_p^2+\omega_{cz}^2\omega_p^2}{16} \end{bmatrix} \tag{A-16}$$

The update coefficients for Linear Method 5 assuming 1-D propagation and the background magnetic field is in the $\hat{z}$ direction are:

$$A = \begin{bmatrix} -\frac{\mu_0 q_e^2 N_e}{m_e}\frac{1}{4\Delta t^1} - \mu_0\epsilon_0\nu\frac{1}{2\Delta t^2} - \mu_0\epsilon_0\frac{1}{\Delta t^3} & \frac{q_e\mu_0\epsilon_0}{m_e}\frac{B_{0z}}{2\Delta t^2} \\ -\frac{q_e\mu_0\epsilon_0}{m_e}\frac{B_{0z}}{2\Delta t^2} & -\frac{\mu_0 q_e^2 N_e}{m_e}\frac{1}{4\Delta t^1} - \mu_0\epsilon_0\nu\frac{1}{2\Delta t^2} - \mu_0\epsilon_0\frac{1}{\Delta t^3} \end{bmatrix} \tag{A-17}$$

$$B = \begin{bmatrix} \frac{1}{(\Delta z)^2}\frac{2}{\Delta t^1} + \frac{\nu}{(\Delta z)^2} + \frac{\mu_0 q_e^2 N_e}{m_e}\frac{1}{4\Delta t^1} - \mu_0\epsilon_0\nu\frac{1}{2\Delta t^2} - \mu_0\epsilon_0\frac{1}{\Delta t^3} & -\frac{q_e}{m_e}\frac{B_{0z}}{(\Delta z)^2} + \frac{q_e\mu_0\epsilon_0}{m_e}\frac{B_{0z}}{2\Delta t^2} \\ \frac{q_e}{m_e}\frac{B_{0z}}{(\Delta z)^2} + \frac{q_e\mu_0\epsilon_0}{m_e}\frac{B_{0z}}{2\Delta t^2} & \frac{1}{(\Delta z)^2}\frac{2}{\Delta t^1} + \frac{\nu}{(\Delta z)^2} + \frac{\mu_0 q_e^2 N_e}{m_e}\frac{1}{4\Delta t^1} - \mu_0\epsilon_0\nu\frac{1}{2\Delta t^2} - \mu_0\epsilon_0\frac{1}{\Delta t^3} \end{bmatrix} \tag{A-18}$$

$$C = \begin{bmatrix} -\frac{1}{(\Delta z)^2}\frac{2}{\Delta t^1} + \frac{\nu}{(\Delta z)^2} - \frac{\mu_0 q_e^2 N_e}{m_e}\frac{1}{4\Delta t^1} - \mu_0\epsilon_0\nu\frac{1}{2\Delta t^2} + \mu_0\epsilon_0\frac{1}{\Delta t^3} & -\frac{q_e}{m_e}\frac{B_{0z}}{(\Delta z)^2} + \frac{q_e\mu_0\epsilon_0}{m_e}\frac{B_{0z}}{2\Delta t^2} \\ \frac{q_e}{m_e}\frac{B_{0z}}{(\Delta z)^2} + \frac{q_e\mu_0\epsilon_0}{m_e}\frac{B_{0z}}{2\Delta t^2} & -\frac{1}{(\Delta z)^2}\frac{2}{\Delta t^1} + \frac{\nu}{(\Delta z)^2} - \frac{\mu_0 q_e^2 N_e}{m_e}\frac{1}{4\Delta t^1} - \mu_0\epsilon_0\nu\frac{1}{2\Delta t^2} + \mu_0\epsilon_0\frac{1}{\Delta t^3} \end{bmatrix} \tag{A-19}$$

$$D = \begin{bmatrix} -\frac{\mu_0 q_e^2 N_e}{m_e}\frac{1}{4\Delta t^1} + \mu_0\epsilon_0\nu\frac{1}{2\Delta t^2} - \mu_0\epsilon_0\frac{1}{\Delta t^3} & -\frac{q_e\mu_0\epsilon_0}{m_e}\frac{B_{0z}}{2\Delta t^2} \\ \frac{q_e\mu_0\epsilon_0}{m_e}\frac{B_{0z}}{2\Delta t^2} & -\frac{\mu_0 q_e^2 N_e}{m_e}\frac{1}{4\Delta t^1} + \mu_0\epsilon_0\nu\frac{1}{2\Delta t^2} - \mu_0\epsilon_0\frac{1}{\Delta t^3} \end{bmatrix} \tag{A-20}$$

$$F = \begin{bmatrix} -\frac{1}{(\Delta z)^2}\frac{1}{\Delta t^1} - \frac{\nu}{2(\Delta z)^2} & \frac{q_e}{m_e}\frac{B_{0z}}{2(\Delta z)^2} \\ -\frac{q_e}{m_e}\frac{B_{0z}}{2(\Delta z)^2} & -\frac{1}{(\Delta z)^2}\frac{1}{\Delta t^1} - \frac{\nu}{2(\Delta z)^2} \end{bmatrix} \tag{A-21}$$

$$G = \begin{bmatrix} \frac{1}{(\Delta z)^2}\frac{1}{\Delta t^1} - \frac{\nu}{2(\Delta z)^2} & \frac{q_e}{m_e}\frac{B_{0z}}{2(\Delta z)^2} \\ -\frac{q_e}{m_e}\frac{B_{0z}}{2(\Delta z)^2} & \frac{1}{(\Delta z)^2}\frac{1}{\Delta t^1} - \frac{\nu}{2(\Delta z)^2} \end{bmatrix} \tag{A-22}$$

$$H = \begin{bmatrix} -\frac{1}{(\Delta z)^2}\frac{1}{\Delta t^1} - \frac{\nu}{2(\Delta z)^2} & \frac{q_e}{m_e}\frac{B_{0z}}{2(\Delta z)^2} \\ -\frac{q_e}{m_e}\frac{B_{0z}}{2(\Delta z)^2} & -\frac{1}{(\Delta z)^2}\frac{1}{\Delta t^1} - \frac{\nu}{2(\Delta z)^2} \end{bmatrix} \tag{A-23}$$

$$I = \begin{bmatrix} \frac{1}{(\Delta z)^2}\frac{1}{\Delta t^1} - \frac{\nu}{2(\Delta z)^2} & \frac{q_e}{m_e}\frac{B_{0z}}{2(\Delta z)^2} \\ -\frac{q_e}{m_e}\frac{B_{0z}}{2(\Delta z)^2} & \frac{1}{(\Delta z)^2}\frac{1}{\Delta t^1} - \frac{\nu}{2(\Delta z)^2} \end{bmatrix} \tag{A-24}$$

REFERENCES

Agrawal, D., and R. C. Moore (2012), Dual-beam ELF wave generation as a function of power, frequency, modulation waveform, and receiver location, *J. Geophys. Res.*, *117*, A12305, doi:10.1029/2012JA018061.

Aoki, M., Y. Baba, and V. A. Rakov (2015), FDTD simulationof LEMP propagation over lossy ground: influence of distance, ground conductivity, and source parameters, *J. Geophys. Res. Atmos.*, *120*, 8043–8051, doi:10.1002/2015JD023245.

Bailey, V. A., and D. F. Martyn (1934), Interaction of radio waves, *Nature*, *133*, 218, doi:10.1038/133218a0.

Barr, R. (1996), VLF wave generation using VLF heating and the cubic nonlinearity of the ionosphere, *Geophys. Res. Lett.*, *23*, 2165–2168, doi:10.1029/96GL02024.

Barr, R., and P. Stubbe (1991), ELF radiation from the Tromso "Super Heater" facility, *Geophys. Res. Lett.*, *18*, 1035–1038, doi:10.1029/91GL01156.

Barr, R., M. T. Rietveld, H. Kopka, P. Stubbe, and E. Nielsen (1985), Extra-low frequency radiation from the polar electrojet antenna, *Nature*, *317*, 155–157.

Barrington-Leigh, C. P. (2000), Fast photometric imaging of high altitude optical flashes above thunderstorms, (Doctoral dissertation). Stanford, CA: Stanford University.

Barrington-Leigh, C. P., and U. S. Inan (1999), Elves triggered by positive and negative lightning discharges, *Geophys. Res. Lett.*, *26*, 683–686, doi:10.1029/1999GL900059.

Barrington-Leigh, C. P., U. S. Inan, and M. Stanley (2001), Identification of sprites and elves with intensified video and broadband array photometry, *J. Geophys. Res.*, *106*, 1741–1750, doi:10.1029/2000JA000073.

Bittencourt, J. A. (2004), *Fundamentals of plasma physics*, 3rd ed., Springer-Verlag, New York.

Boeck, W. L., O. H. Vaughan Jr., R. J. Blakeslee, B. Vonnegut, and M. Brook (1992), Lightning induced brightening in the airglow layer, *Geophys. Res. Lett.*, *19*, 99–102, doi:10.1029/91GL03168.

Boeck, W. L., O. H. Vaughan Jr., R. J. Blakeslee, B. Vonnegut, M. Brook, and J. McKune (1995), Observations of lightning in the stratosphere, *J. Geophys. Res.*, *100*, 1465–1475, doi:10.1029/94JD02432.

Budden, K. G. (1985), *The propagation of radio waves*, Cambridge Univ. Press, New York.

Budden, K. G. (1988), "The ionosphere and magnetosphere," in *The propagation of radio waves: The theory of radio waves of low power in the ionosphere and magnetosphere*. Cambridge University Press, Cambridge, GBR.

Carvalho, F. L., M. A. Uman, D. M. Jordan, J. D. Hill, S. A. Cummer, D. A. Kotovsky, and R. C. Moore (2017), Triggered lightning sky waves, return stroke modeling, and ionosphere effective height, *J. Geophys. Res. Atmos.*, *122*, doi:10.1002/2016JD-26202.

Chapman, S. (1931), The absorption and dissociative or ionizing effect of monochromatic radiation in an atmosphere on a rotating earth, *Proc. Phys. Soc*, *43*, 26–45.

Chapman, S. (1931), The absorption and dissociative or ionizing effect of monochromatic radiation in an atmosphere on a rotating earth. Part II. Grazing incidence, *Proc. Phys. Soc*, *43*, 483–501.

Chapman, S. (1939), The atmospheric height distribution of band absorbed solar radiation, *Proc. Phys. Soc*, *51*, 93–109.

Cheng, Z., and S. Cummer (2005), Broadband VLF measurements of lightning-induced ionospheric perturbations, *Geophys. Res. Lett.*, *32*, L08804, doi:10.1029/2004GL022187.

Cohen, M. B., and M. Golkowski (2013), 100 days of ELF/VLF generation via HF heating with HAARP, *J. Geophys. Res. Space Phys.*, *118*, 6597–6607, doi:10.1002/jgra.50558.

Cohen, M. B., U. S. Inan, and M. Golkowski (2008), Geometric modulation: a more effective method of steerable ELF/VLF wave generation with continuous HF heating of the lower ionosphere, *Geophys. Res. Lett.*, *35*, L12101, doi:10.1029/2008GL03406.

Cohen, M. B., U. S. Inan, M. Golkowski, and M. J. McCarrick (2010), ELF/VLF wave generation via ionospheric HF heating: experimental comparison of amplitude modulation, beam painting, and geometric modulation, *J. Geophys. Res.*, *115*, A02302, doi:10.1029/2009JA014410.

Cohen, M. B., N. G. Lehtinen, U. S. Inan (2012a), Models of ionospheric VLF absorption of powerful ground based transmitters, *Geophys. Res. Lett.*, *39*, L24101, doi:10.1029/2012GL054437.

Cohen, M. B., R. C. Moore, M. Golkowski, and N. G. Lehtinen (2012b), ELF/VLF wave generation from the beating of two HF ionospheric heating sources, *J. Geophys. Res.*, *117*, A12310, doi:10.1029/2012JA018140.

Cummer, S. A. (1997), An analysis of new and existing FDTD methods for isotropic cold plasma and a method for improving their accuracy, *IEEE Trans. Antennas Propag.*, *45*, 392–400, doi:10.1109/8.558654.

Davies, D. K. (1983), Measurements of swarm parameter in dry air, in Theoretical Notes, *Note 346*, Westinghouse R&D Cent., Pittsburgh, PA.

Ferraro, A. J., H. S. Lee, R. Allshouse, K. Carroll, R. Lunnen, and T. Collins (1984), Characteristics of ionospheric ELF radiation generated by HF heating, *J. Atmos. Terr. Phys.*, *46*, 855–865, doi:10.1016/0021-9169(84)90025-4.

Franz, R. C., R. J. Nemzek, and J. R. Winckler (1990), Television image of a large upward electrical discharge above a thunderstorm system, *Science*, *249*, 48–51, doi:10.1126/science.249.4964.48.

Fujimaru, S. (2014), Optimization of beam painting for ELF/VLF wave generation at HAARP using time-of-arrival analysis, Ph.D. thesis, University of Florida, Gainesville, Florida.

Galejs, J. (1972), Ionospheric interaction of VLF radio waves, *J. Atmos. Terr. Phys.*, *34*(3), 421–436, doi:10.1016/0021-9169(72)90044-X.

Gamliel, E. (2017), Direct integration 3-D FDTD method for single-species cold magnetized plasma, *IEEE Trans. Antennas Propag.*, *65*, 295–308, doi:10.1109/TAP.2016.2617373.

Gandhi, O. P., B. Q. Gao, and J. Y. Chen (1993), A frequency-dependent finite-difference time-domain formulation for general dispersive media, *IEEE Trans. Microw. Theory Tech.*, *41*(4), 658–665, doi:10.1109/22.231661.

Getmantsev, C. G., N. A. Zuikov, D. S. Kotik, L. F. Mironenko, N. A. Mityakov, V. O. Rapoport, Y. A. Sazonov, V. Y. Trakhtengerts, and V. Y. Eidman (1974), Combination frequencies in the interaction between high-power short-wave radiation and ionospheric plasma, *JETP Lett.*, *20*, 101–102.

Ginzburg, V. L. (1964), *The propagation of electromagnetic waves in plasmas*, Pergamon, New York.

Golkowski, M., U. S. Inan, and M. B. Cohen (2009), Cross modulation of whistler mode and HF waves above the HAARP ionospheric heater, *Geophys. Res. Lett.*, *36*, L15103, doi:10.1029/2009GL039669.

Golkowski, M., U. S. Inan, M. B. Cohen, and A. R. Gibby (2010), Amplitude and phase of nonlinear magnetospheric wave growth excited by the HAARP HF heater, *J. Geophys. Res.*, *115*, A00F04, doi:10.1029/2009JA014610.

Golkowski, M., U. S. Inan, A. R. Gibby, and M. B. Cohen (2010), Magnetospheric amplification and emission triggering by ELF/VLF waves injected by the 3.6 MW HAARP ionospheric heater, *J. Geophys. Res.*, *113*, A10201, doi:10.1029/2008JA013157.

Gordillo-Vazquez, F. J., A. Luque, and C. Haldoupis (2016), Upper D region chemical kinetic modeling of LORE relaxation times, *J. Geophys. Res.*, *121*, 3525–3544, doi:10.1002/2015JA021408.

Graf, K. L., N. G. Lehtinen, M. Spasojevic, M. B. Cohen, R. A. Marshall, and U. S. Inan (2013), Analysis of experimentally validated trans-ionospheric attenuation estimates of VLF signals, *J. Geophys. Res. Space Phys.*, *118*, 2708–2720, doi:10.1002/jgra.50228.

Gurevich, A. V. (1978), *Nonlinear phenomena in the ionosphere*. Springer-Verlag, New York.

Haddad, M., V. Rakov, and S. Cummer (2012), New measurements of lightning electric fields in Florida: waveform characteristics, interaction with the ionosphere, and peak current estimates, *J. Geophys. Res.*, *117*, D10101, doi:10.1029/2011JD017196.

Han, F., and S. Cummer (2010a), Midlatitude nighttime D region ionosphere variability on hourly to monthly time scales, *J. Geophys. Res.*, *115*, A09323, doi:10.1029/2010JA015437.

Han, F., and S. Cummer (2010b), Midlatitude daytime D region ionosphere variations measured from radio atmospherics, *J. Geophys. Res.*, *115*, A10314, doi:10.1029/2010JA015715.

Han, F., S. Cummer, J. Li, and G. Lu (2011), Daytime ionospheric sharpness derived from VLF radio atmospherics, *J. Geophys. Res.*, *116*, A05314, doi:10.1029/2010JA016299.

Hargreaves, J. K. (1979), *The upper atmosphere and solar-terrestrial relations*. Van Nostrand Reinhold, New York.

Hegerberg, R., and I. D. Reid (1980), Electron drift velocities in air, *Aust. J. Phys.*, *23*(1), doi:10.1071/PH800227a.

Heidler, F., J. M. Cvetic, and B. V. Stanic (1999), Calculation of lightning current parameters, *IEEE Trans. Power Delivery*, *14*(2), 399–404, doi:10.1109/61.754080.

Hu, W., and S. A. Cummer (2006), An FDTD model for low and high altitude lightning-generated EM fields, *IEEE Trans. Antennas Propag.*, *54*, 1513–1522, doi:10.1109/TAP.2006.874336.

Hunsberger, F., R. Luebbers, and K. Kunz (1992), Finite-difference time-domain analysis of gyrotropic media-I: magnetized plasma, *IEEE Trans. Antennas Propag.*, *40*(12), 1489–1495, doi:10.1109/8.204739.

Huxley, L. G. H., and J. A. Ratcliffe (1949), A survey of ionospheric cross-modulation, *Proc. Inst. Elec. Eng.*, *96*, 433–440.

Inan, U. S., S. A. Cummer, and R. A. Marshall (2010), A survey of ELF and VLF research on lightning-ionosphere interactions and causative discharges, *J. Geophys. Res.*, *115*, A00E36, doi:10.1029/2009JA014775.

Inan, U. S., and A. S. Inan (1999), *Engineering Electromagnetics*, Addison Wesley, Menlo Park, CA.

Inan, U. S., M. Golkowski, D. L. Carpenter, N. Reddell, R. C. Moore, T. F. Bell, E. Paschal, P. Kossey, E. Kennedy, and S. Z. Meth (2004), Multi-hop whistler-mode ELF/VLF signals and triggered emissions excited by the HAARP HF heater, *Geophys. Res. Lett.*, *31*, L24805, doi:10.1029/2004GL021647.

Inan, U. S., J. V. Rodriguez, S. Lev-Tov, and J. Oh (1992), Ionospheric modification with a VLF transmitter, *Geophys. Res. Lett.*, *19*, 2071–2074, doi:10.1029/92GL02378.

Jacobson, A., X-M. Shao, and R. Holzworth (2009a), Full-wave reflection of lightning long-wave radio pulses from the ionospheric D region: numerical model, *J. Geophys. Res.*, *114*, A03303, doi:10.1029/2008JA013642.

Jacobson, A., X-M. Shao, and R. Holzworth (2009b), Full-wave reflection of lightning long-wave radio pulses from the ionospheric D region: comparison with midday observations of broadband lightning signals, *J. Geophys. Res.*, *115*, A00E27, doi:10.1029/2009JA014540.

James, H. G., R. L. Dowden, M. T. Rietveld, P. Stubbe, and H. Kopka (1984), Simultaneous observations of ELF waves from an artificially modulated auroral electrojet in space and on the ground, *J. Geophys. Res.*, *89*, 1655–1666, doi:10.1029/JA089iA03p01655.

Joseph, R. M., S. C. Hagness, and A. Taflove (1991), Direct time integration of Maxwell's equations in linear dispersive media with absorption for scattering and propagation of femtosecond electromagnetic pulses, *Optics Lett.*, *16*(18), 1412–1414, doi:10.1364/OL.16.001412.

Kelley, D. F., and R. J. Luebbers (1996), Piecewise linear recursive convolution for dispersive media using FDTD, *IEEE Trans. Antennas Propag.*, *44*, 792–797, doi:10.1109/8.509882.

Kinzer, G. D. (1974) Cloud-to-ground lightning versus radar reflectivity in Oklahoma thunderstroms, *J. Atmos. Sci.*, *31*, 787–799.

Koh, K. L., A. J. Bennett, S. Ghilain, Z. Liu, S. Pedeboy, A. Peverell, and M. Fullekrug (2019), Lower ionospheric conductivity modification above a thunderstorm updraught, *J. Geophys. Res. Space Physics*, *124*, doi:10.1029/2019JA026863.

Kotik, D. S., and E. N. Ermakova (1998), Resonances in the generation of electromagnetic signals due to the thermal cubic nonlinearity in the lower ionosphere, *J. Atmos. Solar Terr. Phys.*, *60*, 1257–1259, doi:10.1016/S1364-6826(98)00053-4.

Kotovsky, D. A. (2016), Response of the nighttime upper mesosphere to electric field changes produced by lightning discharges, (Doctoral dissertation). Gainesville, FL: University of Florida.

Kotovsky, D. A., and R. C. Moore (2016a), Photochemical response of the nighttime mesosphere to electric field heating – onset time of electron density enhancements, *J. Geophys. Res. Space Physics*, *121*, 4782–4799, doi:10.1002/2015JA022054.

Kotovsky, D. A., and R. C. Moore (2016b), Photochemical response of the nighttime mesosphere to electric field heating – recovery of electron density enhancements, *Geophys. Res. Lett.*, *43*, 952–960, doi:10.1002/2015GL067014.

Kotovsky, D. A., and R. C. Moore (2017), Modeling long recovery events (LOREs) produced by lightning-induced ionization of the nighttime upper mesosphere, *J. Geophys. Res. Space. Phys.*, *122*, 7761–7780, doi:10.1002/2017JA023996.

Kuo, C-L. et al. (2007), Modeling elves observed by FORMOSAT-2 satellite, *J. Geophys. Res.*, *112*, A11312, doi:10.1029/2007JA012407.

Kuo, C-L. et al. (2007), Full-kinetic elve model simulations and their comparisons with the ISUAL observed events, *J. Geophys. Res.*, *117*, A07320, doi:10.1029/2012JA017599.

Langston, J., and R. C. Moore (2013), High time resolution observations of HF cross-modulation with the D region ionosphere, *Geophys. Res. Lett.*, *40*, 1912–1916,doi:10.1002/grl.50391.

Lay, E. H., X.-M. Shao, and A. R. Jacobson (2014), *D* region electron profiles observed with substantial spatial and temporal change near thunderstorms, *J. Geophys. Res. Space Physics*, *119*, 4916–4928, doi:10.1002/2013JA019430.

Lehtinen, N. G., and U. S. Inan (2008), Radiation of ELF/VLF waves by harmonically varying currents into a stratified ionosphere with application to radiation by a modulated electrojet, *J. Geophys. Res.*, *113*, A06301, doi:10.1029/2007JA012569.

Lehtinen, N. G., and U. S. Inan (2009), Full-wave modeling of transionospheric propagation of VLF waves, *Geophys. Res. Lett.*, *36*, L03104, doi:10.1029/2008GL036535.

Liu, N. (2012), Multiple ion species fluid modeling of sprite halos and the role of electron detachment of O- in their dynamics, *J. Geophys. Res.*, *117*, A03308, doi:10.1029/2011JA017062.

Luebbers, R., F. Hunsberger, K. S. Kunz, R. Standler, and M. Schneider (1990), A frequency-dependent finite-difference time-domain formulation for dispersive media, *IEEE Trans. Electromagn. Compat.*, *32*, 222–227, doi:10.1109/15.57116.

Luebbers, R., F. Hunsberger, and K. Kunz (1991), A frequency-dependent finite-difference time-domain formulation for transient propagation in plasma, *IEEE Trans. Antennas Propag.*, *39*(1), 29–34, doi:10.1109/8.64431.

Luque, A. et al. (2014), Coupling between atmospheric layers in gaseous giant planets due to lightning-generated electromagnetic pulses, *J. Geophys. Res.*, *119*, 8705–8720, doi:10.1002/2014JA020457.

Malins, J. B., K. S. Obenberger, G. B. Taylor, and J. Dowell (2019), Three dimensional mapping of lightning produced ionospheric reflecions, *Radio Sci.*, doi:10.1029/2019RS006857.

Marshall, R. (2012), An improved model of the lightning electromagnetic field interaction with the D-region ionosphere, *J. Geophys. Res.*, *117*, A03316, doi:10.1029/2011JA017408.

Marshall, R. (2014), Effect of self-absorption on attenuation of lightning and transmitter signals in the lower ionosphere, *J. Geophys. Res.*, *119*, A019921, doi:10.1002/2014JA019921.

Marshall, R., U. Inan, and V. Glukhov (2010), Elves and associated electron density changes due to cloud-to-ground and in-cloud lightning discharges, *J. Geophys. Res.*, *115*, A00E17, doi:10.1029/2009JA014469.

McCormick, J. C., M. B. Cohen, N. C. Gross, and R. K. Said (2018), Spatial and temporal ionospheric monitoring using broadband sferic measurements, *J. Geophys. Res. Space Physics*, *123*, 3111–3130, doi:10.1002/2017JA024291.

McDonald, T. B. III, M. A. Uman, J. A. Tiller, and W. H. Beasley (1979), Lightning location and lower-ionospheric height determination from two-station magnetic field measurements, *J. Geophys. Res.*, *84*, 8C0739, doi:10.1029/JC084iC04p01727.

Milikh, G. M., K. Papadopoulos, M. McCarrick, and J. Preston (1999), ELF emission generated by the HAARP HF-heater using varying frequency and polarization, *Izvestiya Vysshikh Uchebnykh Zavedenii, Radiofizika*, *42*, 728–735.

Moore, R. C. (2007), ELF/VLF wave generation by modulated HF heating of the auroral electrojet, (Doctoral dissertation). Stanford, CA: Stanford University.

Moore, R. C., and D. Agrawal (2011), ELF/VLF wave generation using simultaneous CW and modulated HF heating of the ionosphere, *J. Geophys. Res.*, *116*, A04217, doi:10.1029/2010JA015902.

Moore, R. C., S. Fujimaru, D. A. Kotovsky, and M. Golkowski (2013), Observations of ionospheric ELF and VLF wave generation by excitation of the thermal cubic nonlinearity, *Phys. Rev. Lett.*, *111*, 235007, doi:10.1103/PhysRevLett.111.235007.

Moore, R. C., U. S. Inan, and T. F. Bell (2006), Observations of amplitude saturation in ELF/VLF wave generation by modulated HF heating of the auroral electrojet, *Geophys. Res. Lett.*, *33*, L12106, doi:10.1029/2006GL025934.

Moore, R. C., U. S. Inan, T. F. Bell, and E. J. Kennedy (2007), ELF waves generated by modulated HF heating of the auroral electrojet and observed at a ground distance of 4400 km, *J. Geophys. Res.*, *112*, A05309, doi:10.1029/2006JA012063.

Moore, R. C., S. Fujimaru, M. Cohen, M. Golkowski, and M. J. McCarrick (2012), On the altitude of the ELF/VLF source region generated during "beat-wave" HF heating experiments, *Geophys. Res. Lett.*, *39*, L18101, doi:10.1029/2012GL053210.

Mostajabi, A., D. Li, M. Azadifar, F. Rachidi, M. Rubinstein, G. Diendorfer, W. Schulz, H. Pichler, V. A. Rakov, and D. Pavanello (2019), Analysis of a bipolar upward lightning flash based on simultaneous records of currents and 380-km distant electric fields, *Elec. Power Sys. Res.*, *174*, 105845, doi:10.1016/j.epsr.2019.04.023.

Newsome, R. T., and U. S. Inan (2010), Free-running ground-based photometric array imaging of transient luminous events, *J. Geophys. Res.*, *115*, A00E41, doi:10.1029/2009JA014834.

Nickisch, L. J., and P. M. Franke (1992), Finite-difference time-domain solution of Maxwell's equations for the dispersive ionosphere, *IEEE Antennas Propagat. Mag.*, *34*, 33–39, doi:10.1109/74.163808.

Obenberger, K. S., J. D. Dowell, J. Malins, R. T. Parris, T. R. Pedersen, and G. B. Taylor (2018), Using lightning as a HF signal source to produce ionograms, *Radio Sci.*, *53*, 1419–1425, doi:10.1029/2018RS006680.

Papadopoulos, K., C.-L. Chang, J. Labenski, and T. Wallace (2011a), HF-driven currents in the polar ionosphere, *Geophys. Res. Lett.*, *38*, L12103, doi:10.1029/2011GL047368.

Papadopoulos, K., N. A. Gumerov, X. Shao, I. Doxas, and C. L. Chang (2011b), First demonstration of HF-driven ionospheric currents, *Geophys. Res. Lett.*, *38*, L20107, doi:10.1029/2011GL049263.

Pasko, V. P. (1998), Dynamic coupling of quasi-electrostatic thundercloud fields to the mesosphere and lower ionosphere: sprites and jets, (Doctoral dissertation). Stanford, CA: Stanford University.

Pasko, V. P., U. S. Inan, T. F. Bell, and Y. Taranenko (1997), Sprites produced by quasi-electrostatic heating and ionization in the lower ionosphere, *J. Geophys. Res.*, *102*, 4529–4561, doi:10.1029/96JA03528.

Pasko, V. P., M. A. Stanley, J. D. Mathews, U. S. Inan, and T. G. Wood (2002), Electrical discharge from a thundercloud top to the lower ionosphere, *Nature*, *416*, 152–154.

Pereda, J. A., A. Vegas, and A. Prieto (2002), FDTD modeling of wave propagation in dispersive media by using the mobius transformation technique, *IEEE Trans. Microw Theory Tech.*, *50*, 1689–1695, doi:10.1109/TMTT.2002.800388.

Pereda, J. A., L. A. Vielva, A. Vegas, and A. Prieto (2001), Analyzing the stability of the FDTD technique by combining the von Neumann method with the Routh-Hurwitz criterion, *IEEE Trans. Microw Theory Tech.*, *49*, 377–381, doi:10.1109/22.903100.

Qin, Z., S. A. Cummer, M. Chen, F. Lyu, and Y.-p. Du (2019), A comparative study of the ray theory model with the finite difference time domain model for lightning sferic transmission in Earth-ionosphere waveguide, *J. Geophys. Res. Atmos.*, *124*, 3335–3349, doi:10.1029/2018JD029440.

Rakov, V. A., and M. A. Uman (2003), *Lightning: Physics and Effects*, Cambridge Univ. Press, New York.

Ratcliffe, J. A. (1959), *The magneto-ionic theory and its application to the ionosphere*, Cambridge Univ. Press, Cambridge.

Rietveld, M. T., P. Stubbe, and H. Kopka (1989), On the frequency dependance of ELF/VLF waves produced by modulated ionospheric heating, *Radio Sci.*, *24*, 270–278, doi:10.1029/RS024i003p00270.

Rishbeth, H., and O. K. Garriott (1969), *Introduction to ionospheric physics*. Academic Press, New York,.

Rodriguez, J. V. (1994), Modification of the Earth's ionosphere by very-low-frequency transmitters, (Doctoral dissertation). Stanford, CA: Stanford University.

Rodriguez, J. V., and U. S. Inan (1994), Electron density changes in the nighttime D region due to heating by very-low-frequency transmitters, *Geophys. Res. Lett.*, *21*, 93–96, doi:10.1029/93GL0300.

Salem, M. A., N. Liu, and H. K. Rassoul (2015), Effects of small thundercloud electrostatic fields on the ionospheric density profile, *Geophys. Res. Lett.*, *42*, 1619–1625, doi:10.1002/2015GL063268.

Salem, M. A., N. Liu, and H. K. Rassoul (2016), Modification of the lower ionospheric conductivity by thunderstorm electrostatic fields, *Geophys. Res. Lett.*, *42*, 5–12, doi:10.1002/2015GL066933.

Schonland, B. F. J., J. S. Elder, D. G. Hodges, W. E. Phillips, and J. W. van Wyk (1940) The wave form of atmospherics at night, *Proc. Roy. Soc., Ser. A*, *176*, 180–202, doi:10.1098/rspa.1940.0085.

Sen, H. K., and A. A. Wyller (1960), On the generalization of the Appleton-Hartree magnetoionic formulas, *J. Geophys. Res.*, *65*, 3931– 3950, doi:10.1029/JZ065i012p03931.

Senior, A., M. T. Rietveld, M. J. Kosch, and W. Signer (2010), Diagnosing radio plasma heating in the polar summer mesosphere using cross modulation: Theory and observations, *J. Geophys. Res.*, *115*, A09318, doi:10.1029/2010JA015379.

Sentman, D. D., E. M. Wescott, D. L. Osborne, D. L. Hampton, and M. J. Heavner (1995), Preliminary results from the Sprites94 aircraft campaign: 1. red sprites, *Geophys. Res. Lett.*, *22*, 1205–1208, doi:10.1029/95GL00583.

Shao, X-M., E. Lay, and A. Jacobson (2012), Reduction of electron density in the night-time lower ionosphere in response to a thunderstorm, *Nat. Geosci.*, *6*, NGEO1668.

Somu, V., V. Rakov, M. Haddad, and S. Cummer (2015), A study of changes in apparent ionospheric reflection height with individual flashes, *J. Atmos. Terr. Phys.*, *136*, 66–79, doi:10.1016/j.jastp.2015.09.007.

Stubbe, P., and H. Kopka (1977), Modulation of the polar electrojet by powerful HF waves, *J. Geophys. Res.*, *82*, 2319–2325, doi:10.1029/JA082i016p02319.

Stubbe, P., H. Kopka, M. T. Rietveld, and R. L. Dowden (1982), ELF and VLF generation by modulated HF heating of the current carrying lower ionosphere, *J. Atmos. Terr. Phys.*, *44*, 1123–1135, doi:10.1016/0021-9169(82)90023-X.

Su, H. T., R. R. Hsu, A. B. Chen, Y. C. Wang, W. S. Hsiao, W. C. Lai, L. C. Lee, M. Sato, and H. Fukunishi (2003), Gigantic jets between a thundercloud amd the ionosphere, *Nature*, *423*, 974–976.

Taflove, A., and S. C. Hagness (2005), *Computational electromagnetics: finite-difference time-domain method*, Artech House, Norwood, MA.

Taranenko, Y., U. S. Inan, and T. F. Bell (1993a), Interaction with the lower ionosphere of electromagnetic pulses from lightning: excitation of optical emissions, *Geophys. Res. Lett.*, *20*, 2675–2678, doi:10.1029/93GL02838.

Taranenko, Y., U. S. Inan, and T. F. Bell (1993b), Interaction with the lower ionosphere of electromagnetic pulses from lightning: heating, attachment, and ionization, *Geophys. Res. Lett.*, *20*, 1539–1542, doi:10.1029/93GL01696.

Tellegen, B. D. H. (1933), Interaction between radio waves, *Nature*, *131*, 840, doi:10.1038/131840a0.

Tomko, A. A., A. J. Ferraro, and H. S. Lee (1980), D region absorption effects during high-power radio wave heating, *Radio Sci.*, *15*, 675–682, doi:10.1029/RS015i003p00675.

Tran, T., Y. Baba, V. Somu, and V. Rakov (2017), FDTD modeling of LEMP propagation in the earth-ionosphere waveguide with emphasis on realistic representation of lightning source, *J. Geophys. Res.*, *122*, D027305, doi:10.1002/2017JD027305.

Uman, M. A. (1964), *Introduction to plasma physics*. McGraw-Hill, New York.

Uman, M. A., and D. K. McLain (1969), Magnetic field of lightning return stroke, *J. Geophys. Res.*, *74*, 6899–6910, doi:10.1029/JC074i028p06899.

Uman, M. A., and D. K. McLain (1970), Lightning return stroke current from magnetic and radiation field measurements, *J. Geophys. Res.*, *75*, 5143–5147, doi:10.1029/JC075i027p05143.

Uman, M. A., D. K. McLain, and E. P. Krider (1975), The electromagnetic radiation from a finite antenna, *American Journal of Physics*, *43*, doi:10.1119/1.10027.

Veronis, G., V. P. Pasko, and U. S. Inan (1999), Characteristics of mesospheric optical emissions produced by lightning discharges, *J. Geophys. Res.*, *104*, 12,645–12,656, doi:10.1029/1999JA900129.

Wait, J. R. (1969), Reflection of a plane transient electromagnetic wave from a cold lossless plasma slab, *Radio Sci.*, *4*, 401–405, doi:10.1029/RS004i004p00401.

Wescott, E. M., D. D. Sentman, M. J. Heavner, D. L. Hampton, D. L. Osborne, and H. Vaughan Jr. (1996), Blue starters: brief upward discharges from an intense Arkansas thunderstorm, *Geophys. Res. Lett.*, *23*, 2153–2156, doi:10.1029/96GL01969.

Wescott, E. M., D. Sentman, D. Osborne, D. Hampton, and M. Heavner (1995), Preliminary results from the Sprites94 aircraft campaign: 2. blue jets, *Geophys. Res. Lett.*, *2*, 1209–1212, doi:10.1029/95GL00582.

Wescott, E. M., H. C. Stenbaek-Nielsen, D. D. Sentman, M. J. Heavner, D. R. Moudry, and F. T. Sao Sabbas (2001), Triangulation of sprites, associated halos and their possible relation to causative lightning and micrometeors, *J. Geophys. Res.*, *106*, 10467–10477, doi:10.1029/2000JA000182.

Westcott, B. S. (1962a), Ionospheric reflection processes for long radio wave – I, *J. Atmos. Terr. Phys.*, *24*, 385–399, doi:10.1016/0021-9169(62)90233-7.

Westcott, B. S. (1962b), Ionospheric reflection processes for long radio wave – II, *J. Atmos. Terr. Phys.*, *24*, 619–631, doi:10.1016/0021-9169(62)90084-3.

Wilson, C. T. R. (1924), The electric field of a thundercloud and some of its effects, *Proc. Phys. Soc. London*, *37*, 32D–37D, doi:10.1088/1478-7814/37/1/314.

Yee, K. (1966), A numerical solution of initial boundary value problems involving Maxwell's equations in isotropic media, *IEEE Trans. Antennas Propag.*, *14*, 302–307, doi:10.1109/TAP.1966.1138693.

Young, J. L. (1994), A full finite difference time domain implementation for radio wave propagation in a plasma, *Radio Sci.*, *29*, 1513–1522, doi:10.1029/94RS01921.

Young, J. L., and R. O. Nelson (2001), A Summary and Systematic Analysis of FDTD Algorithms for Linearly Dispersive Media, *IEEE Antennas Propag. Mag.*, *43*, 61–77, doi:10.1109/74.920019.

Yu, Y., and J. J. Simpson (2010), An E-J collocated 3-D FDTD model of electromagnetic wave propagation in magnetized cold plasma, *IEEE Trans. Antennas Propag.*, *58*(2), 469–478, doi:10.1109/TAP.2009.2037706.

BIOGRAPHICAL SKETCH

Anthony Joseph 'AJ' Erdman was born in Central Florida in 1993. He attended DeLand High School where he graduated salutatorian of the class of 2010. In May 2014, AJ graduated Cum Laude from the University of Notre Dame du Lac, receiving a Bachelor of Science in physics with a concentration in advanced physics. In June 2015, AJ enrolled in the Ph.D. program at the University of Florida, Department of Electrical and Computer Engineering, in Gainesville, FL. AJ completed his Ph.D. at the University of Florida under advisor Dr. Robert Moore in December 2019.